A NEW THERMAL HYDRAULICS CODE COUPLED TO AGENT FOR LIGHT WATER REACTOR ANALYSIS

by

Matthew Deric Eklund

A thesis submitted to the faculty of
The University of Utah
in partial fulfillment of the requirements for the degree of

Master of Science

in

Nuclear Engineering

Department of Civil and Environmental Engineering

The University of Utah

May 2016

The University of Utah Graduate School

STATEMENT OF THESIS APPROVAL

The following faculty members served as the supervisory committee chair and members for the thesis of Matthew Deric Eklund.

Dates at right indicate the members' approval of the thesis.

Tatjana Jevremovic, Chair	09/08/2015 Date Approved
Luther McDonald, Member	09/08/2015 Date Approved
Shadrach Roundy, Member	09/08/2015 Date Approved

The thesis has also been approved by Michael E. Barber Chair/Dean of the Department/School/College of Civil and Environmental Engineering and by David B. Kieda, Dean of The Graduate School.

ABSTRACT

A new numerical model for coupling a thermal hydraulics method based on the Drift Flux and Homogeneous Equilibrium Mixture (HEM) models, with a deterministic neutronics code system AGENT (Arbitrary Geometry Neutron Transport), is developed. Named the TH thermal hydraulics code, it is based on the mass continuity, momentum, and energy equations integrated with appropriate relations for liquid and vapor phasic velocities. The modified conservation equations are then evaluated in one-dimensional (1D) steady-state conditions for light water reactor (LWR) coolant subchannel in the axial direction. This permits faster computation times without sacrificing significant accuracy, as compared to other three-dimensional (3D) codes such as RELAP5/TRACE.

AGENT is a deterministic neutronics code system based on the Method of Characteristics to solve the 2D/3D neutron transport equation in current and future reactor systems. The coupling scheme between the TH and AGENT codes is accomplished by computing the normalized fission rate profile in the LWR fuel elements by AGENT. The normalized fission rate profile is then transferred to the TH thermal hydraulics code for computing the reactor coolant properties. In conjunction with the 1D axial TH code, a separate 1D radial heat transfer model within the TH code is used to determine the average fuel temperature at each node where coolant properties are calculated. These properties then are entered into Scale 6.1, a criticality analysis code, to recalculate fuel pin neutron interaction cross sections based on thermal feedback. With

updated fuel neutron interaction cross sections, the fission rate profile is recalculated in AGENT, and the cycle continues until convergence is reached.

The TH code and coupled AGENT-TH code are benchmarked against the TRACE reactor analysis software, showing required agreement in evaluating the basic reactor parameters.

This work is dedicated to my mother, Julie.

TABLE OF CONTENTS

LIST OF TABLES

LIST OF FIGURES

ACKNOWLEDGEMENTS

I express my gratitude to my many teachers and advisors over the years for having continually excelled as educators and for having inspired me to continue in my academic career. I thank Dr. Tatjana Jevremovic for her guidance and support as my graduate advisor and during my time as an undergraduate student at The University of Utah, for introducing me into the world of Nuclear Engineering, and for her passion of teaching. I also thank Dr. Kirk Hagen for sharing his invaluable experience as an engineer in the industry and for his excellence in teaching the fundamentals of Mechanical Engineering during my undergraduate years at Weber State University. I would also like to thank Dr. Dong-Ok Che, Dr. Hermilo Hernandez, and Dr. Miltos Alamaniotis for their tireless support. Many hours of class preparation, answering questions, grading, collaboration, code debugging, and shared jovial conversations have greatly enriched and expounded my academic experience in The University of Utah Nuclear Engineering Program (UNEP). I also thank the Nuclear Regulatory Commission (NRC) for providing the funding for the duration of my graduate studies as a NRC Fellow at The University of Utah.

I express gratitude to all my acquaintances from my undergraduate years; in particular, I thank my fellow Mechanical Engineering Senior Design group members Juan Sandoval, Bryant Parker, Josh Erramouspe, and Cameron Cross, for all the late-night study sessions and working to successfully meet our project deadlines.

Thanks also go to fellow UNEP students for their aid in coursework and research efforts: Sarah Obadina, Fawaz Alroumi, Zoairia Lyric, Varun Vijay, Victor Bautista, Evelynn van den Akker, Samantha Winkle, Matthew Lund, Josh Chidester, Orland Bateman, Christian Adjei, Sangkyu Lee, and Ryan Schow. Particular thanks go to R.W. Sisson, without whom I could not have completed this thesis.

I thank my family and friends for their support and understanding. Long before my interest in Nuclear Engineering grew, they supported me during rough times and encouraged me to realize my full potential. I extend all my thanks and love to my parents, grandparents, and siblings for making me the person I am today. I thank Stephen Morphet for always being a friend since early childhood and a great example of an American soldier and scholar. I also thank Dr. Brandon Burnett, for being my hero of our hometown of North Ogden.

Finally, I thank God and His Son, Jesus Christ, for granting me the mental faculties and ambition to achieve my goals and for giving me each new day another chance to improve and overcome my faults and weaknesses. I hope to follow the examples of fellow Latter-Day Saints before me such as Dr. Henry Eyring, Richard G. Scott, and Dr. Joseph F. Merrill, who have demonstrated a firm belief in God as well as a commitment to the growth of knowledge in science and engineering.

CHAPTER 1

INTRODUCTION

1.1 Motivation

Light water reactors (LWRs), including boiling water reactors (BWRs) and pressurized water reactors (PWRs), operate using light water as both a coolant and as a neutron moderator (which reduces fast neutrons at energies exceeding 1 MeV born from nuclear fission to energies conducive to reproducing further nuclear fission reactions). The operation of LWRs heavily depends on the coolant/moderator operating with a defined set of parameters. Extending beyond these parameters leads to dangerous situations such as LOCAs (Loss of Coolant Accidents) and CHF (Critical Heat Flux), where the heat transfer between the coolant and reactor behaves in a drastically different manner than intended (Todreas & Kazimi, 1990). It is for this reason that the analysis of coolant properties is critical for the design and safe operation of nuclear reactors. The coolant properties, such as temperature, pressure, density, etc., all have an effect on the operation of the reactor, ultimately affecting the neutron interactions with the reactor fuel, which affects the overall reactor power level.

The AGENT (Arbitrary Geometry Neutron Transport) code is an effective and accurate methodology applicable for the analysis of nuclear systems (Jevremovic et al., 2006). The AGENT code, based on the ANEMONA code developed by Jevremovic et

al. (2001; Jevremovic et al., 2002), uses the Method of Characteristics to solve the neutron transport equation (Xiao, 2009). While highly effective at modeling neutron interactions and flux within a reactor, AGENT does not include analysis of reactor coolant properties and behavior which can alter the performance of the system.

Previous to the work presented in this thesis, the AGENT had not yet had a coolant hydrodynamic or heat transfer model included, focusing primarily on nuclear reactor physics (specifically neutronics). To more accurately model LWRs, a new thermal-hydraulic code is necessary which takes account of temperature feedback on the reactor fuel affecting its nuclear macroscopic cross sections, or material properties which dictate the likelihood and type of interaction between neutrons of a specific energy and the bulk material (Duderstadt & Hamilton, 1976; Jevremovic, 2009). The TH (Thermal Hydraulics) code is coupled with the AGENT neutronics code to take the effect of the coolant into account in the operation of a LWR. This will increase the accuracy of the reactor power profile and operating conditions and enable design of LWR reactors more feasible than with neutronics capabilities alone.

1.2 Thesis Objectives

The objectives for this MS thesis are as follows:

1. To implement a simplified model based on the drift flux model and homogeneous equilibrium mixture (HEM) model into the AGENT code system, and therefore develop the AGENT-TH code coupled system.
2. To perform and analyze benchmarks of the drift flux model and HEM model using a BWR pin and PWR pin, respectively, against results from TRACE reactor

analysis software.

3. To extend the drift flux and HEM solvers to multichannel implementation and coupling the new TH code with the AGENT code.
4. To perform and analyze benchmark of a BWR pin using the coupled AGENT-TH code and compare against results from TRACE reactor analysis software.
5. To discuss capabilities of the coupled AGENT-TH code in analyzing PWR and BWR pins, compare accuracy of AGENT-TH analyses versus results from TRACE, and describe recommended future work to improve accuracy from benchmark results.

1.3 Organization of the Thesis

Chapter 1 is an introduction to the entire format and content of the thesis. Following this introductory chapter, Chapter 2 provides a general overview of the AGENT neutronics code, its basis, the Method of Characteristics, a brief introduction to R-functions, etc. Chapter 3 discusses the mass continuity, momentum, and energy equations integrated with the Drift Flux and Homogeneous Equilibrium Mixture (HEM) models as applied to heated BWR and PWR channels, respectively, in the TH code.

Included in Chapter 3 is a treatment on the Net Vapor Generation Model, the Fuel Pin Temperature Model, Void Fraction correlations, etc. used in the code to solve the conservation equations. It also describes the finite difference scheme employed in the coupled TH code. The 1D radial heat transfer used to determine the average nodal fuel temperatures for use in coupling the AGENT-TH code is also described in detail in Chapter 3.

Chapter 4 includes several benchmarks of the TH code's thermal-hydraulic capability against single BWR and PWR fuel pins using the TH code's drift flux and HEM models, respectively. Following these examples, a benchmark of a coupled AGENT-TH analysis is performed on a single BWR pin to demonstrate the temperature-dependent neutron cross sections on the averaged axial power profile of the pin. In all the preceding benchmarks, the TRACE reactor analysis software is used as a basis of comparison for the effectiveness of the TH thermal-hydraulic code and the coupled AGENT-TH code.

Following the benchmarks in Chapter 4, Chapters 5 and 6 include the main conclusions and recommended future work, respectively, for this thesis.

The attached appendices include the various TH code components used to run the code. Appendix A includes the main Matlab file and the appendices that follow include the associated Matlab files that are called by the main file.

The final section of the thesis includes the list of references used throughout this work.

CHAPTER 2

AGENT NEUTRONICS CODE SYSTEM

2.1 Method of Characteristics (MOC)

The AGENT neutronics code, which has been coupled with the new TH thermal hydraulics code to create the AGENT-TH code, is described in detail in this chapter. The theoretical basis of the AGENT methodology is introduced whereby the neutron transport equation is evaluated in 2D and 3D. This methodology is then described in detail as it is applied for the modeling and analysis of the neutronics of LWR core assemblies. The subsequent Chapter 3 will describe the TH thermal hydraulics code and the scheme by which it is coupled to the AGENT neutronics code for LWR analysis.

As an introduction, the AGENT code is fundamentally based on the method of characteristics (Eklund et al., 2015; Hursin and Jevremovic, 2005; Hursin et al., 2006). Simply, the method of characteristics is used to solve partial differential equations (PDEs) (Abbot, 1966; Haberman, 1983). This is done by reducing the PDE to an ordinary differential equation (ODE), where various simple techniques exist to solve such an equation (Asmar, 2005). Such techniques include separation of variables, direct integration, the introduction of an exponential factor, etc., depending on the type of ODE considered.

The MOC is based on the solution of a PDE along characteristic curves or rays of

constant value (Hong and Cho, 1998). The MOC is a flexible method but also necessitates long calculation times due to its solution of PDEs through successive iterations (Lathrop, 1969). Acceleration and optimization techniques exist and are developed to mitigate this deleterious effect, ultimately speeding up the convergence process. Also, including a large set of characteristic curves will increase accuracy but will also increase calculation time; thus, the optimization of the number of curves to be calculated will reduce unnecessary computation which provides negligible additional accuracy. With the evolution of computers, including large memory storage, parallel processing, GPU acceleration, etc., MOC solutions become more feasible, accurate and efficient (Tai et al., 2005). The MOC has become a viable and effective means to solve PDEs for different science and engineering problems (Boroushaki, 2009).

2.2 AGENT Methodology

The AGENT code (Hursin and Jevremovic, 2005; Hursin et al., 2006) is a 2D/3D MOC neutron transport code based on the ANEMONA code which was originally developed by Jevremovic et al. (2001; Jevremovic et al., 2002). It is capable of performing two- or three-dimensional heterogeneous nuclear reactor modeling (Jevremovic et al., 2006). AGENT is an accurate, computationally-resourceful code able to model and analyze reactor cores with hexagonal and rectangular lattice configurations, as well as any arbitrary geometry (Jevremovic et al, 2001). Its efficiency results from the combination of *R*-functions (used to model any desired geometry) with MOC. A web-based version of AGENT has been also developed as part of the *virtual reactor* (Jevremovic et al., 2006).

The AGENT neutronics code increases efficiency and decreases computation time by subdividing reactor cores into three levels of complexity, allowing for a solution in 2D or 3D coordinates. The first level of complexity is the unit cell, which is the smallest region in a nuclear reactor core which includes a single pin (which may be composed of fuel, neutron absorber/poison, water, etc.), cladding, and any other features inherent to that cell. After the unit cell, the second level of complexity is a reactor assembly, which is simply a composition of several unit cells typically in a rectangular or hexagonal lattice. The third level of complexity is the full core, consisting of multiple reactor assemblies. As layers of complexity are added to the reactor core simulation, longer computation time and additional computational resources are necessary when using the same techniques.

The 'solution-rays,' or vectors which each represent neutron trajectories, are located along several polar and angular directions which pass through the unit cell or reactor assembly. The locations at which the ray vectors intersect the cell or assembly boundary account for a neutron flux entering or exiting the cell (the latter being neutron leakage). Whether the neutron flux is considered as entering or leaking from the system depends on the direction of the ray vectors. A set of rays parallel to each other is applied to the system with the distance between the parallel rays being the ray separation (measured in centimeters). In order to increase accuracy, a smaller ray separation may be used, however, this will add to the computation time. A smaller ray separation results in a larger number of rays being surveyed within the reactor cell or assembly.

After several rays pass through a system, a weighted flux value for each zone, separated by material and system submeshing, is calculated. The neutron flux values located at the intersection between each set of rays and a boundary edge are used to

calculate a weighted flux at the boundary edge. The flux within a zone is then calculated by taking the weighted mean neutron flux on each ray which intersects through the zone. These weighted zone flux values are scalar, whereas the flux values determined on the cell boundary are angular flux values, having both a magnitude and direction. These are used in Multi-AGENT for determining the number and direction of neutrons interacting between each sub-assembly.

The material type determines the system's macroscopic cross sections as calculated using the Scale library. These must be calculated for each material zone and entered in the AGENT input file before the code may be run. Figure 2.1 displays a single square unit cell consisting of fuel, cladding, and moderator materials (labeled as zones 1, 2, and 3, respectively) with rays separated by a distance δA at an azimuthal angle α. The dark dots indicate intersection between each ray and a zone boundary. The cell boundary is divided into a set of edges (indicated by lines extending beyond the unit cell) where the mean of the incoming and outgoing neutron flux values are calculated amongst the rays that extend in the cell. A smaller zone size will increase the accuracy of the calculation. The zone size may be reduced by using a finer zone subdivision, more rays (by reducing ray separation distance), including more angles (along azimuthal angles in the $x-y$ plane and polar angles extended from the z axis), and a finer energy resolution (i.e. including more energy group calculations).

The version of AGENT which allows optimized analysis of large assemblies is called Multi-AGENT. To initiate Multi-AGENT, the unit cell geometry and materials are defined with the associated cross sections from Scale (determined using ENDF microscopic cross section libraries). An array of 2D unit cells, which each may have the

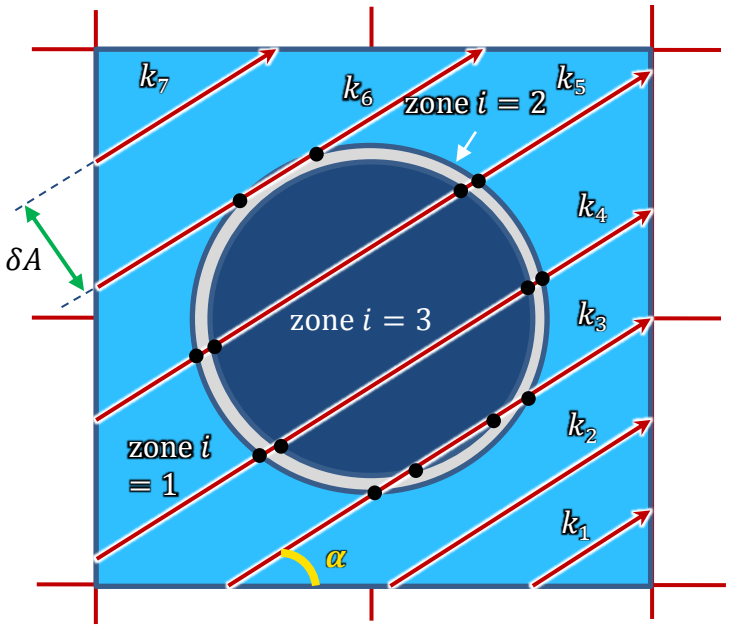

Figure 2.1. Ray tracing discretization of a single unit cell used by AGENT 2D solver (adapted from Eklund et al., 2015).

same or different cross section definitions, is created and extruded to develop a 3D assembly. In a simultaneous coupling scheme, Multi-AGENT solves the neutron transport equation first using MOC in 2D for several radial planes along the height of the assembly. Rays are extended separately in each plane and the neutron flux at the edges is calculated. Once the neutron flux distribution is known for each radial plane, the neutron leakage between the 2D planes for each pin is then calculated using MOC in a 1D axial scheme by separating the 3D assembly into separate 1D pins. A separate MOC solver is used for each scheme to calculate the outgoing neutron flux and transverse neutron leakage values. The separate 1D and 2D MOC solvers, each with a different arrangement of characteristic rays, transmit the interfacing transverse neutron leakage values between planes. This coupling scheme between the 2D radial and 1D axial MOC solvers allows for a full 3D core solution of the reactor power profile and neutron flux distribution. Figure 2.2 gives an overview of the Multi-AGENT 1D to 2D coupling process.

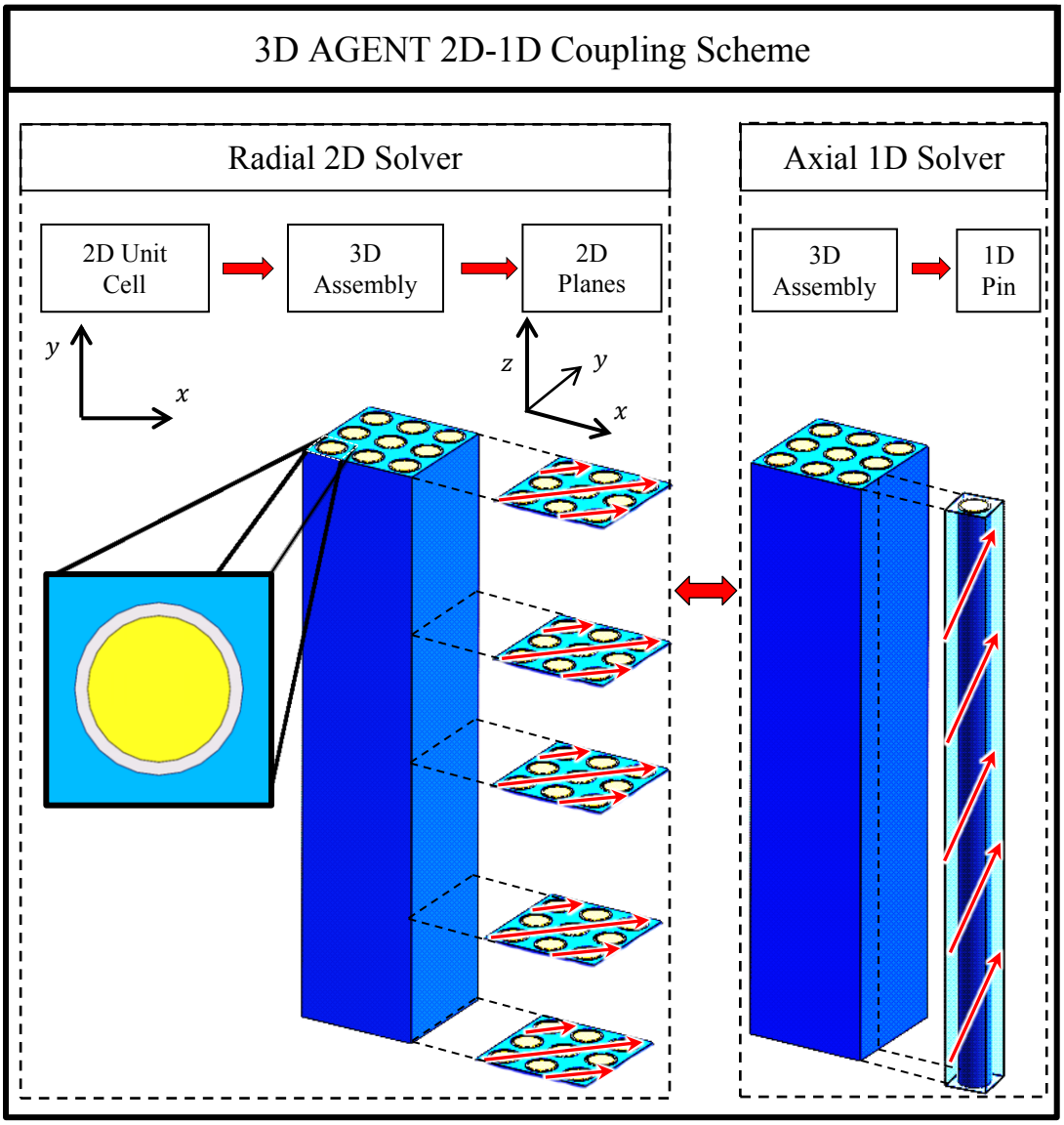

Figure 2.2. Overview of the 3D AGENT 2D radial/1D axial solver coupling scheme (adapted from Eklund et al., 2015).

The equations employed by the 2D MOC solver in AGENT are developed, followed by the 1D solver equations. Starting with the time-dependent neutron transport equation as taken from Duderstadt & Hamilton (1976):

$$\frac{1}{v}\frac{\partial\Psi(\vec{r},E,\hat{\Omega},t)}{\partial t}+\hat{\Omega}\cdot\nabla\Psi(\vec{r},E,\hat{\Omega},t)+\Sigma(\vec{r},E)\Psi(\vec{r},E,\hat{\Omega},t)=Q(\vec{r},E,\hat{\Omega},t) \quad (2.1)$$

where t = time (s), v = neutron velocity (cm/s), Ψ = angular neutron flux (neutrons/cm^2-s), $\hat{\Omega}$ = angular direction vector of neutrons, Σ = total macroscopic cross section (cm^{-1}), $\vec{r}$ = position vector (cm), E = neutron energy (eV), Q = neutron source term (neutrons/cm^3-s).

Each term in Eq. (2.1) accounts for the entrance or exit of neutrons from the system under analysis. On the left-hand side, the first term accounts for the time-dependent change in neutrons in the system. The second term accounts for the loss or gain of neutrons in the system as they cross the system boundaries. The third term accounts for all neutron interactions with other particles within the system. Note that typically only neutron-nucleus interactions are considered, as neutrons, having a neutral charge, do not interact by the same manner with other charged particles. The remaining term on the right-hand side of Eq. (2.1) represents the neutrons produced by the neutron source, from which neutrons are produced within the system. The two major mechanisms by which neutrons may be produced, fission and scattering, are discussed farther along in this section.

Of more frequent interest in nuclear reactor systems is the steady-state operating condition of the system. Certainly, the transient operation of the reactor during startup

and shutdown is crucial to its design, however, its operation over the long term allows for calculation of fuel burnup, the areas of largest neutron flux, etc., where the power levels are usually at their maximum. To analyze the steady-state neutron transport equation, all time-dependent terms in Eq. (2.1) are removed and each of the remaining terms becomes time independent:

$$\hat{\Omega} \cdot \nabla \Psi(\vec{r}, E, \hat{\Omega}) + \Sigma(\vec{r}, E)\Psi(\vec{r}, E, \hat{\Omega}) = Q(\vec{r}, E, \hat{\Omega}) \tag{2.2}$$

A significant factor in the interaction between neutrons and other nuclei is the neutron velocity or energy. Note that each term in Eq. (2.2) is dependent on the neutron energy. Since neutron energies span a wide spectrum of values, from 0 eV to well over 1 MeV, it is impractical to account for every possible neutron energy when solving the neutron transport equation. To simplify the equation and reduce the total computational resources needed to evaluate Eq. (2.2), neutron energies are separated into discrete ranges, or "bins." This results in the multigroup neutron transport equation:

$$\hat{\Omega} \cdot \nabla \Psi_g(\vec{r}, \hat{\Omega}) + \Sigma_g(\vec{r})\Psi_g(\vec{r}, \hat{\Omega}) = Q_g(\vec{r}, \hat{\Omega}) \tag{2.3}$$

where the g subscripts represent a discrete energy group. The source term on the right-hand side of Eq. (2.3), instead of representing a continuous energy integral, now represents a summation of all energy groups from most energetic group 1 to the lowest-energy group G.

This transport equation, Eq. (2.3), is the basis for evaluating the behavior of neutrons

in the nuclear system. However, these equations are difficult to evaluate for an entire heterogeneous system all at once. Instead, the system is surveyed at the unit cell level (as shown in Figure 2.1) and at the assembly level (as shown in Figure 2.2) using many separate straight rays (as shown in Figures 2.1 and 2.2) along which the equation is discretized in space and evaluated. The equation (Eq. (2.3)) is also discretized and evaluated for a set number of neutron energy groups as defined by the user along each ray. As is discussed further in this chapter, the evaluated neutron transport equation for each ray will be taken into account to result in averaged weighted neutron flux for each region in the unit cell and assembly. This will be useful (as described in Chapter 3) when coupling the AGENT neutronics code to the TH thermal hydraulics code, as it will provide a normalized axial power distribution for each fuel pin in the assembly. These power profiles will affect the heat transferred to the coolant adjacent to the fuel pins, which will, in turn, affect the neutron cross sections and the normalized axial power profile. The coupling scheme between AGENT and the new thermal hydraulics code is described in detail in Chapter 3.

Returning to the neutron transport equation, Eq. (2.3), the two major mechanisms which contribute to the neutron density in the system are fission and scattering. The term on the right-hand side of Eq. (2.3) may be further developed using these two sources. Fission is considered an isotropic source while the scattering source may be considered an anisotropic source. Using these two source contributions, the total source is:

$$Q_g(\vec{r}) = F_g(\vec{r}) + S_g(\vec{r}) \tag{2.4}$$

The fission F_g and isotropic scattering S_g terms are defined as:

$$S_g(\vec{r}) = \frac{1}{4\pi}\sum_{g'} \Sigma_{s,g'\to g}(\vec{r})\phi_{g'}(\vec{r}) \tag{2.5}$$

$$F_g(\vec{r}) = \frac{\chi_g(\vec{r})}{4\pi k_{eff}}\sum_{g'} \nu\Sigma_{f,g'}(\vec{r})\phi_{g'}(\vec{r}) \tag{2.6}$$

where each term equals, with respect to energy group g': $\phi_{g'}(\vec{r}) = \int_{4\pi} \Psi_{g'}(\vec{r},\hat{\Omega}')\ d\hat{\Omega}'$ = scalar flux of group g' (cm^2-s), $\Sigma_{s,g'\to g}(\vec{r})$ = macroscopic isotropic scattering cross section from neutron energy group g' to group g (cm^{-1}), ν = average number of neutrons released per fission event, $\Sigma_{f,g'}(\vec{r})$ = macroscopic fission cross section of group g' (cm^{-1}), $\chi_g(\vec{r})$ = fission spectrum for group g, k_{eff} = effective neutron multiplication factor.

The neutron transport equation is evaluated for 2D planes. An assumption used by the AGENT code is that the thickness of each of these planes is assumed to be infinite, termed the Infinite Thick Plane Approximation. The multigroup 2D transport equation, including leakage in the axial direction, is equal to:

$$\left(\sin\theta\cos\alpha\frac{\partial}{\partial x} + \sin\theta\sin\alpha\frac{\partial}{\partial y}\right)\Psi_g(\vec{r}^{2D},\hat{\Omega}) + \Sigma_g(\vec{r}^{2D})\Psi_g(\vec{r}^{2D},\hat{\Omega}) = Q_g(\vec{r}^{2D},\hat{\Omega}) - TL_g^{Axial}(\vec{r}^{2D},\hat{\Omega}) \tag{2.7}$$

where θ = polar angle, α = azimuthal angle, TL_g^{Axial} = transverse neutron leakage term

(neutrons/cm^3). The 2D superscript indicates the equation is evaluated using the 2D solver.

The advantage of MOC is the ability to reduce PDEs to ODEs, as described previously in this section. To reduce Eq. (2.7) to an ODE, straight characteristic rays are applied in the direction of $\hat{\Omega}(\alpha, \theta)$. The transport equation is evaluated along each characteristic ray separately. Thus, Eq. (2.7) is evaluated along the single characteristic ray s:

$$\frac{d}{ds}\left(\Psi_g\left(\vec{r}^{\,2D}, \hat{\Omega}\right)\right) + \Sigma_g(\vec{r}^{\,2D})\Psi_g\left(\vec{r}^{\,2D}, \hat{\Omega}\right) = Q_g\left(\vec{r}^{\,2D}, \hat{\Omega}\right) - TL_g^{Axial}\left(\vec{r}^{\,2D}, \hat{\Omega}\right) \quad (2.8)$$

A solution is resolved from Eq. (2.8) by angular and spatial discretization.

To increase the accuracy of the evaluation of the neutron transport equation by AGENT using MOC, the angular and spatial discretization must be refined. The system under analysis is subdivided into finite zones. For each zone, it is assumed that macroscopic cross sections, scalar neutron flux, and material properties are homogeneous. It is assumed that these properties are constant, independent of the polar and azimuthal angles of the characteristic rays. As a result, the source term is assumed to be constant and the cross sections are dependent on the neutron energy groups and zone. To refine the system subdivision, Eq. (2.8) is discretized along azimuthal and polar angles (denoted by subscripts az and pol, respectively). Multiple parallel characteristic rays, each indexed by subscript k, are separated by a distance δA as shown in Figure 2.1. Angular neutron flux is calculated along the characteristic ray line k within zone i and

discretized by azimuthal angle α and polar angle θ. The line segment $s_{\alpha,\theta,i,k}$ is created by the intersection of ray with index k discretized along azimuthal angle α and polar angle θ within zone i. AGENT precalculates the projection of a segment in 2D as follows:

$$s_{\alpha,i,k} = s_{\alpha,\theta,i,k} \sin\theta \tag{2.9}$$

Using MOC on ray of index k, the radial neutron transport equation becomes:

$$\frac{d\Psi_{g,\alpha,\theta,i,k}}{ds_{g,\alpha,\theta,i,k}} + \Sigma_{g,i}\Psi_{g,\alpha,\theta,i,k} = Q_{g,i} - TL^{Axial}_{g,\alpha,\theta,i,k} \tag{2.10}$$

The source term becomes:

$$Q_{g,i} = \frac{1}{4\pi}\sum_{g'}\left(\Sigma_{s,g'\to g,i}\phi_{g',i} + \frac{\chi_{g,i}}{k_{eff}}\nu\Sigma_{f,g',i}\phi_{g',i}\right) \tag{2.11}$$

where $\Psi_{g,\alpha,\theta,i,k}$ = angular neutron flux of energy group g along characteristic ray of index k with azimuthal angle α and polar angle θ (neutrons/cm^2-s); $Q_{g,i}$ = isotropic neutron source term of energy group g and zone i (neutrons/cm^3-s); $TL^{Axial}_{g,\alpha,\theta,i}$ = transverse leakage term from axial solver of energy group g, azimuthal angle α , polar angle θ, and zone i (neutrons/cm^3-s).

On the left-hand side of Eq. (2.11) exist two terms, one a differential term, which are

dependent on angular neutron flux, Ψ. This prevents the usage of separation and integration to reduce the differential order of the equation. An alternate solution requires the utilization of an exponential factor. This may be used since the following mathematical equation applies:

$$\frac{d}{dx}(y\exp[\lambda x]) = y\lambda\exp[\lambda x] + \exp[\lambda x]\frac{dy}{dx} = \exp[\lambda x]\left(y\lambda + \frac{dy}{dx}\right) \tag{2.12}$$

where λ is an arbitrary constant, y is a dependent variable, and x is an independent variable. Integrating the left-hand side of the equation yields:

$$\int_{x_1}^{x_2} \frac{d}{dx}(y\exp[\lambda x])dx = y(x_2)\cdot\exp[\lambda x_2] - y(x_1)\cdot\exp[\lambda x_1] \tag{2.13}$$

where x_2 and x_1 are the upper and lower bounds of the integral, respectively. This allows for a simple mathematical manipulation to solve for dependent variable y. Applying the exponential factor method to Eq. (2.11) requires multiplication of an integrating factor on both sides of the equation:

$$\exp\left[\Sigma_{g,i}s\right]\left[\frac{d\Psi_{g,\alpha,\theta,i,k}}{ds_{g,\alpha,\theta,i,k}} + \Sigma_{g,i}\Psi_{g,\alpha,\theta,i,k}\right] = \exp\left[\Sigma_{g,i}s\right]\left[Q_{g,i} - TL_{g,\alpha,\theta,i}^{Axial}\right] \tag{2.14}$$

$$\Rightarrow \frac{d}{ds}\left(\Psi_{g,\alpha,\theta,i,k}\exp\left[\Sigma_{g,i}s\right]\right) = \exp\left[\Sigma_{g,i}s\right]\left(Q_{g,i} - TL_{g,\alpha,\theta,i}^{Axial}\right) \tag{2.15}$$

Integrating each side:

$$\int_0^{s'} \frac{d}{ds}\left(\Psi_{g,\alpha,\theta,i,k}\exp\left[\Sigma_{g,i}s\right]\right)ds = \int_0^{s'} \exp\left[\Sigma_{g,i}s\right]\left(Q_{g,i} - TL_{g,\alpha,\theta,i}^{Axial}\right)ds \qquad (2.16)$$

$$\Rightarrow \Psi_{g,\alpha,\theta,i,k}(s')\exp\left[\Sigma_{t,g}s'\right] = \Psi_{g,\alpha,\theta,i,k}(0)$$

$$+\frac{\exp\left[\Sigma_{g,i}s'\right]}{\Sigma_{g,i}}\left(Q_g(s') - TL_{g,\alpha,\theta,i}^{Axial}(s')\right) - \left(Q_g(0) - TL_{g,\alpha,\theta,i}^{Axial}(0)\right) \qquad (2.17)$$

Solving for neutron flux at ray segment s':

$$\Psi_{g,\alpha,\theta,i,k}(s') = \Psi_{g,\alpha,\theta,i,k}(0)\exp\left[-\Sigma_{t,g,i}s'_{\alpha,\theta,i,k}\right] + \frac{Q_g(s') - TL_{g,\alpha,\theta,i}^{Axial}(s')}{\Sigma_{t,g,i}} \qquad (2.18)$$

A weighting function, ω, allows calculation of the average scalar flux, ϕ:

$$\phi_{g,\alpha,\theta,i,k}(s') = \sum_{m=1}^{M} \omega_m \overline{\Psi}_{g,\alpha,\theta,i,k}(s') \qquad (2.19)$$

where $\overline{\Psi}$ is the average angular neutron flux (neutrons/cm^2-s).

As done with the 2D radial solver, the equations used in the 1D axial solver are addressed. Similarly with the previous section, the AGENT 1D axial solver equations are based on the work of Xiao (2009) which presents these equations in detail. It is assumed that the pin cells evaluated by the 1D axial solver have an infinite radius and are homogeneous; this assumption is called the Infinite Homogenized Pin-Cell

Approximation. Each axial cell uses the following cross section equations:

1D Transport cross section:

$$\Sigma_{g,p}^{1D} = \frac{\sum_{i \in P} \Sigma_{g,i} A_i \phi_{g,i}}{\sum_{i \in P} A_i \phi_{g,i}} \tag{2.20}$$

1D Scattering cross section:

$$\Sigma_{s,g' \to g,p}^{1D} = \frac{\sum_{i \in P} \Sigma_{s,g' \to g,i} A_i \phi_{g,i}}{\sum_{i \in P} A_i \phi_{g,i}} \tag{2.21}$$

1D Nu-fission cross section:

$$\nu\Sigma_{f,g,p}^{1D} = \frac{\sum_{i \in P} \nu\Sigma_{f,g,i} A_i \phi_{g,i}}{\sum_{i \in P} A_i \phi_{g,i}} \tag{2.22}$$

where $\Sigma_{g,i}$ = macroscopic neutron transport cross section for group g and zone i (cm^{-1}); $\phi_{g,i}$ = scalar neutron flux of group g and zone i from 2D radial solver; $\Sigma_{s,g' \to g,i}$ = macroscopic neutron scattering cross section from group g' to group g in zone i (cm^{-1}); $\Sigma_{f,g,i}$ = macroscopic fission cross section of group g within zone i (cm^{-1}); A_i = 2D area of zone i (cm^2); $\sum_{i \in P}$ = summation for all zones within pin cell p, ν = average number of neutrons released per fission.

The characteristic rays are discretized along azimuthal angle α and polar angle θ. The

1D transport equation then becomes:

$$\frac{d}{ds}\Psi_{g,\alpha,\theta,p}^{1D} + \Sigma_{g,p}^{1D}\Psi_{g,\alpha,\theta,p}^{1D} = Q_{g,p}^{1D} - TL_{g,\alpha,\theta,p}^{Radial} \tag{2.23}$$

where $\Psi_{g,\alpha,\theta,p}^{1D}$ = angular neutron flux of energy group g, azimuthal angle α, polar angle θ, and pin cell p (neutrons/cm^2-s); $Q_{g,p}^{1D}$ = isotropic source term of energy group g and pin cell p (neutrons/cm^3-s); $TL_{g,\alpha,\theta,p}^{Radial}$ = transverse leakage term from radial solver of energy group g, azimuthal angle α , polar angle θ, and pin cell p (neutrons/cm^3-s).

The isotropic source for the 1D axial solver becomes:

$$Q_{g,p}^{1D} = \frac{1}{4\pi}\sum_{g'}\left(\Sigma_{s,g'\to g,p}^{1D} + \frac{\chi_{g,p}}{k_{eff}}\nu\Sigma_{f,g',p}^{1D}\phi_{g,p}^{1D}\right) \tag{2.24}$$

where $\chi_{g,p}$ = the neutron fission spectrum for group g and pin cell p. The $1D$ superscript and p and g subscripts apply as in previous equations.

The solution for the AGENT 1D axial equations is now approached. Since the axial neutron leakage term, $TL_{g,az,pol,i}^{Axial}$, is independent of azimuthal angle, α, the associated subscript may be removed only from this term. This is applicable under the Infinite Homogenized Pin-cell Approximation. At location s for characteristic ray of index k, the 2D radial transport equation allows for a solution of the angular neutron flux:

$$\Psi_{g,\alpha,\theta,i,k}(s) = \Psi_{g,\alpha,\theta,i,k}(0)\exp\left[-\Sigma_{g,i}s\right] + \frac{Q_{g,p}^{1D} - TL_{g,\theta,i}^{Axial}}{\Sigma_{g,i}}\left(1 - \exp\left[-\Sigma_{g,i}s\right]\right) \tag{2.25}$$

where $\Psi_{g,\alpha,\theta,i,k}$ = angular neutron flux of energy group g, azimuthal angle α , polar angle θ, zone i, and characteristic ray of index k (neutrons/cm^2-s); $\Sigma_{g,i}$ = macroscopic neutron transport cross section of energy group g and zone i (cm^{-1}).

On segment length $s_{\alpha,\theta,i,k}$ with azimuthal angle α, polar angle θ, zone i, and characteristic ray k, the average angular neutron flux is:

$$\bar{\Psi}_{g,\alpha,\theta,i,k} = \frac{1}{s_{\alpha,\theta,i,k}} \int_0^{s_{\alpha,\theta,i,k}} \Psi_{g,\alpha,\theta,i,k}(s)ds \tag{2.26}$$

$$= \frac{1}{s_{\alpha,\theta,i,k}} \int_0^{s_{\alpha,\theta,i,k}} \left[\Psi_{g,\alpha,\theta,i,k}(0)\exp[-s] + \frac{Q_{g,i} - TL_{g,\theta,i}^{Axial}}{\Sigma_{g,i}}\left(1 - \exp\left[-\Sigma_{g,i}s\right]\right)\right] ds \tag{2.27}$$

$$= \frac{1}{s_{\alpha,\theta,i,k}\Sigma_{g,i}} \begin{bmatrix} \Psi_{g,\alpha,\theta,i,k}(0)\left(1 - \exp\left[-\Sigma_{g,i}s\right]\right) + \left(Q_{g,i} - TL_{g,\theta,i}^{Axial}\right)s_{\alpha,\theta,i,k} \\ -\frac{Q_{g,i} - TL_{g,\theta,i}^{Axial}}{\Sigma_{g,i}}\left(1 - \exp\left[-\Sigma_{g,i}s_{\alpha,\theta,i,k}\right]\right) \end{bmatrix} \tag{2.28}$$

$$= \frac{1}{s_{\alpha,\theta,i,k}\Sigma_{g,i}}\left[\Psi_{g,\alpha,\theta,i,k}(0) - \Psi_{g,\alpha,\theta,i,k}\left(s_{\alpha,\theta,i,k}\right) + \left(Q_{g,i} - TL_{g,\theta,i}^{Axial}\right)s_{\alpha,\theta,i,k}\right] \tag{2.29}$$

The Greek symbol delta (Δ) is introduced to represent the change in angular neutron flux along the segment $s_{\alpha,\theta,i,k}$:

$$\Delta_{g,\alpha,\theta,,i,k} = \Psi_{g,\alpha,\theta,i,k}(0) - \Psi_{g,\alpha,\theta,i,k}\left(s_{\alpha,\theta,i,k}\right) \tag{2.30}$$

This equation reduces to:

$$\bar{\Psi}_{g,\alpha,\theta,i,k} = \frac{Q_{g,i} - TL_{g,\theta,i}^{Axial}}{\Sigma_{g,i}} + \frac{\Delta_{g,\alpha,\theta,i,k}}{s_{\alpha,\theta,i,k}\Sigma_{g,i}} \tag{2.31}$$

The ray separation distance δA (cm) is multiplied by the sum of the mean angular neuron flux and by the segment length $s_{\alpha,\theta,i,k}$ in the following equation. It is also weighted by the multiplication of the segment length and ray separation distance along characteristic rays of index k. This results in the average angular neutron flux:

$$\bar{\Psi}_{g,az,pol,i} \equiv \frac{\sum_k \bar{\Psi}_{g,az,pol,i,k} s_{az,i,k} \delta A}{\sum_k s_{az,i,k} \delta A} \tag{2.32}$$

The Infinite Thick Plane Approximation is once again invoked:

$$s_{\alpha,\theta,i,k} = \frac{s_{\alpha,i,k}}{\sin(\theta)} \tag{2.33}$$

The two equations, Eq. (2.31) and Eq. (2.32), are now combined:

$$\bar{\Psi}_{g,\alpha,\theta,i} = \frac{1}{\sum_k s_{\alpha,i,k}\delta A} \sum_k \left(\frac{Q_{g,i} - TL_{g,\theta,i}^{Axial}}{\Sigma_{g,i}} + \frac{\Delta_{g,\alpha,\theta,i,k}}{s_{\alpha,\theta,i,k}\Sigma_{g,i}} \right) s_{\alpha,i,k}\delta A \tag{2.34}$$

$$= \frac{Q_{g,i} - TL_{g,\theta,i}^{Axial}}{\Sigma_{g,i}} + \frac{1}{\Sigma_{g,i}\left(\sum_k s_{\alpha,i,k}\delta A\right)} \sum_k \Delta_{g,\alpha,\theta,i,k} \left(\frac{s_{\alpha,i,k}}{s_{\alpha,\theta,i,k}} \right) \delta A \tag{2.35}$$

And combining Eq. (2.33) with Eq. (2.35):

$$\bar{\Psi}_{g,\alpha,\theta,i} = \frac{Q_{g,i} - TL_{g,\theta,i}^{Axial}}{\Sigma_{g,i}} + \frac{\sin(\theta)\sum_k \Delta_{g,\alpha,\theta,i,k}\delta A}{\Sigma_{g,i}\left(\sum_k s_{\alpha,i,k}\delta A\right)} \tag{2.36}$$

The term $\sum_k s_{\alpha,i,k}\delta A$ (cm^2), which represents the area of zone i, is replaced by the true area A_i which results in the following simplification:

$$\bar{\Psi}_{g,\alpha,\theta,i} = \frac{Q_{g,i} - TL_{g,\theta,i}^{Axial}}{\Sigma_{g,i}} + \frac{\sin(\theta)\sum_k \Delta_{g,\alpha,\theta,i,k}\delta A}{\Sigma_{g,i}A_i} \tag{2.37}$$

The parameter $\phi_{g,i}$, or the average scalar zone flux of group g and zone i, may be rewritten by invoking the Flat Zone Approximation. This assumes that each zone has a constant scalar neutron flux and material properties, including macroscopic cross sections:

$$\phi_{g,i} = 4\pi \sum_\alpha \sum_\theta \omega_\alpha \omega_\theta \bar{\Psi}_{g,\alpha,\theta,i} \tag{2.38}$$

$$= 4\pi \left[\frac{Q_{g,i} - \sum_\theta \omega_\alpha TL_{g,\theta,i}^{Axial}}{\Sigma_{g,i}} + \frac{1}{\Sigma_{g,i}A_i} \sum_\alpha \sum_\theta \omega_\alpha \omega_\theta \sin(\theta) \sum_k \Delta_{g,\alpha,\theta,i,k}\delta A \right] \tag{2.39}$$

where ω_α = weight of azimuthal angles α and ω_θ = weight of polar angles θ. By default, AGENT sets these weights equal to one.

The radial leakage term is now introduced. Using the Homogenized Radial Leakage Approximation, where it is assumed that radial leakage is homogeneous in all directions,

the radial leakage term for group g and pin cell p in AGENT is calculated as:

$$TL_{g,p}^{Radial} = \sum_{\alpha}\sum_{\theta} \omega_{\alpha}\omega_{\theta} TL_{g,\alpha,\theta,p}^{Radial} \tag{2.40}$$

$$= \frac{1}{h_x}\sum_{\alpha} \omega_{\alpha} \cos(\alpha\,) \sum_{\theta} \omega_{\theta} \sin(\theta) \left(\Psi_{g,\alpha,\theta,p}^{S_2} - \Psi_{g,\alpha,\theta,p}^{S_4}\right)$$

$$+ \frac{1}{h_y}\sum_{\alpha} \omega_{\alpha} \sin(\alpha\,) \sum_{\theta} \omega_{\theta} \sin(\theta) \left(\Psi_{g,\alpha,\theta,p}^{S_3} - \Psi_{g,\alpha,\theta,p}^{S_1}\right) \tag{2.41}$$

where $\Psi_{g,\alpha,\theta,p}^{S_1}$, $(i = 1, 2, 3, 4)$ is the side-averaged angular flux at side i on the rectangular boundary edges. The index i refers to each edge beginning on the point nearest to the origin in the first quadrant of the $x - y$ plane, with the remaining indices denoting the remaining sides as rotated counter-clockwise. The side-averaged angular flux is used to determine the axial neutron leakage term. The terms h_x and h_y are the dimensions on the x and y axes, respectively, at which the neutron transport equation is integrated along the $x - y$ plane.

The 2D/1D MOC coupling equations are now considered. The methodology for solving Eq. (2.23), the 1D MOC transport equation, is similar to that done with the 2D MOC equation. Employing the Infinite Homogenized Pin-cell and Homogenized Radial Leakage Approximation, Eq. (2.23) becomes independent of all azimuthal angles. Eq. (2.23) is then solved along a polar direction:

$$\Psi_{g,\theta,p}^{1D}(s) = \Psi_{g,\theta,p}^{1D}(0)\exp\left[-\Sigma_{g,p}^{1D}s\right] + \frac{Q_{g,p}^{1D} - TL_{g,p}^{Radial}}{\Sigma_{g,i}^{1D}}\left(1 - \exp\left[-\Sigma_{g,p}^{1D}s\right]\right) \quad (2.42)$$

The average angular flux of segment $s_{\theta,p}$ for polar angle θ and pin cell p is calculated as:

$$\bar{\Psi}_{g,\theta,p}^{1D} = \frac{Q_{g,p}^{1D} - TL_{g,p}^{Radial}}{\Sigma_{g,p}^{1D}} + \frac{\Delta_{g,\theta,p}^{1D}}{s_{\theta,p}\Sigma_{g,p}^{1D}} \quad (2.43)$$

where:

$$\Delta_{g,\theta,p}^{1D} = \Psi_{g,\theta,p}^{1D}(0) - \Psi_{g,\theta,p}^{1D}\left(s_{\theta,p}\right) \quad (2.44)$$

The scalar flux for pin cell p and group g is calculated as:

$$\phi_{g,p}^{1D} = 4\pi\sum_{\theta}\omega_{\theta}\bar{\Psi}_{g,\theta,p} \quad (2.45)$$

$$= \frac{4\pi}{\Sigma_{g,p}^{1D}}\left[\left(Q_{g,p}^{1D} - TL_{g,p}^{Radial}\right) + \sum_{\theta}\omega_{\theta}\frac{\Delta_{g,\theta,p}^{1D}}{s_{\theta,p}}\right] \quad (2.46)$$

$$= \frac{4\pi}{\Sigma_{g,p}^{1D}}\left[\left(Q_{g,p}^{1D} - TL_{g,p}^{Radial}\right) + \frac{1}{h_{z,p}}\sum_{\theta}\omega_{\theta}\cos(\theta)\,\Delta_{g,\theta,p}^{1D}\right] \quad (2.47)$$

where $h_{z,p}$ = length of pin cell p in z direction (cm).

The equations Eq. (2.43) and Eq. (2.45) were developed and reduced as done with Eq. (2.37) and Eq. (2.38), respectively.

The axial neutron leakage, $TL_{g,\theta,i}^{Axial}$ for energy group g, polar angle θ, and zone i is calculated thus:

$$TL_{g,\theta,i}^{Axial} = \frac{\cos(\theta)}{h_{z,p}}\left(\Psi_{g,\theta,p}^{1D,Top} - \Psi_{g,\theta,p}^{1D,Bottom}\right), \qquad \forall i \in p \tag{2.48}$$

where $\Psi_{g,\theta,p}^{1D,Top}$, $\Psi_{g,\theta,p}^{1D,Bottom}$= angular neutron flux at top and bottom of pin cell, respectively, from the 1D axial solver (neutrons/cm^2-s). The leakage term is shared between zones i which share the same pin cell.

As briefly introduced, the MOC solution requires optimizing the energy and spatial discretization in use by the AGENT code. While an accurate result will typically be found by greatly increasing the number of energy groups, polar and azimuthal angles, decreasing ray separation, etc., it may take much longer than is necessary to reach a sufficient approximation. An optimization of space and energy discretization parameters requires performing a survey at the smaller assembly or unit cell level, whereby each discretization parameter is modified one at a time and the criticality calculations compared to find an optimum setting, taking into account accuracy and computational resources, including computation time. Using these optimized settings for a large assembly will prevent excessive refinement of spatial and energy group discretization than is needed to achieve sufficiently accurate converged flux rates and multiplication factors.

It is assumed that heterogeneity in the radial direction exceeds that in the axial direction (Xiao 2009). If valid, this results in an extremely effective 2D/1D coupling, as performed by AGENT. This requires a higher number of characteristic rays in the 2D radial solver than in the 1D axial solver. Thus, there is a higher number of characteristic rays used in the radial directions, x and y, than in the axial direction z, as shown in Figure 2.1. The number of characteristic rays in the x direction on a 2D plane, nx, and in the y direction, ny, is on the order of n for a given ray separation, or:

$$nx \sim O(n) \tag{2.49}$$

$$ny \sim O(n) \tag{2.50}$$

For the axial, or z, direction, the number of characteristic, nz, is on the order of n:

$$nz \sim O(n) \tag{2.51}$$

Note that this only applies if the reactor design requires this level of heterogeneity. However, if a higher heterogeneity is assumed in the radial direction rather than the axial direction (as described previously), the number of characteristic rays along the axial direction may be of an order lower:

$$nz \sim 1 \tag{2.52}$$

In this case, the total number of rays in 3D, $nray_{3D}$, would be on the order of the

square of n:

$$nray_{3D} \sim O(n^2) \tag{2.53}$$

While the AGENT MOC solver is very accurate for calculating and outputting neutron flux, normalized fission rates, reaction rates, and other neutronics parameters for a nuclear system, it does not take into account the effect of coolant temperature on the system's performance. An increase of coolant temperature will occur with an increase of the temperature of the fuel. Increased coolant temperatures lead to higher coolant void fractions and may change the type of coolant flow from single-phase to dispersed bubbly flow, churn or slug flow, annular flow, etc. Figure 2.3 displays these four main types of two-phase flow found in a vertical heated channel (Todreas & Kazimi, 1990). For most nuclear reactors with fuel elements designed with a negative temperature coefficient of reactivity, α_T (not to be confused with the previous use of alpha for azimuthal angle), will result in a reduction of reactivity of the system with a fuel temperature increase.

The previous lack of temperature feedback capability in AGENT led to the need for the development of a new thermal-hydraulic code. The new code requires that these thermal feedback effects are accounted for when calculating LWR system criticality. The TH code, explained in detail in the following section, is developed to model both BWR and PWR systems to fulfill this requirement.

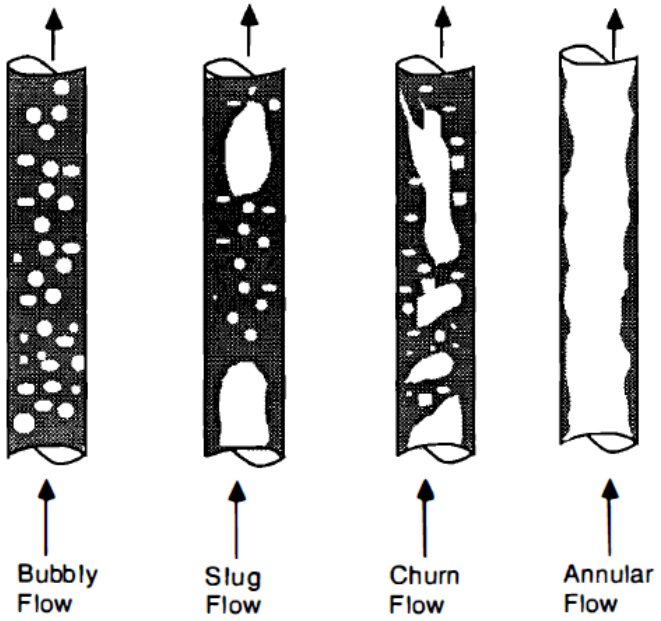

Figure 2.3. Visual representation of four different types of two-phase flow in a vertical heated channel (Todreas & Kazimi, 1990). From left to right are displayed bubbly, slug, churn, and annular flow. The dark areas represent the liquid phase and the blank (white) areas in the pipe represent the vapor (gaseous) phase.

CHAPTER 3

TH THERMAL HYDRAULICS CODE

3.1 Coolant Flow Properties

The behavior of nuclear reactors is largely governed by the reactivity of the system. There are many factors which affect reactivity (boron poison concentration, fuel burnup, control rod insertion, etc.) which may alter the overall reactor power profile and the total thermal power output. This thesis focuses on modeling the coupled behavior between the fluid flow in the reactor core and its effect on the reactor power profile. The fluid (water in the case for LWRs) is typically pumped through the lower plenum of the reactor core toward the upper plenum through multiple flow paths (i.e., coolant channels). Energy in the form of heat is transferred to the fluid as it passes through these coolant channels in an operating reactor. The amount of liquid in the fluid that is converted to vapor affects the flow properties, including velocity, heat transfer capabilities, etc. The effectiveness of the LWR reactor core at transferring heat to the moving fluid will ultimately determine the efficiency of the power generation system, which typically runs on a Rankine cycle. The temperature and behavior of the coolant also affects the temperature of the fuel pins, which affects their reactivity. Thus, these two processes are directly coupled. The fluid exiting the plenum will either directly turn an electric turbine generator for a single-coolant Rankine cycle or will transfer heat to a second coolant loop for a two-coolant

steam cycle. The fluid in the former case must then be condensed before being pumped again into the reactor while the latter, assumed to remain largely in the liquid phase at higher pressures, may be directly pumped back to the core.

The flow parameters that are crucial to the development of the TH thermal hydraulics code are presented within this section. These properties are used in subsequent sections within this chapter to develop the conservation equations which define the properties and behavior of the coolant in each LWR channel. Table 3.1 includes the most common thermodynamic and thermal-hydraulic variables and notations used throughout the equations in this chapter. Table 3.2 includes a list of common subscripts and superscripts employed in the equations throughout Chapters 3 and 4.

As a visual description of the types of forces acting on a channel's coolant, Figure 3.1 shows an example of annular fluid flow through the channel in direction z with velocity v. Forces due to wall shear and pressure, τ_w and p, respectively, are shown as acting on the fluid flow along with gravitational pull, g. The angle θ between the axis of fluid flow and the gravitational pull vector is assumed to be zero for heated LWR channels.

After introducing the fluid flow parameters, the drift flux parameters and relationships will be introduced. The conservation equations will then be introduced and integrated with the drift flux relations. Other important relations, such as the Net Vapor Generation (NVG) model, which accounts for subcooled nucleate boiling; heat conduction within a fuel pin utilizing equivalent thermal resistance circuits; the discretized finite difference equations used in the TH thermal hydraulics code; along with the AGENT/TH codes coupling scheme, are addressed in this section.

Table 3.1. Important thermal-hydraulic parameters in use with the TH thermal hydraulics code and their associated SI units (where applicable).

Variable	Description (SI Units/Value)	Variable	Description (SI Units/Value)
A	Flow Cross-Sectional Area (m^2)	Re	Reynolds Number
A_{rods}	Fuel Rods Cross-Sectional Area (m^2)	S	Slip Ratio
C_0	Concentration Parameter	St	Stanton Number
c_p	Specific Heat Capacity (J/kg-K)	t	Time (s)
D_e	Equivalent Heated Diameter (m)	u	Specific Internal Energy (J/kg)
D_h	Hydraulic Diameter (m)	V_{vj}	Effective Drift Velocity (m/s)
F_{wz}'''	Net Shear Force per Unit Volume (N/m^3)	$\overline{V_{vj}}$	Mean Drift Velocity (m/s)
f	Darcy Friction Factor	$\forall$	Total Volume (m^3)
f_{lo}	Liquid-Only Phase Friction Factor	$\forall_k$	Total Volume of Phase k (m^3)
f_{TP}	Two-Phase Friction Factor	v	Velocity (m/s)
f_{vo}	Vapor-Only Phase Friction Factor	v_{vj}	Vapor Drift Velocity (m/s)
G	Mass Flux (kg/m^2-s)	v	Specific Volume (m^3/kg)
g	Gravitational Constant($\cong$ 9.80665 m/s^2)	x	Flow Quality
h	Specific Enthalpy (J/kg)	x_e	Equilibrium Flow Quality
h_{conv}	Convection Heat Transfer Coefficient (W/m^2-K)	x_{NVG}	Net Vapor Generation Quality
j	Superficial Velocity (m/s)	x_{st}	Static Quality
K	Form Loss Coefficient		
k	Thermal Conductivity (W/kg-K)	**Greek Letters and Other Symbols**	
m	Fluid Mass (kg)	α	Void Fraction
$\dot{m}$	Mass Flow Rate (kg/s)	θ	Angle Between Direction of Flow and Gravitational Vector
Nu	Nusselt Number	μ	Dynamic Viscosity (Pa-s)
P_c	Critical Pressure (water: $P_c \cong 22.06(10^6)$ Pa)	ν	Kinematic Viscosity (m^2-s)
P_h	Heated Perimeter of Fuel Rod (m)	ρ	Density (kg/m^3)
P_w	Wetted Perimeter (m)	σ	Surface Tension of Liquid (N/m)
Pe	Peclet Number	$\bar{\bar{\tau}}$	Stress Tensor (Pa)
Pr	Prandtl Number	τ_w	Wall Shear Stress (Pa)
p	Pressure (Pa)	ϕ^2	Friction Pressure Drop Parameter
Δp_{acc}	Pressure Drop Flow Acceleration (Pa)	χ_f^j	Energy Deposited in Fuel per Fission Reaction of isotope j (J)
Δp_{fric}	Flow Friction Pressure Drop (Pa)	$(\partial p/\partial z)$	Pressure Gradient (Pa/m)
Δp_{grav}	Pressure Drop Due to Gravity (Pa)	$\vec{y}$	Vector of y
q'	Linear Heat Addition (W/m)	$\bar{y}$	Weighted/Mean Value of y
q''	Heat Flux (W/m^2)	$\{y\}$	Area-Averaged Value of y
q'''	Volumetric Heat Rate (W/m^3)	$\langle y \rangle$	Volume-Averaged Value of y
R_{rod}	Fuel Rod Radius (m)	$\tilde{y}$	Time-Averaged Value of y

Table 3.2. List and description of common subscripts and superscripts used in equations throughout Chapters 3 and 4.

Subscript/Superscript	Description
2ϕ	Two-Phase Parameter
D	Drift-flux Parameter
$cond$	Conduction Heat Transfer
$conv$	Convection Heat Transfer
f	Saturated Liquid
$fric$	Friction Flow Parameter
g	Saturated Vapor
k	Phase
l, lo	Liquid Phase
loc	Local Flow Parameter
m	Flow Mixture
NB	Nucleate Boiling Parameter
s	Parameter at Surface
sat	Parameter at Flow Saturation
TH	Thermal
TP	Two-Phase
v, vo	Vapor
z	1D Flow Direction
$+$	Dynamic/Mixing Cup

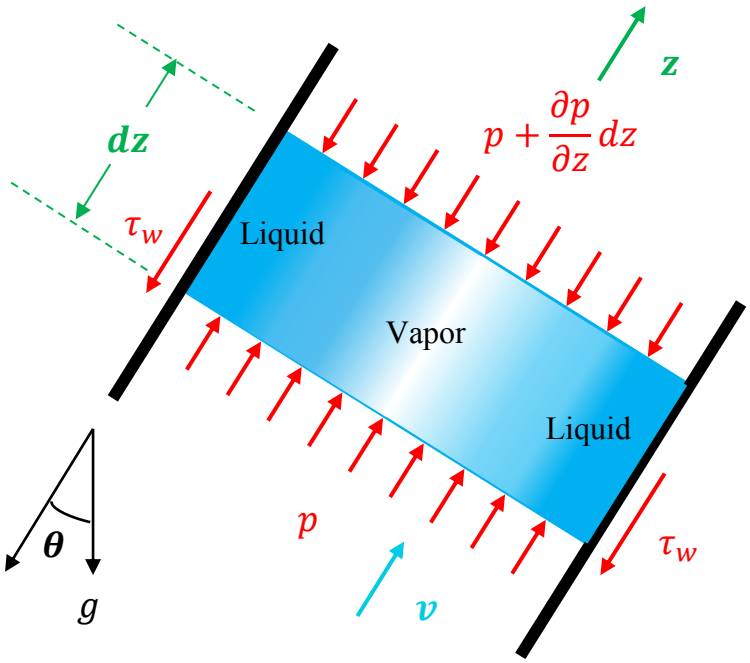

Figure 3.1. Annular fluid flow within a channel.

Before discussing the equations for the drift flux and HEM model parameters and assumptions, and combining them into the conservation equations, several flow properties and relations must be introduced. The flow properties may be averaged over space, time, or both. In a one-dimensional flow at steady state, instantaneous area-averaged quantities are typically used.

Two important operators are first discussed. The volume-averaged value of the flow property c_k for phase k is defined as follows:

$$\langle c_k \rangle = \frac{1}{\cancel{V}} \iiint_{\cancel{V}} c_k \, d\cancel{V} \tag{3.1}$$

where $\cancel{V_k}$ = volume of phase k (m^3) and $\cancel{V}$ = total volume (m^3).

The area-averaged value of the same property is defined as

$$\{c_k\} = \frac{1}{A} \iint_{A} c_k \, dA \tag{3.2}$$

where A_k = flow cross-sectional area of phase k (m) and A = total flow cross-sectional area (m).

An important flow property is the volumetric fraction of phase k to the total flow volume, symbolized using the lower-case Greek letter alpha $\langle \alpha_k \rangle$. The instantaneous void fraction averaged over the control volume is given as

$$\langle \alpha_k \rangle = \frac{1}{\cancel{V}} \iiint_{\cancel{V}} \alpha_k \, d\cancel{V} = \frac{\cancel{V_k}}{\cancel{V}} \tag{3.3}$$

Since there are two phases considered in this flow, the area taken up by the remaining phase k' may be used to redefine the previous equation:

$$\langle \alpha_k \rangle = \frac{\cancel{V_k}}{\cancel{V}} = \frac{\cancel{V_k}}{\cancel{V_k} + \cancel{V_{k'}}} \tag{3.4}$$

The volume fraction of the gaseous phase to the total flow volume is known as the void fraction, represented as simply $\langle \alpha \rangle$.

The following equation for this property demonstrates how the instantaneous area-averaged fraction of phase k would be shown:

$$\{\alpha_k\} \equiv \frac{A_k}{A} = \frac{1}{A} \iint_A \alpha_k \, dA \tag{3.5}$$

where the braces indicate it is averaged over the flow cross section. Similarly with the volume-averaged equation, the volume of the other phase k' allows the area-averaged void fraction to be defined as:

$$\{\alpha_k\} \equiv \frac{A_k}{A} = \frac{A_k}{A_k + A_{k'}} \tag{3.6}$$

If the area-averaged void fraction of phase k is at unity, the entire area at the axial flow location consists solely of that phase. If the area-averaged void fraction of phase k is zero, the area at the axial flow location is devoid of that phase. Written in mathematical terms, the boundaries of this property are

$$0 \leq \{\alpha_k\} \leq 1 \tag{3.7}$$

for all two-phase flows. It is for this reason that α_k may be referred to as the phase density function for phase k.

Throughout this document, the void fraction of the gaseous phase, α_v, is presented with no subscript (i.e., α) and will simply be referred to as the void fraction for brevity. If its area-averaged quantity is compared to the area-averaged void fraction of the liquid phase:

$$\{\alpha\} = \{1 - \alpha_l\} \tag{3.8}$$

Similarly, comparing the volume-averaged void fraction (or simply void fraction) with the liquid volume-averaged void fraction:

$$\langle\alpha\rangle = \langle 1 - \alpha_l \rangle \tag{3.9}$$

The mixture density of the two-phase fluid flow is defined as

$$\rho_m \equiv \alpha\rho_v + (1-\alpha)\rho_l = \rho_l + \alpha\rho_{lv} \tag{3.10}$$

where ρ_l = density of liquid phase (kg/m^3), ρ_v = density of vapor phase (kg/m^3), and the density difference between the liquid and vapor phases is:

$$\rho_{lv} = \rho_v - \rho_l \tag{3.11}$$

The mixture velocity is weighted by the mixture density:

$$v_m \equiv \frac{\{\rho_m v_m\}}{\{\rho_m\}} = \frac{\{\alpha\rho_v v_v + (1-\alpha)\rho_l v_l\}}{\{\rho_m\}} \tag{3.12}$$

where v_l = velocity of liquid phase (kg/m^3) and v_v = velocity of vapor phase (kg/m^3).

The dynamic (or mixing cup) density is defined as

$$\rho_m^+ \equiv \frac{G_m^2}{\{\rho_v \alpha v_{vz}^2 + \rho_l(1-\alpha)v_{lz}^2\}} \tag{3.13}$$

Two related and essential properties when studying two-phase flow are the static and flow qualities. The static quality is the instantaneous ratio of the volume-averaged gaseous phase to the total volume at any flow location:

$$x_{st} = \frac{\langle m_v \rangle}{\langle m \rangle} = \frac{\langle m_v \rangle}{\langle m_v + m_l \rangle} \tag{3.14}$$

where $\langle m_v \rangle$ = volume-averaged mass of gaseous phase (kg), $\langle m_l \rangle$ = volume-averaged mass of liquid phase (kg), and $\langle m \rangle$ = total volume-averaged mass (kg).

This equation may also be expressed as an area-averaged quantity:

$$x_{st} = \frac{\{m_v\}}{\{m\}} = \frac{\{m_v\}}{\{m_v + m_l\}} \tag{3.15}$$

where $\{m_v\}$ = area-averaged mass of gaseous phase (kg), $\{m_l\}$ = area-averaged mass of liquid phase (kg), and $\{m\}$ = total area-averaged mass (kg).

The static flow quality is so named as it is not dependent on the flow dynamics; it takes the area-averaged mass fraction of vapor to the total mixture at a moment in time or at steady-state.

The mass flow rate of phase k through area $\vec{A}_j$, which is normal to direction j, is equal to the following:

$$\dot{m}_{kj} = \iint_{A_j} \alpha_k \rho_k \vec{v}_k \cdot \vec{n} dA_j = \{\alpha_k \rho_k \vec{v}_k\}_j \cdot \vec{A}_j \tag{3.16}$$

where ρ_k = density of phase k (kg/m^3), $\vec{v}_k$ = vector velocity of phase k (m/s), and $\vec{n}$ = unit vector normal to area $\vec{A}_j$.

The following equation relates phase property average to total area property average:

$$\{c_k\} = \{c_k\}_k \{\alpha_k\} \tag{3.17}$$

where c_k and α_k are any flow property and void fraction of phase k, respectively. This allows the mass flow rate to be redefined as:

$$\dot{m}_{kj} = \{\rho_k \vec{v}_k\}_{kj}\{\alpha_k\}_j \cdot \vec{A}_j \tag{3.18}$$

The flow quality, also known as the vapor mass flow fraction of the total flow, or simply mass fraction, is defined in a one-dimensional flow in the z-direction as:

$$x_z \equiv \frac{\dot{m}_{vz}}{\dot{m}_z} = \frac{\dot{m}_{vz}}{\dot{m}_{vz} + \dot{m}_{lz}} \tag{3.19}$$

where $\dot{m}_{vz}$ = mass flow rate of vapor phase in the z-direction (kg/s), $\dot{m}_{lz}$ = mass flow rate of liquid phase in the z-direction (kg/s), and $\dot{m}_z$ = total mass flow rate in the z-direction (kg/s).

Specific internal energy, u (J/kg), describes the amount of thermal energy stored per unit mass of the coolant flow. Specific enthalpy, h (J/kg), is the addition of the fluid's specific internal energy to the work necessary to expand the fluid's boundary:

$$h = u + p\mathrm{v} = u + \frac{p}{\rho_m} \tag{3.20}$$

where v = fluid specific volume (m^3/kg) and p = flow pressure (Pa).

Note that this equation applies due to the following relationship:

$$\mathrm{v} = \frac{1}{\rho} \tag{3.21}$$

The specific flow (or mixing cup) enthalpy is defined as

$$h_m^+ \equiv x h_v + (1 - x) h_l \tag{3.22}$$

where h_v = specific enthalpy of vapor phase (J/kg) and h_l = specific enthalpy of liquid phase (J/kg).

Using these definitions, the flow thermodynamic (or equilibrium) quality is given as:

$$x_{eq} = \frac{h_m^+ - h_f}{h_g - h_f} \tag{3.23}$$

where h_f = specific enthalpy of saturated liquid (J/kg) and h_g = specific enthalpy of saturated vapor (J/kg).

As with mixture density, the difference between the liquid and vapor values for specific energy and enthalpy may be represented, respectively:

$$u_{lv} = u_v - u_l \tag{3.24}$$

$$h_{lv} = h_v - h_l \tag{3.25}$$

The saturated fluid properties are typically found from standardized tables as provided by the NIST website (2011) or another reliable experimental data source.

Mass flux, also known as superficial mass flux or mass velocity, is the mass of flow mixture or specific phase per unit area and time, or the mass flow rate per unit area. It is defined as:

$$G_k \equiv \frac{\dot{m}_{kj}}{A_j} \tag{3.26}$$

where G_k = mass flux of mixture or phase k in flow direction j (kg/m^2-s), $\dot{m}_{kj}$ = mass flow rate of mixture or phase k in flow direction j (kg/s), and A_j = cross-sectional area of fluid flow in direction j (m^2).

It may also be expressed using the equation for mass flow rate:

$$G_k \equiv \frac{\{\rho_k \vec{v}_k\}_{kj}\{\alpha_k\}_j \cdot \vec{A}_j}{A_j} = \{\rho_k v_{kj}\}_{kj}\{\alpha_k\}_j \tag{3.27}$$

where v_{kj} = velocity of fluid flow of phase or mixture k in direction j (m/s).

For the individual phases moving in the z-direction, the mass flux may be expressed as:

$$G_{lz} \equiv \frac{\dot{m}_{lz}}{A_z} = \frac{\dot{m}_z(1-x)}{A_z} = \{\rho_l v_{lz}\}_{lz}\{\alpha_l\}_z = \{\rho_l v_{lz}\}_{lz}\{1-\alpha\}_z \tag{3.28}$$

$$G_{vz} \equiv \frac{\dot{m}_{vz}}{A_z} = \frac{\dot{m}_z x}{A_z} = \{\rho_v v_{vz}\}_{vz}\{\alpha_v\}_z = \{\rho_v v_{vz}\}_{vz}\{\alpha\}_z \tag{3.29}$$

where G_{lz} = mass flux of liquid phase flow direction z (kg/s) and G_{vz} = mass flux of

vapor phase in flow direction z (kg/s).

The Reynolds number for the coolant mixture flow within a pipe is calculated as:

$$Re = \frac{GD_h}{\mu} = \frac{\rho v D_h}{\mu} = \frac{vD_h}{\nu} \tag{3.30}$$

where μ = dynamic viscosity (Pa-s), ν = kinematic viscosity (m^2-s), and D_h = hydraulic diameter.

The hydraulic diameter is calculated as:

$$D_h = \frac{4A_m}{P_w} \tag{3.31}$$

Note that the hydraulic diameter is used to calculate the Reynolds number and Nusselt number and is discussed in a following section.

The friction factor for operating LWRs is calculated using the McAdams relationship (Todreas & Kazimi, 1990) which is used to approximate the friction for a smooth tube. For Reynolds numbers ranging from 30,000 < Re < 1,000,000:

$$f = 0.184 \cdot Re^{-0.2} \tag{3.32}$$

For Reynolds numbers below 30,000, the Blasius relation may be used (Todreas & Kazimi, 1990):

$$f = 0.316 \cdot Re^{-0.25} \tag{3.33}$$

The quantity that is defined as the comparison between the area-averaged void fraction to the flow quality at any axial position along the coolant flow is known as the void-quality-slip ratio, or simply the slip ratio, S. It is the ratio of the time- and area-averaged phase velocities in direction i, as follows:

$$S_i = \frac{\{\widetilde{v_{v,i}}\}_v}{\{\widetilde{v_{l,i}}\}_l} \tag{3.34}$$

where the v and l subscripts indicate the vapor and liquid phases, respectively, and braces indicate an area-averaged quantity, with the tilde above the quantity representing a time-averaged quantity.

If time fluctuations in $\{\alpha\}$ are considered negligible, the slip ratio is found as:

$$S = \frac{x}{1-x}\frac{\rho_l}{\rho_v}\frac{\{1-\alpha\}}{\{\alpha\}} \tag{3.35}$$

Solving the above equation for the void fraction:

$$\{\alpha\} = \frac{1}{1 + \frac{1-x}{x}\frac{\rho_l}{\rho_v}S} \tag{3.36}$$

3.2 Drift Flux Relations

The velocity of the vapor phase may be redefined if introducing the superficial velocity, j:

$$v_v = j + (v_v - j) = j + v_{vj} \tag{3.37}$$

where j = superficial velocity (m/s) and v_{vj} = vapor drift velocity (m/s).

The superficial velocity of the vapor phase is defined as:

$$j_v \equiv \alpha v_v \tag{3.38}$$

Using the equation for vapor velocity to expand the vapor superficial velocity:

$$j_v = \alpha v_v + \alpha j - \alpha j \tag{3.39}$$

The vapor superficial velocity can be rearranged as follows:

$$j_v = \alpha j + \alpha(v_v - j) \tag{3.40}$$

$$\Rightarrow j_v = \alpha j + \alpha v_{vj} \tag{3.41}$$

When averaging this equation over the flow cross-sectional area:

$$\{j_v\} = \{\alpha j\} + \{\alpha v_{vj}\} \tag{3.42}$$

Similarly, the liquid superficial velocity is:

$$j_l \equiv (1-\alpha)v_l \tag{3.43}$$

Averaging each side over the flow area:

$$\{j_l\} = \{(1-\alpha)v_l\} \tag{3.44}$$

The total superficial velocity is simply the addition of the phasic superficial velocities:

$$j = j_v + j_l = \alpha v_v + (1-\alpha)v_l \tag{3.45}$$

The second term on the right-hand side of this equation is defined as the drift flux, J. It has similar dimensions as the superficial velocity and volumetric flux of distance divided by time. Introducing two new variables allows the vapor superficial velocity to be defined as follows:

$$\{j_v\} = C_0\{\alpha\}\{j\} + \{\alpha\}V_{vj} \tag{3.46}$$

where C_0 = concentration parameter and V_{vj} = effective drift velocity (m/s).

The effective drift velocity is defined as:

$$V_{vj} \equiv \frac{\{\alpha(v_v - j)\}}{\{\alpha\}} = \frac{\{\alpha v_{vj}\}}{\{\alpha\}} \tag{3.47}$$

and the concentration parameter is defined as:

$$C_0 \equiv \frac{\{\alpha j\}}{\{\alpha\}\{j\}} \tag{3.48}$$

Rearranging these equations to solve for the void fraction:

$$\{\alpha\} = \frac{\{j_v\}}{C_0\{j\} + V_{vj}} \tag{3.49}$$

The void fraction may be expressed by replacing terms for mass flow rate, mass flux, flow quality, and phase densities into Eq. (3.49):

$$\{\alpha\} = \frac{{}^{x\dot{m}}/_{\rho_v A}}{C_0\left(\frac{x}{\rho_v} + \frac{1-x}{\rho_l}\right) + \frac{V_{vj}\rho_v}{xG}} \tag{3.50}$$

A quantity known as the mean drift velocity is defined (Hibiki & Ishii, 2003; Hibiki & Ishii, 2005):

$$\overline{V_{vj}} \equiv v_v - \{j\} = (1 - \{\alpha\})(v_v - v_l) = V_{vj} + (C_0 - 1)\{j\} \tag{3.51}$$

This may be transformed into:

$$\overline{V_{vJ}} = \frac{\{j_v\}}{\{\alpha\}} - (\{j_v\} + \{j_l\}) \tag{3.52}$$

The definitions given for the drift velocity for annular two-phase flows (Hibiki & Ishii, 2003; Hibiki & Ishii, 2005) allow for several relations to be introduced. The phasic velocities may be represented as:

$$v_v = v_m + \frac{\rho_l}{\{\rho_m\}}\overline{V_{vJ}} \tag{3.53}$$

$$v_l = v_m - \frac{\{\alpha\}}{1-\{\alpha\}}\frac{\rho_v}{\{\rho_m\}}\overline{V_{vJ}} \tag{3.54}$$

The superficial velocity is the addition of these two, thus:

$$\{j\} = \{j_v\} + \{j_l\} = \{\alpha v_v\} + \{(1-\alpha)v_l\} \tag{3.55}$$

$$\Rightarrow \{j\} = \left\{\{\alpha\}\left(v_m + \frac{\rho_l}{\{\rho_m\}}\overline{V_{vJ}}\right)\right\} + (1-\{\alpha\})\left\{v_m - \frac{\{\alpha\}}{1-\{\alpha\}}\frac{\rho_g}{\{\rho_m\}}\overline{V_{vJ}}\right\} \tag{3.56}$$

$$\Rightarrow \{j\} = v_m + \overline{V_{vJ}}\left(\frac{\{\alpha\}\rho_l}{\{\rho_m\}} - (1-\{\alpha\})\frac{1}{1-\{\alpha\}}\frac{\{\alpha\}\rho_g}{\{\rho_m\}}\right) \tag{3.57}$$

$$\Rightarrow \{j\} = v_m + \overline{V_{vJ}}\left(\frac{\{\alpha\}\rho_l}{\{\rho_m\}} - \frac{\{\alpha\}\rho_g}{\{\rho_m\}}\right) \tag{3.58}$$

$$\Rightarrow \{j\} = v_m + \overline{V_{vJ}}\left(\frac{\{\alpha\}(\rho_l - \rho_g)}{\{\rho_m\}}\right) \tag{3.59}$$

These equations will be inserted into the conservation equations in the following section to derive the equations used in the finite difference model.

3.3 Conservation Equations

3.3.1 Mass Continuity

The equations from this section are taken from Todreas & Kazimi (1990) with additional developments and discussion.

Consider the one-dimensional flow through a plane of an area A_z at a position z along a channel. The mass balance equation is written as:

$$\frac{\partial}{\partial t}\iint_{A_z} \rho \, dA_z + \frac{\partial}{\partial z}\iint_{A_z} \rho v_z \, dA_z = 0 \tag{3.60}$$

or:

$$\frac{\partial}{\partial t}\{\rho_v \alpha + \rho_l(1-\alpha)\}A_z + \frac{\partial}{\partial z}\{\rho_v \alpha v_{vz} + \rho_l(1-\alpha)v_{lz}\}A_z = 0 \tag{3.61}$$

where v_z = mixture velocity in z-direction (m/s), v_{vz} = vapor velocity in z-direction (m/s), and v_{lz} = liquid velocity in z-direction (m/s).

The mixture mass flux, G_m (kg/m^2-s), is defined as follows:

$$G_{mz} \equiv \frac{\dot{m}_z}{A_z} = \frac{\dot{m}_{lz} + \dot{m}_{vz}}{A_z} = G_{lz} + G_{vz} \tag{3.62}$$

When inserting a term for average mixture density, ρ_m, and mass flux, G_m, over the area A_z, the previous equation may be written as:

$$\frac{\partial}{\partial t}(\rho_m A_z) + \frac{\partial}{\partial z}(G_m A_z) = 0 \tag{3.63}$$

Mass flux may be defined slightly differently than as given above:

$$G_m = \{\rho_v \alpha v_v + \rho_l (1-\alpha) v_l\} \tag{3.64}$$

For a single channel with a constant area A_z, the equation reduces to:

$$\frac{\partial \rho_m}{\partial t} + \frac{\partial}{\partial z}(G_m) = 0 \tag{3.65}$$

which can be also written as:

$$\frac{\partial \rho_m}{\partial t} + \frac{\partial}{\partial z}(\rho_m v_m) = 0 \tag{3.66}$$

Eq. (3.66) is restated since the following equation holds:

$$v_m = \frac{G_m}{\rho_m} \tag{3.67}$$

3.3.2 Momentum

The momentum equation for two-phase flow in one dimension along the z-direction is given as:

$$\frac{\partial}{\partial t}\iint_{A_Z}\rho v_z dA_z + \frac{\partial}{\partial z}\iint_{A_Z}\rho v_z^2 dA_z = -\iint_{A_Z}\frac{\partial p}{\partial z}dA_z - \int_{P_z}\tau_w dP_z - \iint_{A_Z}\rho g cos\theta dA_z \quad (3.68)$$

where τ_w = shear stress at the walls (Pa), P_z = perimeter of channel at location z (Pa), θ = angle between the channel and direction of gravitational vector, $\vec{g}$, and g = gravitational constant ≅ 9.80665 m/s^2.

Evaluating the equation for the separate phases:

$$\frac{\partial}{\partial t}\{\rho_v \alpha v_{vz} + \rho_l(1-\alpha)v_{lz}\}A_z + \frac{\partial}{\partial z}\{\rho_v \alpha\, v_{vz}^2 + \rho_l(1-\alpha)v_{lz}^2\}A_z$$

$$= -\left(\frac{\partial\{p\}A_z}{\partial z}\right) - \int_{P_z}\tau_w dP_z - \{\rho_v\alpha\ + \rho_l(1-\alpha)\}g cos\theta A_z \quad (3.69)$$

If pressure is assumed to be uniform in area A_z, this may be rewritten as:

$$\frac{\partial}{\partial t}\{\rho_v \alpha v_{vz} + \rho_l(1-\alpha)v_{lz}\}A_z + \frac{\partial}{\partial z}\{\rho_v \alpha\, v_{vz}^2 + \rho_l(1-\alpha)v_{lz}^2\}A_z$$

$$= -\left(\frac{\partial(pA_z)}{\partial z}\right) - \int_{P_z}\tau_w dP_z - \{\rho_v\alpha\ + \rho_l(1-\alpha)\}g cos\theta A_z \quad (3.70)$$

$$\Rightarrow \frac{\partial}{\partial t}(\rho_m A_z) + \frac{\partial}{\partial z}\{\rho_v \alpha\, v_{vz}^2 + \rho_l(1-\alpha)v_{lz}^2\}A_z$$

$$= -\left(\frac{\partial(pA_z)}{\partial z}\right) - \int_{P_z} \tau_w dP_z - \rho_m g cos\theta A_z \tag{3.71}$$

Replacing the shear stress term in the momentum equation as follows:

$$\frac{1}{A_z}\int_{P_z} \tau_w dP_z = \left(\frac{\partial p}{\partial z}\right)_{fric} \tag{3.72}$$

where the term on the right-hand side represents the friction pressure gradient. For two-phase flow, it can be related to the wall shear stress and momentum flux by terms analogous to the single-phase flow case as follows:

$$\left(\frac{\partial p}{\partial z}\right)_{fric} = \frac{\tau_w P_w}{A_z} = f\frac{G_m^2}{2D_h\rho_m} \tag{3.73}$$

If a) the area A_z is considered constant along the axial direction of a single coolant channel, b) the pressures of the two phases are roughly equal (i.e., $p_v \simeq p_l \simeq p_l$), and c) the terms for the shear stress, as given previously, are included, the momentum equation may be restated thus:

$$\frac{\partial G_m}{\partial t} + \frac{\partial}{\partial z}\{\rho_v \alpha\, v_{vz}^2 + \rho_l(1-\alpha)v_{lz}^2\} = -\frac{\partial p}{\partial z} - \frac{f G_m^2}{2D_h\rho_m} - \rho_m g cos\theta \tag{3.74}$$

In order to take two-phase pressure losses due to friction, a two-phase multiplier is added to the equation above. This will modify the single-phase friction factor to account for pressure losses due to both phases. The modified momentum equation follows:

$$\frac{\partial G_m}{\partial t} + \frac{\partial}{\partial z}\{\rho_v \alpha\, v_{vz}^2 + \rho_l(1-\alpha)v_{lz}^2\} = -\frac{\partial p}{\partial z} - \phi_{fric}^2 \frac{f G_m^2}{2D_h \rho_m} - \rho_m g cos\theta \quad (3.75)$$

where ϕ_{fric}^2 = two-phase friction pressure loss multiplier.

In Galloway's implementation of the Drift Flux model in NESTLE (2010), another term was added to account for pressure loss due to grid spacers. The pressure drop due to spacers (local pressure loss) follows a similar form to that from friction losses:

$$\Delta p_{local} = \phi_{local}^2 K \frac{G_m^2}{2\rho_l} \quad (3.76)$$

where Δp_{local} = local pressure loss (Pa), ϕ_{local}^2 = two-phase local loss multiplier, and K = user-defined single-phase local pressure loss coefficient.

The value for K_{local} is typically provided for an experimental setup. Slight modification of this term may be necessary to achieve satisfactory results.

Including this pressure loss term in the momentum equation above gives us:

$$\frac{\partial G_m}{\partial t} + \frac{\partial}{\partial z}\{\rho_v \alpha\, v_{vz}^2 + \rho_l(1-\alpha)v_{lz}^2\}$$
$$= -\frac{\partial p}{\partial z} - \phi_{fric}^2 \frac{f G_m^2}{2D_h \rho_m} - \frac{\partial}{\partial z}\left[\phi_{lo}^2 K \frac{G_m^2}{2\rho_l}\right] - \rho_m g cos\theta \quad (3.77)$$

Evaluating at steady-state conditions results in the following:

$$\frac{\partial}{\partial z}\{\rho_v \alpha\, v_{vz}^2 + \rho_l(1-\alpha)v_{lz}^2\}$$

$$= -\frac{\partial p}{\partial z} - \phi_{fric}^2 \frac{f G_m^2}{2 D_h \rho_m} - \frac{\partial}{\partial z}\left[\phi_{lo}^2 K \frac{G_m^2}{2\rho_l}\right] - \rho_m g cos\theta \tag{3.78}$$

As implemented in the NESTLE hydrodynamic model (Galloway, 2010), the Columbia relation is used for calculating the two-phase friction pressure loss multiplier:

$$\phi_{fric}^2 = 1 + \left(\frac{\rho_l}{\rho_g} - 1\right) Cx \tag{3.79}$$

where x = fluid flow quality and C = friction loss parameter.

The friction loss parameter C depends on the pressure of the axial location in the channel. If the flow pressure is greater than 600 psi (or approximately $4.14(10^6)$ Pa), the following is used:

$$C = 1.02 x^{-0.175} G_m^{-0.45} \tag{3.80}$$

Otherwise:

$$C = 0.357\left(1 + 10\frac{P}{P_c}\right) x^{-0.175} G_m^{-0.45} \tag{3.81}$$

where P_c = critical pressure.

For water, the critical pressure is approximately $22.06(10^6)$ Pa.

3.3.3 Energy Conservation

For the energy balance in one-dimensional flow:

$$\frac{\partial}{\partial t}\iint_{A_Z} \rho u dA_z + \frac{\partial}{\partial z}\iint_{A_Z} \rho h v_z dA_z = q' + \iint_{A_Z} q''' dA_z \tag{3.82}$$

where q' = linear heat addition from the walls (W/m) and q''' = volumetric heat generation rate in the coolant (W/m^3).

Note that the axial heat conduction and work terms are ignored. Since the control volume is fixed, there is no expansion work term. The surfaces along the walls, fuel elements, spacers, and any surface with which the fluid may come in contact are stationary. A small portion of the energy due to friction, pressure, and shear forces would be converted to heat. However, according to Todreas and Kazimi (1990), this heat is negligibly small and is usually ignored. Effects from gravity are likewise considered negligible.

The energy equation above may also be written as:

$$\frac{\partial}{\partial t}\iint_{A_Z} \rho h dA_z + \frac{\partial}{\partial z}\iint_{A_Z} \rho h v_z dA_z = \frac{\partial}{\partial t}\iint_{A_Z} \rho(pv) dA_z + q' + \iint_{A_Z} q''' dA_z \tag{3.83}$$

by employing the definition of enthalpy.

If p is assumed to be uniform over A_z:

$$\frac{\partial}{\partial t}(\{\rho_v \alpha h_v + \rho_l(1-\alpha)h_l\}A_z) + \frac{\partial}{\partial z}(\{\rho_v \alpha\, h_v v_{vz} + \rho_l(1-\alpha)h_l v_{lz}\}A_z)$$

$$= \left(\frac{\partial p}{\partial t}\right)A_Z + q' + \iint_{A_Z} q'''dA_z \tag{3.84}$$

If the kinetic energy of both phases is ignored:

$$\frac{\partial}{\partial t}(\rho_m h_m A_z) + \frac{\partial}{\partial z}(G_m h_m^+ A_z) = \left(\frac{\partial p}{\partial t}\right)A_Z + q' + \iint_{A_Z} q'''dA_z \tag{3.85}$$

$$\Rightarrow \frac{\partial}{\partial t}[(\rho_m h_m - p)A_z] + \frac{\partial}{\partial z}(G_m h_m^+ A_z) = q' + \iint_{A_Z} q'''dA_z \tag{3.86}$$

$$h_m = \frac{1}{\rho_m}\{\rho_v \alpha h_v + \rho_l(1-\alpha)h_l\} \tag{3.87}$$

where h_m = static mixture enthalpy averaged over area A_z (J/kg). Also:

$$h_m^+ = \frac{1}{G_m}\{\rho_v \alpha h_v v_{vz} + \rho_l(1-\alpha)h_l v_{lz}\} \tag{3.88}$$

where h_m^+ = dynamic (or mixing cup) average enthalpy over area A_z (J/kg).

If total volume is assumed to be as follows:

$$\not{V} = A_z \Delta z \tag{3.89}$$

where $\not{V}$ = volume (m^3) and Δz = distance between discretized node locations (m), then a one-dimensional spatially averaged energy equation can be derived. A heat addition term is now defined to represent the heat added internally to fluid k and from surface heat addition as follows:

$$\left(\frac{dQ}{dt}\right)_k = \iiint_{\not{V}_k} q_k''' d\not{V} + \oiint_{S_k} \overrightarrow{q_k''} \cdot \vec{n}\, ds \tag{3.90}$$

where $\overrightarrow{q_k''} \cdot \vec{n}$ = heat flux normal to the surface (W/m^2) and $\vec{n}$ = unit vector normal to flow cross-sectional area.

Also introducing a work term due to shear forces:

$$\left(\frac{dW}{dt}\right)_{k,shear} = -\oiint_{S_k} \overrightarrow{\overline{\tau_k}} \cdot \vec{n}\, ds \iiint_{\mathrm{v}_k} q_k''' d\mathrm{v} + \oiint_{S_k} \overrightarrow{q_k''} \cdot \vec{n}\, ds \tag{3.91}$$

where $\bar{\bar{\tau}}$ = stress tensor (Pa). The stress tensor is defined as:

$$\bar{\bar{\tau}} = \begin{pmatrix} \tau_{xx} & \tau_{xy} & \tau_{xz} \\ \tau_{yx} & \tau_{yy} & \tau_{yz} \\ \tau_{zx} & \tau_{zy} & \tau_{zz} \end{pmatrix} \tag{3.92}$$

where each component's subscripts indicate the stress on each side of a theoretical cube.

For equilibrium conditions:

$$\tau_{ij} = \tau_{ji} \tag{3.93}$$

for τ stress (Pa) and i and j being any of the three Cartesian axes. Todreas and Kazimi's text (1990) shows that the energy transport equation can be developed as:

$$\frac{\partial}{\partial t}[(\rho_m h_m - p)A_z] + \frac{\partial}{\partial z}(G_m h_m^+ A_z) = q_m''' A_z - q'' P_h + \frac{G_m}{\rho_m}\left(F_{wz}''' + \frac{\partial p}{\partial z}\right) A_z \tag{3.94}$$

where P_h= heated perimeter of fuel rod (m) and F_{wz}''' = net force per unit volume due to shear forces at the walls (N/m^3).

The latter introduced variable may be defined as:

$$F_{wz}''' = \frac{1}{A_z}\int \tau_w dP_z = \left(\frac{\partial p}{\partial z}\right)_{fric} \tag{3.95}$$

from the momentum equation development.

For constant vertical area A_z for the single coolant channel and assuming the phasic pressures are roughly equal, as done with the momentum equation (i.e. $p_v \simeq p_l \simeq p$):

$$\frac{\partial}{\partial t}(\rho_m h_m - p) + \frac{\partial}{\partial z}(G_m h_m^+) = \frac{q'' P_h}{A_z} + \frac{G_m}{\rho_m}\left(\frac{\partial p}{\partial z} + \frac{f G_m^2}{2 D_e \rho_m}\right) \tag{3.96}$$

The friction factor, f, may represent either single-phase or two-phase conditions.

The absolute value notation is used on the term containing mass flux, G_m, to take into account the friction force change depending on the flow direction. Rearrangement of the equation above provides:

$$\frac{\partial}{\partial t}(\rho_m h_m) + \frac{\partial}{\partial z}(G_m h_m^+) = \frac{q'' P_h}{A_z} + \frac{\partial p}{\partial t} + \frac{G_m}{\rho_m}\left(\frac{\partial p}{\partial z} + \frac{f G_m^2}{2 D_e \rho_m}\right) \tag{3.97}$$

Evaluating at steady-state:

$$\frac{\partial}{\partial z}(G_m h_m^+) = \frac{q'' P_h}{A_z} + \frac{G_m}{\rho_m}\left(\frac{\partial p}{\partial z} + \frac{f G_m^2}{2 D_e \rho_m}\right) \tag{3.98}$$

3.4 Implementation of Fluid Models with Conservation Equations

Having developed the differential equations relating the momentum and energy conservation principles to the fluid flow, the equations are adapted to the HEM and drift flux models in the following sections, depending on each model's assumptions and implementation.

3.4.1 HEM Model

3.4.1.1 Momentum

Beginning with the following equation:

$$\frac{\partial}{\partial z}\{\rho_v \alpha\, v_{vz}^2 + \rho_l (1-\alpha) v_{lz}^2\}$$

$$= -\frac{\partial p}{\partial z} - \phi_{fric}^2 \frac{f G_m^2}{2 D_h \rho_m} - \frac{\partial}{\partial z}\left[\phi_{lo}^2 K \frac{G_m^2}{2\rho_l}\right] - \rho_m g cos\theta \tag{3.99}$$

Reintroducing the mixing up enthalpy to the equation:

$$\frac{\partial}{\partial z}\left(\frac{G_m^2}{\rho_m^+}\right) = -\frac{\partial p}{\partial z} - \phi_{fric}^2 \frac{f G_m^2}{2 D_e \rho_l} - \frac{\partial}{\partial z}\left[\phi_{local}^2 \sum K \frac{G_m^2}{2\rho_l}\right] - \rho_m g cos\theta \tag{3.100}$$

In the HEM model, the phasic velocities are assumed to be equal:

$$v_m = v_l = v_v \tag{3.101}$$

The following equations also apply to the HEM model:

$$h_m = h_m^+ \tag{3.102}$$

$$\rho_m = \rho_m^+ \tag{3.103}$$

Applying these to the momentum equation gives us:

$$\frac{\partial}{\partial z}\left(\frac{G_m^2}{\rho_m}\right) = -\frac{\partial p}{\partial z} - \phi_{fric}^2 \frac{f G_m^2}{2 D_e \rho_l} - \frac{\partial}{\partial z}\left[\phi_{lo}^2 \sum K \frac{G_m^2}{2\rho_l}\right] - \rho_m g cos\theta \tag{3.104}$$

3.4.1.2 Energy/Enthalpy

The friction and pressure terms in the energy/enthalpy equations tend to be negligible as compared to the other terms in the momentum equation; Todreas and Kazimi (1990) removed them for HEM analysis. The mixing enthalpy may also be set to the mixture enthalpy as done with the HEM momentum equation in Eq. (3.104). Applying these assumptions to Eq. (3.98) along with Eq. (3.102) results in the following reduced HEM enthalpy equation:

$$\frac{\partial}{\partial z}(G_m h_m) = \frac{q'' P_h}{A_z} \tag{3.105}$$

Applying the continuity equation with constant mass flux independent of channel location:

$$G_m \frac{\partial h_m}{\partial z} = \frac{q'' P_h}{A_z} \tag{3.106}$$

3.4.2 Drift Flux Model

Combining the drift flux parameters from earlier in this section to the conservation equations allows for the creation of the drift flux conservation equations. As implemented in NESTLE by Galloway (2010), the equations used in that code are as follows:

- Mass Continuity:

$$A_z \frac{\partial \rho_m}{\partial t} + \frac{\partial}{\partial z}(G_m A_z) = 0 \tag{3.107}$$

- Momentum:

$$A_z \frac{\partial}{\partial t}(\rho_m v) + \frac{1}{A_z}\frac{\partial}{\partial z}\left(\frac{G_m^2 A_z}{\rho_m}\right)$$

$$= -\frac{\partial p}{\partial z} - \frac{\tau_w P_w}{A_z} - \frac{1}{A_z}\frac{\partial}{\partial z}\left(\frac{\rho_l \rho_v}{\rho}\left(\frac{1}{\alpha(1-\alpha)}\right) j_D^2 A_z\right) - \rho_m g cos\theta \tag{3.108}$$

where

$$\frac{\tau_w P_w}{A_z} = f\left(\frac{G^2}{2D_e \rho_l}\right)\phi_{fric}^2 + \sum_m \delta(z - z_m) K\left(\frac{G^2}{2\rho_l}\right)\phi_{local}^2 \tag{3.109}$$

- Internal Energy:

$$A_z \frac{\partial}{\partial t}(\rho u) + \frac{\partial}{\partial z}(G_m u A_z)$$

$$= -p\frac{\partial}{\partial z}\left(\frac{G}{\rho}A_z\right)A_Z + q'''A_z - p\frac{\partial}{\partial z}\left(\frac{\rho_l - \rho_v}{\rho} j_D A_z\right) - \frac{\partial}{\partial z}\left(\frac{\rho_l \rho_v}{\rho}(u_v - u_l) j_D A_z\right) \tag{3.110}$$

where

$$j_D = \overline{V_{vJ}}\{\alpha\} \tag{3.111}$$

Note also that, according to Todreas and Kazimi (1990), enthalpy may be used

interchangeably with the internal energy equation (requiring several modifications to terms accordingly). The conservation equations have been implemented in the TH code for the drift flux model in steady state as follows:

- Mass Continuity:

$$\frac{\partial}{\partial z}(G_m A_z) = 0 \tag{3.112}$$

- Momentum:

$$\frac{1}{A_z}\frac{\partial}{\partial z}\left(\frac{G_m^2 A_z}{\rho_m}\right)$$

$$= -\frac{\partial p}{\partial z} - \frac{\tau_w P_w}{A_z} - \frac{1}{A_z}\frac{\partial}{\partial z}\left(\frac{\rho_l \rho_v}{\rho}\left(\frac{1}{\alpha(1-\alpha)}\right) j_D^2 A_z\right) - \rho_m g cos\theta \tag{3.113}$$

where

$$\frac{\tau_w P_w}{A_z} = f\left(\frac{G^2}{2D_e\rho_l}\right)\phi_{fric}^2 + \frac{\partial}{\partial z}\left(K\left(\frac{G^2}{2\rho_l}\right)\phi_{local}^2\right) \tag{3.114}$$

- Energy/Enthalpy:

$$\frac{\partial}{\partial z}(G_m h A_z)$$

$$= -p\frac{\partial}{\partial z}\left(\frac{G}{p}A_z\right)A_Z + q'' P_h - p\frac{\partial}{\partial z}\left(\frac{\rho_l - \rho_v}{\rho} j_D A_z\right) - \frac{\partial}{\partial z}\left(\frac{\rho_l \rho_v}{\rho} h_{lv} j_D A_z\right) \tag{3.115}$$

where

$$j_D = \overline{V_{vj}}\{\alpha\} \tag{3.116}$$

3.5 Finite Difference Scheme

The equations developed must now by discretized into finite difference equations to be used in a one-dimensional line separated by nodes. The mixture momentum equation is first addressed, solving for the pressure at the upper nodal edge. Secondly, the energy conservation equation is solved for the specific enthalpy at the upper nodal edge.

Figure 3.2 demonstrates the parameters evaluated at node k and their relationship to those at the nodal edges. The density $\bar{\rho}_k$, internal energy $\bar{u}_k$, and pressure $\overline{p_k}$ are averaged values between those calculated at the upper nodal edge $k + {}^1/_2$ and lower nodal edge $k - {}^1/_2$, where the areas $A_{x_{(k+{}^1/_2)}}$ and $A_{x_{(k-{}^1/_2)}}$ are determined, respectively. The one-dimensional discretized conservation equations are first solved for each individual LWR subchannel at the inlet and subsequently solved upwards along the

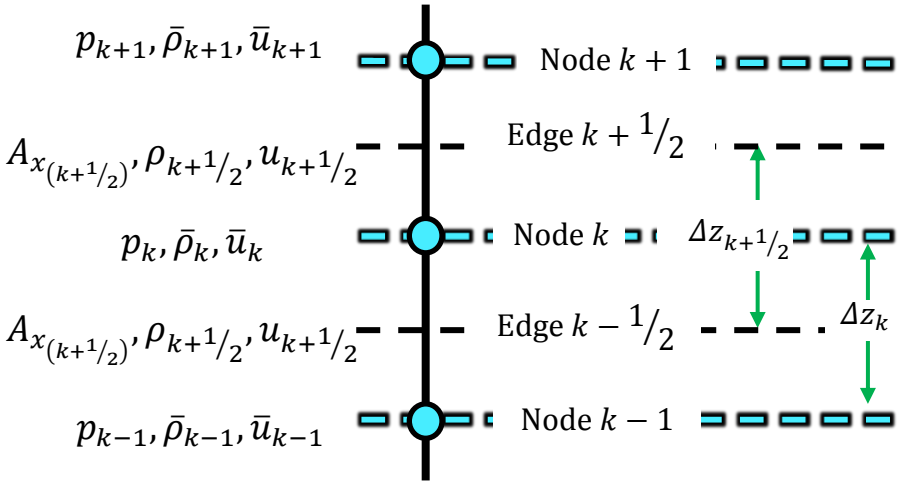

Figure 3.2. Nodal discretization of TH finite difference equations.

channel until the top.

For cases where a LWR system has multiple coolant subchannels, the top-left subchannel is analyzed first followed by the subchannel adjacent to its right on that row, continuing until reaching the end of the row. The left-most subchannel on the row just below is then analyzed and the process continues until all subchannels are analyzed.

Each coolant subchannel is numbered, with each subchannel being analyzed separately, beginning with subchannel 1 and ending with subchannel $(n+1)^2$, where n is the number of fuel pins in the horizontal and vertical directions for a square assembly (e.g., a square assembly where $n = 4$ will have 16 fuel pins and 25 total subchannels). Note that the inclusion of additional pins, other elements (such as a central water rod, poison rods, etc.), a nonsquare assembly (e.g., a 3x4 pin arrangement) or any other significant deviations will modify the numbering scheme along with the subchannel properties (subchannel cross-sectional flow area, heated perimeters, hydraulic diameters, heat flux values, etc.) and must be adjusted by the user in the TH code on an individual case-by-case basis. Figure 3.3 shows the enumeration of coolant subchannels for a standard 3x3 LWR assembly.

The initial parameters at the channel inlet are supplied by the user, such as pressure, mass flow rate, extent of subcooling, etc. The energy/enthalpy equation is solved first at each nodal edge along the channel, followed by the momentum equation. The code continues to run in each iteration with updated energy and pressure values until a proper convergence is reached. The HEM and drift flux model finite difference equations are related in the following subsections separately.

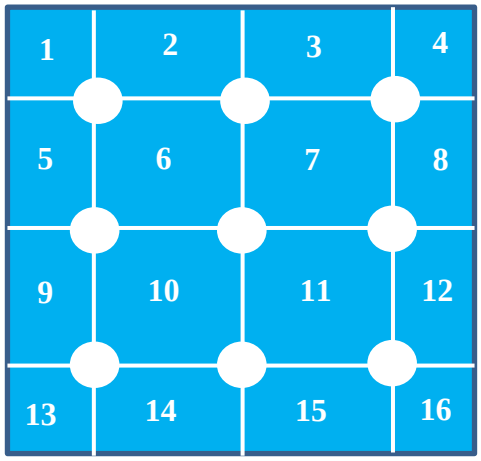

Figure 3.3. Enumeration system for each coolant subchannel for a standard 3x3 LWR assembly in the TH thermal hydraulics code. The conservation equations described in Chapter 3 are solved for each coolant subchannel separately beginning with subchannel 1 and ending with subchannel $(n+1)^2$ where n is the number of fuel pins in the horizontal and vertical directions in a square (i.e. nxn) assembly. Note that any addition or removal of pins or subchannels will require the user to manually update the code to take the changes into account.

3.5.1 HEM Model

The HEM model finite difference equations are as follows:

- Momentum/Mass Continuity:

$$p_{k+1/2} = p_{k-1/2} - G_m^2\left(\frac{1}{\rho_{k+1/2}} - \frac{1}{\rho_{k-1/2}}\right)$$

$$-\left(\phi_{lo}^2 \frac{f G_m^2 \Delta z}{2 D_e \rho_l}\right)_k - \left(\phi_{lo}^2 \sum K \frac{G_m^2}{2\rho_l}\right)_k - (\rho_m g \Delta z)_k \qquad (3.117)$$

- Energy/Enthalpy:

$$h_{m,k+1/2} = h_{m,k-1/2} + \left(\frac{q'' P_h \Delta z}{G_m A_z}\right)_k \qquad (3.118)$$

3.5.2 Drift Flux Model

Similarly, the discretized equations for the drift flux model are as follows:

- Momentum/Mass Continuity:

$$p_{k+1/2} = p_{k-1/2} - G_m^2\left(\frac{1}{\rho_{k+1/2}} - \frac{1}{\rho_{k-1/2}}\right) - \left(\phi_{fric}^2 \frac{fG^2\Delta z}{2D_e\rho_l}\right)_k - \left(\phi_{local}^2 \frac{KG^2}{2\rho_l}\right)_k - (\rho g \Delta z)_k - \left[\left(\frac{\rho_l\rho_v}{\rho}\left(\frac{\{\alpha\}}{(1-\{\alpha\})}\right)V_{vj}^2\right)_{k+1/2} - \left(\frac{\rho_l\rho_v}{\rho}\left(\frac{\{\alpha\}}{(1-\{\alpha\})}\right)V_{vj}^2\right)_{k-1/2}\right] \quad (3.119)$$

- Energy/Enthalpy:

$$h_{k+1/2} = h_{k-1/2} - p_k\left(\frac{1}{\rho_{k+1/2}} - \frac{1}{\rho_{k-1/2}}\right) + \left(\frac{q'' P_h \Delta z}{G_m A_z}\right)_k - \frac{p_k}{G_m}\left(\left(\frac{\rho_l - \rho_v}{\rho} j_D\right)_{k+1/2} - \left(\frac{\rho_l - \rho_v}{\rho} j_D\right)_{k-1/2}\right) - \frac{1}{G_m}\left(\left(\frac{\rho_l\rho_v}{\rho} h_{lv} j_D\right)_{k+1/2} - \left(\frac{\rho_l\rho_v}{\rho} h_{lv} j_D\right)_{k-1/2}\right) \quad (3.120)$$

3.6 Net Vapor Generation (NVG) Model

The HEM and drift flux models have different models by which the void fraction is calculated. The accurate calculation of void fraction is essential to take into account heat transfer effects based on the type of two-phase flow, as well as for single-phase flow (for

subcooled liquids where void fraction is negligible). Boiling will also occur at the walls of the heated pins as they are not completely smooth. Nucleation sites exist at the heated pins where bubbles may form locally. To take subcooled nucleate boiling, a Net Vapor Generation (NVG) model is used.

The NVG model takes into account boiling in a heated channel when the bulk liquid is below saturated temperature conditions. Figure 3.4 displays two curves depicting boiling behavior according to two different models, including the NVG model curve (solid line) and the saturated boiling curve (dashed line). The latter operates under the assumption that boiling occurs only after the fluid's bulk temperature is elevated at or above the fluid thermodynamic saturation temperature at the prescribed fluid pressure.

The horizontal axis indicates several axial heights (Z with varying subscripts) representing transition points at which changes in subcooled boiling occur. The transition height location parameters and the associated type of subcooled boiling region

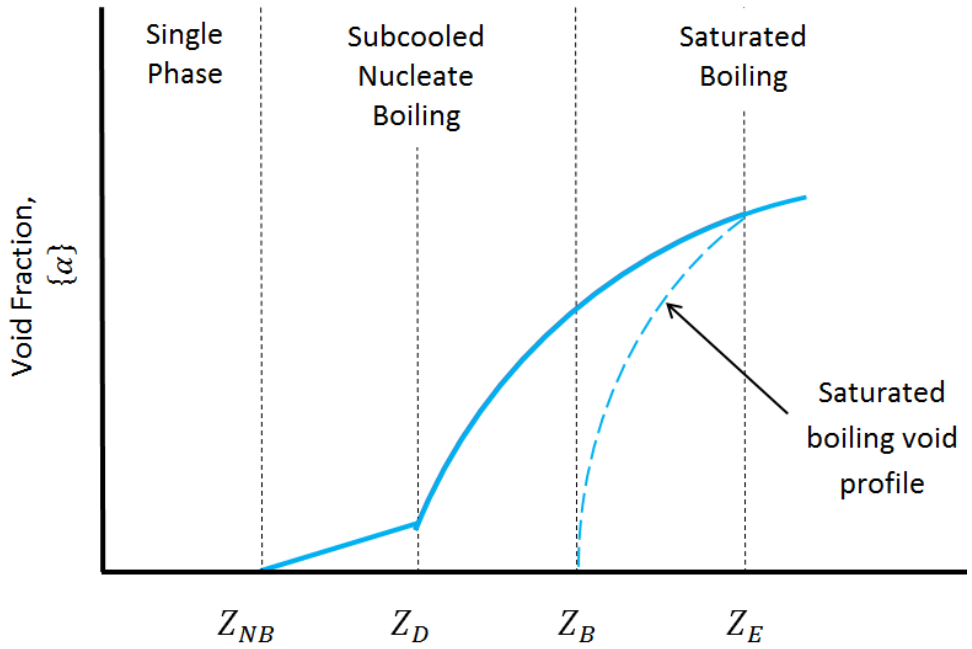

Figure 3.4. Net Vapor Generation (NVG) model as compared with saturated boiling profile for area-averaged void fraction versus axial height in a heated channel.

are listed respectively for each region as follows: Z_{NB} for nucleate boiling, Z_D for bubble detachment, Z_B for bulk liquid boiling, and Z_E where thermal equilibrium conditions between the liquid and vapor phases exist.

Each region indicates the general behavior of the intermixed vapor phase within the fluid flow. In the nucleate boiling region (between axial channel heights Z_{NB} and Z_D), the void fraction is small and is considered negligible. In the detached bubble region (between axial channel heights Z_D and Z_B), bubbles are much more prevalent in the fluid flow. This is the point at which bubbles receive sufficient energy to detach from the surface while preventing from undergoing condensation, returning to a liquid state within the flow. Many of these bubbles collapse as heat is transferred from the bubbles to the liquid. In the bulk boiling region (between axial channel heights Z_B and Z_E), the liquid and vapor phases in the fluid are in thermal equilibrium. In this condition, the bubbles will not collapse as in the detached bubble region. This is where the thermodynamic bulk boiling occurs. As heat is continually added to the saturated fluid, the liquid vaporizes, depending on its value for heat of vaporization or the energy required to break the loosely bound structure of the liquid in order to convert it into a gaseous state. Above the equilibrium height Z_E, the subcooling model is no longer applicable. Theoretically, at this height, the entire fluid should be in thermal equilibrium. When the fluid receives sufficient energy to vaporize all the liquid within the flow, superheated vapor tables are then required to determine the thermodynamic properties of the fluid.

There are two NVG models implemented in the NESTLE code (Galloway, 2010) the Saha-Zuber relation and the more recent EPRI model developed by Lellouche and Zolotar. The default model implemented in the TH code is the EPRI model. The

equations for both models are listed and may be chosen by the user.

The Saha-Zuber model takes both hydrodynamic and thermal conditions into account when determining the NVG quality, x_{NVG}. It is calculated depending on the Peclet number, Pe. This number is calculated as follows for rectangular, annular, as well as circular tubes:

$$Pe = \frac{GD_e c_{pl}}{k_l} \tag{3.121}$$

where c_{pl} = specific heat capacity of liquid phase (J/kg-K or J/kg-°C) and $k_{TH,l}$ = thermal conductivity of liquid phase (W/m-K or W/m-°C).

The Peclet number is also a ratio of the Nusselt and Stanton numbers, Nu and St, respectively:

$$Pe = \frac{Nu}{St} \tag{3.122}$$

In the Saha-Zuber model, if the Peclet number is less than 70,000:

$$x_{NVG} = -\frac{0.0022 q'' D_e c_p}{k(h_v - h_l)} \tag{3.123}$$

If the Peclet number is greater than or equal to 70,000:

$$x_{NVG} = -\frac{154q''}{G(h_v - h_l)} \tag{3.124}$$

The EPRI model uses the following equation for NVG quality:

$$x_{NVG} = \frac{c_p Z}{h_v - h_l}\left(\frac{2.3886(10^{-4})\frac{\text{BTU}}{\text{lbm} - °\text{F}}}{1\frac{\text{J}}{\text{kg} - \text{K}}}\right)\left(\frac{2326\ \frac{\text{J}}{\text{kg}}}{1\frac{\text{BTU}}{\text{lbm}}}\right) \tag{3.125}$$

where Z is the positive square root solution to a quadratic equation following the formula:

$$Z = \frac{-b + \sqrt{b^2 - 4ac}}{2a} \tag{3.126}$$

The variables a, b, and c are determined as follows:

$$a = 4HB(HDB + HHN)^2 \tag{3.127}$$

$$b = 2HDB^2\left(HHN + {}^{HDB}/_{2}\right) + 8q''\left(\frac{1\ \frac{\text{BTU}}{\text{hr} - \text{ft}^2}}{3.154590745\frac{\text{W}}{\text{m}^2}}\right)HB(HDB + HHN) \tag{3.128}$$

$$c = q''\left(\frac{1\ \frac{\text{BTU}}{\text{hr} - \text{ft}^2}}{3.154590745\frac{\text{W}}{\text{m}^2}}\right)\left[4q''\left(\frac{1\ \frac{\text{BTU}}{\text{hr} - \text{ft}^2}}{3.154590745\frac{\text{W}}{\text{m}^2}}\right)HB + HDB^2\right] \tag{3.129}$$

where

$$HB = \frac{\exp\left[{}^{P}/_{630}\left(\frac{1\text{ psia}}{6894.75728\text{ Pa}}\right)\right]}{0.072^2} \tag{3.130}$$

$$HDB = CDB\frac{Re^{0.8}Pr^{0.4}k_{TH}}{D_e}\left(\frac{0.57782\frac{\text{BTU}}{\text{hr}-\text{ft}-°\text{F}}}{1\frac{\text{W}}{\text{m}-\text{K}}}\right)\left(\frac{0.3048\text{ m}}{1\text{ ft}}\right) \tag{3.131}$$

$$CDB = 0.033\varepsilon_{frac} + 0.013 \tag{3.132}$$

with

$$\varepsilon_{frac} = \frac{A_z}{A_z + A_{rods}} \tag{3.133}$$

where A_{rods} = cross-sectional area of fuel rods (m^2) and Pr = Prandtl Number. Continuing the set of equations:

$$HHN = CHN\left[Re^{0.662}Pr\frac{k}{D_e}\left(\frac{0.57782\frac{\text{BTU}}{\text{hr}-\text{ft}-°\text{F}}}{1\frac{\text{W}}{\text{m}-\text{K}}}\right)\left(\frac{0.3048\text{ m}}{1\text{ ft}}\right)\right] \tag{3.134}$$

and:

$$CHN = \frac{0.2D_h}{4R_{rod}} \tag{3.135}$$

where R_{rod} = fuel rod radius (m).

The area of the fuel rods is calculated assuming they are cylindrical:

$$A_{rods} = N_{rod}\pi R_{rod}^2 \tag{3.136}$$

where N_{rod} = total number of fuel rods.

Of note is that several of these equations include correction factors. These equations were developed using United States customary units, and thus, some values required conversion from SI to US customary units before the EPRI model parameters could be calculated. The EPRI model is implemented in the TH code as coupled with AGENT.

Once the NVG quality is calculated, the true quality must be determined. The true quality is calculated using a hyperbolic tangential fit as introduced by Lahey and Moody (1977):

$$x = \frac{x_{eq} - x_{NVG}\left(1 - \tanh\left(1 - {}^{x_{eq}}/_{x_{NVG}}\right)\right)}{1 - x_{NVG}\left(1 - \tanh\left(1 - {}^{x_{eq}}/_{x_{NVG}}\right)\right)} \tag{3.137}$$

The true quality is necessary to determine the void fraction, which is discussed in the following section. The HEM and drift flux void fraction models are considered separately when calculating void fraction.

3.7 Void Fraction Model

3.7.1 HEM Model

The void fraction calculation for the HEM model is straightforward. Due to the phasic velocities being equal, for the HEM model only:

$$S = 1 \tag{3.138}$$

Since the previous equation applies, the void fraction using the HEM model is found as follows:

$$\{\alpha\} = \frac{1}{1 + \frac{1-x}{x}\frac{\rho_v}{\rho_l}} \tag{3.139}$$

3.7.2 Drift Flux Model

Several models exist to calculate the void fraction in a heated channel for the drift flux model while accounting for two-phase flow. Among these include the models developed by Chexal and Lellouche (1986), Zuber and Findlay (1965), and Lellouche and Zolotar (1982). The last model is employed in the TH code. Along with the models, the steam tables provided by the NIST website (2011) allow for accurate calculation of fluid properties.

As with the NVG model used in the TH code, several parameters are determined previous to calculating the final void fraction. However, some of these equations require a prior value for the void fraction. A value of void fraction must first be assumed in order to begin the calculations. Thus, it is an iterative process to calculate the void fraction, which continues until a set convergence criterion is reached. The equations are listed below.

$$C_1 = 4\frac{P_c^2}{P(P_c - P)} \tag{3.140}$$

where, as before, P_c is the coolant flow critical pressure. For water, the critical pressure is approximately $22.06(10^6)$ Pa.

If the void fraction is zero:

$$L_n = 1.0 \tag{3.141}$$

Otherwise:

$$L_n = 1 - \exp[-(C1 \cdot \alpha)] \tag{3.142}$$

$$K_1 = \min\left(0.8 \frac{1}{1 + \exp\left[-\left(\text{Re}/_{1E5}\right)\right]}\right) \tag{3.143}$$

$$K_0 = K_1 + (1 - K_1)\left(\frac{\rho_v}{\rho_l}\right)^{1/4} \tag{3.144}$$

$$r = \frac{1 + 1.57\left(\frac{\rho_v}{\rho_l}\right)}{1 - K_1} \tag{3.145}$$

$$A = K_0 + (1 - K_0)\alpha^r \tag{3.146}$$

The mean drift velocity is found to be:

$$\overline{V_{vJ}} = \left(\frac{1.41(\rho_l - \rho_v)\sigma g^2}{\rho_l^2}\right)^{1/4} (1 - \alpha)^{3/2} \tag{3.147}$$

where σ = surface tension of liquid (N/m).

$$C_0 = {L_n}/{A} \tag{3.148}$$

$$Y = (1 - x)\left(\frac{\rho_v}{\rho_l}\right)\left(1 + \frac{\rho_l A \overline{V_{vj}}}{G_m L_n (1 - x)}\right) \tag{3.149}$$

If $L_n \geq 0.2$:

$$\alpha = \frac{A}{(1 + {Y}/{x})L_n} \tag{3.150}$$

Otherwise, if $L_n < 0.2$:

$$\alpha = \sqrt{\frac{A}{(1 + {Y}/{x})C_1}} \tag{3.151}$$

and the true coolant quality found using the NVG model is represented as x.

As a point of comparison, a second set of equations for determining the concentration parameter and mean drift velocity are derived from Hibiki & Ishii (2003, 2005). This set of equations are derived for each boiling regime as shown in Figure 3.5. This figure was adapted from a simplification of the boiling regime map from Todreas and Kazimi (1990) taken from the work of Hewitt and Roberts (1969). Each equation for this model refers to the bubbly flow, slug flow, churn flow, and annular flow boiling regimes. The horizontal axis on Figure 3.5 is labeled using the multiplication of the liquid density multiplied by the square of the superficial liquid velocity. The vertical axis is similarly labeled using the same measurements, but for the fluid vapor phase.

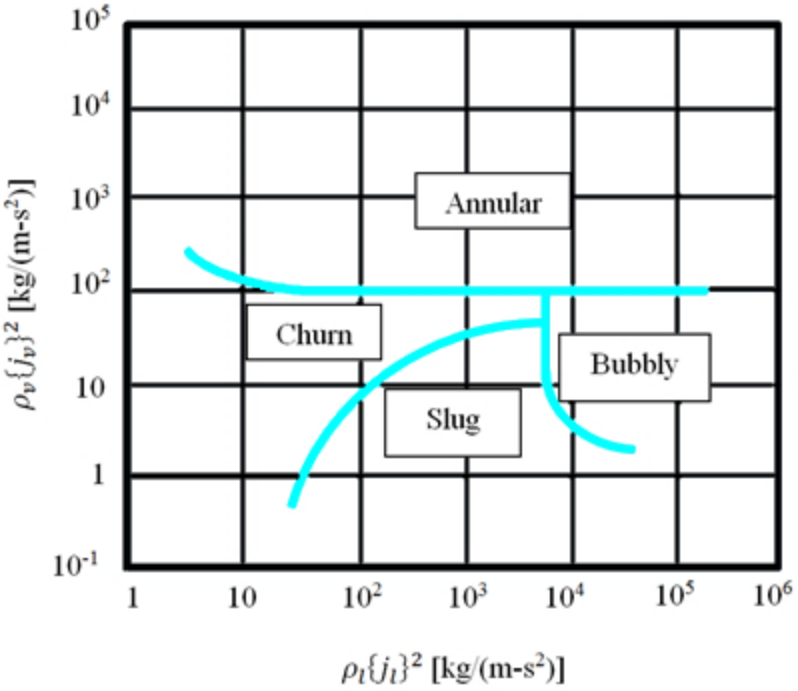

Figure 3.5. Boiling flow regime map adapted from Todreas & Kazimi (1990).

The equations for each boiling flow regime from the Hibiki-Ishii void fraction model are as follows:

- Bubbly flow:

$$C_0 = 2.0\exp(-0.000584 \cdot Re) + 1.2\{1 - \exp(-22\{D_{sm}\}/D_h)\}$$
$$\cdot\{1 - \exp(-0.000584\ Re)\} - [2.0\exp(-0.000584\ Re)$$
$$+1.2\{1 - \exp(-22\{D_{sm}\}/D_h)\} \cdot \{1 - \exp(-0.000584\ Re)\} - 1]\sqrt{\rho_v/\rho_l} \quad (3.152)$$

$$V_{vj} = \sqrt{2}\left(\frac{\Delta\rho g\sigma}{\rho_l^2}\right)^{1/4}(1 - \{\alpha\})^{1.75} \quad (3.153)$$

- Slug flow:

$$C_0 = 1.2 - 0.2\sqrt{\rho_v/\rho_l} \tag{3.154}$$

$$V_{vj} = 0.35\sqrt{\frac{\Delta\rho g D_h}{\rho_l}} \tag{3.155}$$

- Churn flow:

$$C_0 = 1.2 - 0.2\sqrt{\rho_v/\rho_l} \tag{3.156}$$

$$V_{vj} = \sqrt{2}\left(\frac{\Delta\rho g\sigma}{\rho_l^2}\right)^{1/4} \tag{3.157}$$

For annular flow, instead of having separate equations for the two parameters, the mean drift velocity is directly calculated:

$$\overline{V_{vJ}} = (1-\{\alpha\})\left(\{\alpha\} + \left\{\frac{1+75(1-\{\alpha\})}{\sqrt{\{\alpha\}}}\,\frac{\rho_v}{\rho_l}\right\}^{1/2}\right)^{-1} \cdot\left(\{j\} + \sqrt{\frac{\Delta\rho g D(1-\{\alpha\})}{0.015\rho_l}}\right) \tag{3.158}$$

The parameter D_{sm}, as calculated in Eq. (3.152), represents the bubble Sauter mean diameter (m), which may be predicted using the following relations:

$$D_{sm} = Lo\widetilde{D_{sm}} = Lo\left(1.99\,\widetilde{Lo}^{-0.335}\widetilde{Re}^{-0.239}\right) \tag{3.159}$$

$$Lo \equiv \sqrt{\sigma / g \Delta \rho} \tag{3.160}$$

$$\widetilde{Lo} \equiv Lo / D_h \tag{3.161}$$

$$\widetilde{Re} \equiv \left(\{\varepsilon\}^{1/3} Lo^{1/3}\right) Lo / \nu_l \tag{3.162}$$

where ε = energy dissipation rate per unit mass with:

$$\{\varepsilon\} = g\{j_v\} \exp(-0.000584 \cdot Re)$$

$$+ \frac{\{j\}}{\rho_m} \left(-\frac{dp}{dz}\right)_{fric} \cdot \{1 - \exp(-0.000584 \cdot Re)\} \tag{3.163}$$

$$\nu = \mu / \rho \tag{3.164}$$

The two-phase friction pressure gradient may be approximated using the Method of Lockhart-Martinelli (Todreas & Kazimi, 1990):

$$\left(\frac{dp}{dz}\right)_{fric} = \phi_l^2 \left(\frac{dp}{dz}\right)_{fric}^{l} \tag{3.165}$$

and:

$$\phi_l^2 = (1 - \{\alpha\})^{-2} \tag{3.166}$$

$$\left(\frac{dp}{dz}\right)_{fric}^{l} = \frac{f_l}{D_h} \left[\frac{G_m^2 (1 - x)^2}{2\rho_l}\right] \tag{3.167}$$

where

$$f_l \sim \left(\frac{\mu_l}{D_h G_l}\right)^n = \left(\frac{\mu_l}{D_h G_m (1-x)}\right)^n \tag{3.168}$$

where n may be 0.2 or 0.25, depending on the type of correlation used (Todreas & Kazimi, 1990).

For bubbly, churn, and slug flow, the mean effective drift velocities may be calculated thus:

$$\overline{V_{vj}} = V_{vj} + (C_0 + 1)\{j\} \tag{3.169}$$

With the calculated values for V_{vj}, C_0 as determined in the Hibiki-Ishii void fraction model (depending on the coolant boiling regime), the void fraction may be calculated directly using Eq. (3.50).

3.8 Fuel Pin Heat Transfer Model

The hydrodynamic models used by the TH code require coupling with a heat transfer model to determine the average fuel temperatures. These temperatures allow a coupling with the AGENT neutronics code by updating the materials cross sections as a function of temperature in the Scale computation code. Figure 3.6 provides an overview of the coupling scheme between the 1D axial fluids equations (including the HEM and drift flux models as well as the NVG and void fraction models) and the 1D radial heat transfer model. The radial heat transfer model is evaluated at the same axial locations along each pin as where the fluids models were evaluated. The average fuel pin temperatures are then found using the model described in this section. Similar to the enumeration system

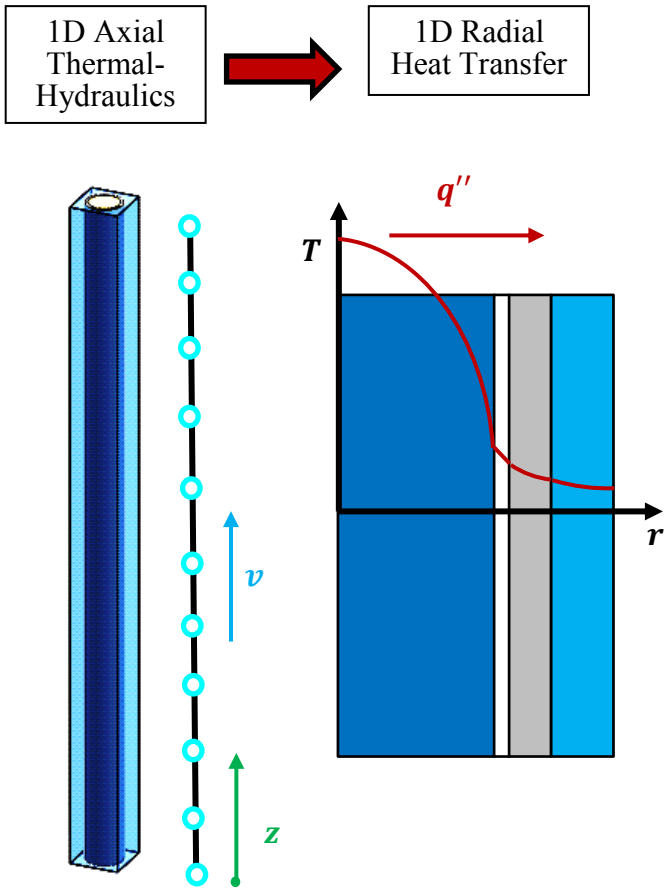

Figure 3.6. Coupling scheme between 1D axial thermal-hydraulic model and 1D radial heat transfer model.

as visually described in Figure 3.3 for the coolant subchannels, the equations in this section for the fuel pins are first solved for the top-left fuel pin (numbered pin 1) and continue until pin n^2, where n is the vertical and horizontal number of pins in a square array. Figure 3.7 shows the system of numbering fuel pins for a standard 3x3 square LWR assembly.

As nuclear fissions occur by the collision of neutrons to uranium-235 (U-235), the primary fissile nuclide within the fuel element of a light water reactor (LWR), heat is generated at position vector $\vec{r}$ from isotope j by the following equation (Todreas &

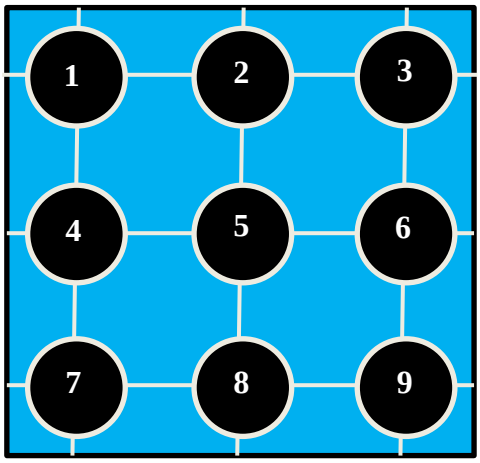

Figure 3.7. Enumeration system for each fuel pin for a standard 3x3 LWR assembly in the TH thermal hydraulics code. The radial 1D heat transfer equations described in Chapter 3 are solved for each fuel pin separately, beginning with pin 1 and ending with pin n^2, where n is the number of fuel pins in the horizontal and vertical directions in a square (i.e., nxn) assembly. Note that any addition or removal of pins or subchannels will require the user to manually update the code to take the changes into account.

Kazimi, 1990):

$$q_j'''(\vec{r}) = \int_0^\infty \chi_f^j R_f^j(\vec{r}, E) dE \tag{3.170}$$

where $q_j'''(\vec{r})$ = volumetric heat generation from isotope j (W/m^3), χ_f^j = energy deposited in fuel per fission reaction of isotope j (J), and R_f^j = fission reaction rate of isotope j ((m^3-s)$^{-1}$).

The fission reaction rate of isotope j may be expressed as:

$$R_f^j(\vec{r}, E) = \Sigma_f^j(\vec{r}, E)\phi(\vec{r}, E) \tag{3.171}$$

where Σ_f^j = macroscopic fission cross section of isotope j (m^{-1}) and ϕ = neutron flux

($(m^2\text{-}s)^{-1}$).

Inserting into the equation for volumetric heat generation above:

$$q_j'''(\vec{r}) = \int_0^\infty \chi_f^j \Sigma_f^j(\vec{r},E)\phi(\vec{r},E)dE \tag{3.172}$$

Normally, in order to reduce computation times, neutron energies are divided into one or more energy groups or intervals; the following equation proves useful for calculating heat produced from each isotope j and neutron energy group g':

$$q_j'''(\vec{r}) = \sum_j \sum_{g'=1}^{G} \chi_f^j \Sigma_{fg'}^j(\vec{r})\phi_{g'}(\vec{r}) \tag{3.173}$$

where G = total number of neutron energy groups, $\Sigma_{fg'}^j$ = macroscopic fission cross section for energy group g' (m^{-1}), and $\phi_{g'}$ = neutron flux of energy group g' ($(m^2\text{-}s)^{-1}$).

While the majority of released energy per fission is imparted to the kinetic energy of fission fragments, the remaining approximately 19.5% of the energy released per fission is released elsewhere. Table 3.1 shows the distribution of energy released in which particles and by what form the energy is released, whether through kinetic energy of massive particles, electromagnetic energy, etc.

The approximate average energy released per fission is 200 MeV. However, as described in Table 3.3, approximately 5% of this energy is unrecoverable (i.e., lost) due to the release of neutrinos. Thus, it is assumed that, for a thermal reactor, the total

Table 3.3. Approximated average distribution of energy released per fission in thermal reactors.

Type of Energy Release	**Process**	**Percent of Total Released Energy**	**Amount of Released Energy (MeV)**	**Principal Location of Energy Deposition**
Fission: Instantaneous Energy	Kinetic Energy of Fission Fragments	80.5	161	Fuel
	Kinetic Energy of Newly-Born Fast Neutrons	2.5	5.0	Moderator
	γ-Energy Released at Time of Fission	2.5	5.0	Fuel and Structures
Fission: Delayed Energy	Kinetic Energy of Delayed Neutrons	0.02	0.04	Moderator
	β-Decay Energy of Fission Products	3.0	6.0	Fuel Materials
	Neutrinos from β-Decay	5.0	10.0	Unrecoverable
	γ-Decay Energy of Fission Products	3.0	6.0	Fuel and Structures
Neutron Capture	Non-fission Reactions Due to Excess Neutrons & β- and γ-Decay Energy of (n, γ) Products	3.5	7.0	Fuel and Structures
Total		~ 100	~ 200	

recoverable energy release per fission is:

$$\chi_f = 190 \text{ MeV} = 3.04(10^{-11}) \text{ J} \tag{3.174}$$

The main forms of heat transfer from the fuel centerline to the fluid are conduction and convection. Each type of heat transfer requires a different set of equations. They will be addressed separately.

3.8.1 Conduction

The heat diffusion equation is the basis for the fuel pin heat conduction model implementation. It is assumed that heat conduction in the axial direction in the fuel pin is negligible; in the coupled AGENT-TH simulations performed in Chapter 4, the fuel pin is modeled using reflective boundary conditions for the neutronics, which essentially models it as an infinitely long pin, effectively making the power profile of the pin flat. The effects of temperature on the axial power profile are of greatest concern. For future versions of the TH code, axial heat conduction in the pin is recommended to be implemented for cases where reflective boundary conditions are not used. Since the heat produced from fission is assumed to be at its peak in the centerline of each fuel element, the fuel centerline temperature will be the peak of the fuel element's radial temperature. The heat distribution at the edge of the fuel element's cladding will be lower.

The heat diffusion equation is reproduced (Bergman et al., 2011) as follows:

$$\nabla(k_{TH}\nabla T) + \dot{q} = \rho c_p \frac{\partial T}{\partial t} \tag{3.175}$$

where ∇ = gradient, where, for 3D Cartesian coordinates, $\nabla = \frac{\partial}{\partial \mathrm{x}}\vec{\imath} + \frac{\partial}{\partial \mathrm{y}}\vec{\jmath} + \frac{\partial}{\partial \mathrm{z}}\vec{k}$; $\vec{\imath}, \vec{\jmath}, \vec{k}$ = unit vectors in 3D Cartesian coordinates for x, y, and z axes, respectively; k_{TH} = material thermal conductivity (W/m-K or W/m-°C); T = material temperature (K or °C); $\dot{q}$ = internal volumetric heat generation (W/m^3); $\vec{r}$ = position vector (m); t = time (s); ρ = material density (kg/m^3); c_p = constant-pressure heat capacity (J/kg-K or J/kg-°C).

Note that, since the change in temperature only is of interest, the temperatures may be measured in degrees Celsius or Kelvin, since the difference in two degrees in either

measurement system will produce the same value.

If expressed in the Cartesian coordinate system, the heat diffusion equation becomes:

$$\frac{\partial}{\partial x}\left(k_{TH}\frac{\partial T}{\partial x}\right)+\frac{\partial}{\partial y}\left(k_{TH}\frac{\partial T}{\partial y}\right)+\frac{\partial}{\partial z}\left(k_{TH}\frac{\partial T}{\partial x}\right)+\dot{q}=\rho c_p\frac{\partial T}{\partial t} \tag{3.176}$$

Since the heat transfer is assumed axially uniform at each nodal location, and the system is assumed to be at steady state, the heat diffusion equation is assumed to consist of variables solely dependent on the radius. This eliminates several variables in the equation above to produce:

$$\frac{d}{dx}\left(k_{TH}\frac{dT}{dx}\right)+\dot{q}=0 \tag{3.177}$$

The partial differential equation describing heat conduction then becomes a simple ordinary differential equation in one dimension.

Solving for the volumetric heat generation term:

$$\dot{q}=-\frac{d}{dx}\left(k_{TH}\frac{dT}{dx}\right) \tag{3.178}$$

Separating variables:

$$\dot{q}\,dx=-k_{TH}\frac{dT}{dx} \tag{3.179}$$

The volumetric heat generation term may be expressed as:

$$\dot{q} = \frac{d}{dx}(q''_{cond}) \tag{3.180}$$

where q''_{cond} = heat flux due to conduction (W/m^2). Thus:

$$\dot{q}\, dx = \frac{d}{dx}(q''_{cond})\, dx = q''_{cond} \tag{3.181}$$

Replacing in the equation above:

$$q''_{cond} = -k_{TH}\frac{dT}{dx} \tag{3.182}$$

This equation is commonly known as Fourier's Law of heat conduction in one dimension. This will be used to calculate the heat transfer through a solid medium to determine the temperatures at the center or edges as applicable.

3.8.2 Convection

To account for convective heat transfer (i.e., heat transfer due to the thermal gradient between a moving fluid and another fluid or surface), Newton's Law of Cooling is used (Bergman et al., 2011):

$$q''_{conv} = \mathrm{h}_{conv}(T_s - T_\infty) \tag{3.183}$$

where q''_{conv} = heat flux due to convection (W/m^2), h_{conv} = convection heat transfer coefficient (W/m^2-K or W/m^2-°C), T_s = temperature of surface (K or °C), and T_∞ = temperature of flowing fluid (K or °C).

3.8.3 Thermal Resistance Equivalent Circuit

The cross section of a LWR cylindrical fuel element and the surrounding coolant (in this case, H_2O) is included in Figure 3.8, which is not necessarily to scale. The fuel is typically composed of enriched uranium-zirconium hydride (UZrH), as in the case of research reactors such as TRIGA, or of UOX (uranium dioxide) or MOX (mixed oxide) fuels in commercial reactors. The fuel is surrounded by a gap layer to allow room for the emitted gases from fission decay products. Without such a gap, material stresses would build up and could potentially cause a failure in the outer cladding, often made of aluminum or of zirconium or steel alloys. Surrounding the fuel cladding is the coolant, which, in the case of a LWR, is simply H_2O or light water. The light water acts as a

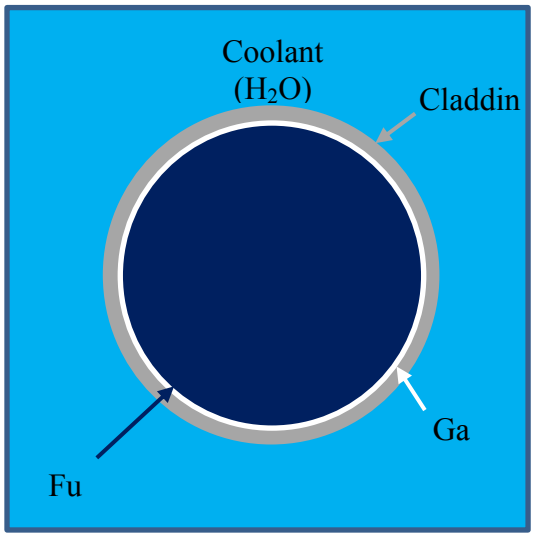

Figure 3.8. Cross section of a light water reactor (LWR) fuel element.

coolant and a neutron moderator, increasing the reactor criticality.

Included in the TH thermal hydraulics code presented in this thesis is a fuel pin temperature model. This is made using the heat diffusion equation and Newton's Law of cooling as stated above. This is done by using thermal circuits which requires calculating the equivalent thermal resistances.

To better illustrate this concept, Ohm's Law for electrical circuits is introduced:

$$\Delta V = IR \tag{3.184}$$

where V = voltage (V), I = electric current (A), and R = electrical resistance (Ω or ohms).

When comparing Ohm's Law to the heat diffusion equation, the analog for voltage is temperature, current for heat flux, and thermal conductivity for resistance. Solving Ohm's Law for resistance:

$$R = \frac{\Delta V}{I} \tag{3.185}$$

The electrical resistance can be seen as the ratio of the voltage (or potential) versus the electrical current. A thermal resistant circuit may be defined as the ratio of the thermal potential, or change in temperature, versus the thermal current, or heat rate:

$$R_{TH} \equiv \frac{\Delta T}{q} = \frac{\Delta T}{q'' A} \tag{3.186}$$

Restating the heat diffusion equation using finite differences instead of differential elements gives us:

$$q''_{cond} = -k_{TH}\frac{\Delta T}{\Delta x} \tag{3.187}$$

where Δx = distance between finite difference nodes (m).

The heat rate is desired before creating an equivalent thermal circuit. This is done by simply multiplying the heat flux due to conduction by the cross-sectional area:

$$q_{cond} = Aq''_{cond} \tag{3.188}$$

where q_{cond} = heat rate due to conduction (W) and A = cross-sectional area (m^2).

If the analogous quantities for heat transfer are replaced in the above Ohm's Law solved for electrical resistance, an equivalent thermal resistance for heat conduction is defined:

$$R_{TH,cond} \equiv \frac{\Delta T}{q''_{cond}A} = \frac{\Delta T}{q_{cond}} = \frac{\Delta x}{k_{TH}A} \tag{3.189}$$

where $R_{TH,cond}$ = equivalent thermal resistance for heat conduction (K/W or °C/W).

This may similarly be performed for convection:

$$R_{TH,conv} \equiv \frac{\Delta T}{q''_{conv}A} = \frac{\Delta T}{q_{conv}} = \frac{1}{\mathrm{h}_{conv}A} \tag{3.190}$$

where $R_{TH,conv}$ = equivalent thermal resistance for heat convection (K/W or °C/W) and q_{conv} = heat rate due to convection (W).

A thermal circuit is created by arranging thermal resistances in series or parallel as one would with an electrical circuit. The resistances calculated above were assumed to be used for one-dimensional heat transfer within a wall. Before a thermal circuit can be created for the fuel element in Figure 3.8, similar equations must be developed in cylindrical coordinates.

Beginning with the original heat diffusion equation:

$$\nabla \cdot k_{TH} \nabla T + \dot{q} = \rho c_p \frac{\partial T}{\partial t} \tag{3.191}$$

Evaluating in cylindrical coordinates:

$$\frac{1}{r}\frac{\partial}{\partial r}\left(k_{TH} r \frac{\partial T}{\partial r}\right) + \frac{1}{r^2}\frac{\partial}{\partial \theta}\left(k_{TH}\frac{\partial T}{\partial \theta}\right) + \frac{\partial}{\partial \mathrm{z}}\left(k_{TH}\frac{\partial T}{\partial \mathrm{z}}\right) + \dot{q} = \rho c_p \frac{\partial T}{\partial t} \tag{3.192}$$

where r = radius (m) and θ = polar angle (radians).

Solving Eq. (3.192) for steady-state and assuming the change in temperature is negligible for all but the radial direction, r:

$$\frac{1}{r}\frac{\partial}{\partial r}\left(k_{TH} r \frac{\partial T}{\partial r}\right) + \dot{q} = 0 \tag{3.193}$$

Solving for heat generation rate results in the following:

$$\dot{q} = -\frac{1}{r}\frac{\partial}{\partial r}\left(k_{TH} r \frac{\partial T}{\partial r}\right) \tag{3.194}$$

Separating variables and replacing volumetric heat parameter with heat flux as done with the Cartesian equation gives us:

$$q''_{TH,cond} = -\frac{1}{r} k_{TH} r \frac{\partial T}{\partial r} = k_{TH} \frac{\partial T}{\partial r} \tag{3.195}$$

This results in the same equation as using the one-dimensional Cartesian equation, replacing distance x with radius r.

Solving the conduction heat flux equation for the total heat rate gives us:

$$q_{cond} = A q''_{TH,cond} = A k_{TH} \frac{\partial T}{\partial r} = (2\pi r L) k_{TH} \frac{\partial T}{\partial r} \tag{3.196}$$

where L = length of rod section (m).

Solving for the differential temperature term results in the following:

$$\frac{\partial T}{\partial r} = \frac{q_{cond}}{(2\pi r L) k_{TH}} \tag{3.197}$$

Separating variables in the above equation gives us:

$$dT = \frac{q_{cond}}{(2\pi L) k_{TH}} \left(\frac{dr}{r}\right) \tag{3.198}$$

Integrating results in the following:

$$\int_{T_1}^{T_2} dT = \int_{r_1}^{r_2} \frac{q_{cond}}{(2\pi L)k_{TH}}\left(\frac{dr}{r}\right) \tag{3.199}$$

$$\Rightarrow (T_2 - T_1) = \Delta T = \frac{q_{cond}}{(2\pi L)k_{TH}} \ln\left({}^{r_2}/_{r_1}\right) \tag{3.200}$$

Finally, solving for q_{cond} gives us:

$$q_{cond} = \frac{\Delta T(2\pi L)k_{TH}}{\ln\left({}^{r_2}/_{r_1}\right)} \tag{3.201}$$

This is used to later determine the thermal equivalent resistance.

The convection equation is the same as described earlier in this section. Solving for its heat rate:

$$q_{conv} = Aq''_{TH,conv} = A\mathrm{h}_{conv}(T_s - T_\infty) = (2\pi rL)\mathrm{h}_{conv}\Delta T \tag{3.202}$$

The equivalent thermal circuits for conduction and convection thermal transfer for a cylinder are needed. First, the conduction equation is, again, the ratio of the potential (ΔT) and heat rate (q) multiplied by area (A):

$$R_{TH,cond} \equiv \frac{\Delta T}{q''_{cond}A} = \frac{\Delta T}{q_{cond}} = \frac{\Delta T}{\frac{\Delta T(2\pi L)k_{TH}}{\ln(r_2/r_1)}} = \frac{\ln(r_2/r_1)}{(2\pi L)k_{TH}} \qquad (3.203)$$

For convection:

$$R_{TH,conv} \equiv \frac{\Delta T}{q''_{conv}A} = \frac{\Delta T}{q_{conv}} = \frac{\Delta T}{(2\pi rL)\mathrm{h}_{conv}\Delta T} = \frac{1}{(2\pi rL)\mathrm{h}_{conv}} \qquad (3.204)$$

Figure 3.9 shows the equivalent thermal circuit for the cylindrical fuel element shown in Figure 3.8. The variables T_{max} and T_m are the centerline or maximum fuel and bulk coolant temperatures, respectively. The latter temperature is found using the coolant temperature calculations previously described in this chapter. The centerline of the fuel rod is assumed to be at a cylindrical radius equal to zero, assuming cylindrical symmetry in regards to temperature distribution in each pin; note that the 4π term for the fuel resistance is addressed by Todreas & Kazimi (1990). The variables r_{gap} and r_{clad} are the outer radii for the gap and clad, respectively. The variables $\mathrm{h}_{conv,gap}$ and $\mathrm{h}_{conv,m}$ are the convection heat transfer coefficient for the gap and fluid near the pin wall, respectively.

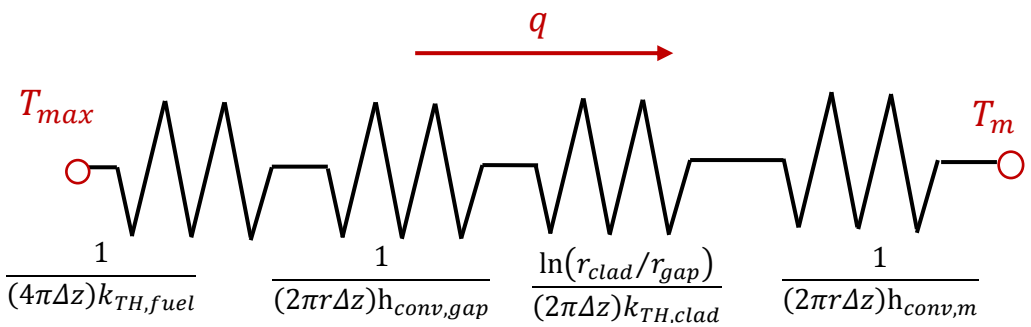

Figure 3.9. Equivalent thermal circuit for fuel element.

Thermal conductivities for the fuel and cladding are $k_{TH,fuel}$ and $k_{TH,clad}$, respectively.

The total thermal resistance of the circuit is:

$$R_{TH} = \sum R_{TH,cond} + \sum R_{TH,conv} \tag{3.205}$$

Solving the thermal resistance equation for the centerline fuel temperature gives us:

$$T_{max} = T_m + R_{TH} q'' A_s \tag{3.206}$$

The average fuel temperature is used to calculate a more accurate cross section for the fuel at that location using Scale. This temperature may be found using a logarithmic mean (required due to the cylindrical pin shape). The logarithmic mean for the temperature of the fuel, $\bar{T}_{fuel}$, is:

$$\bar{T}_{fuel} = \frac{T_{max} - T_{s,fuel}}{\ln\left(T_{max}/T_{s,fuel}\right)} \tag{3.207}$$

where $T_{s,fuel}$ represents the temperature at the fuel outer radius (or the edge of the fuel which contacts the gap). Similarly, the logarithmic mean for the temperature of the cladding, $\bar{T}_{clad}$, is found with the following equation:

$$\bar{T}_{clad} = \frac{T_{si,clad} - T_{so,clad}}{\ln\left(T_{si,clad}/T_{so,clad}\right)} \tag{3.208}$$

where $T_{si,clad}$ and $T_{so,clad}$ are the inner and outer cladding, respectively.

3.9 Heat Transfer Coefficients

3.9.1 Conduction

An added level of complexity to calculating the fuel pin temperature is that the heat transfer properties, including the thermal conductivity, are dependent on temperature. Ronchi et al. (1999) have developed an equation relating the thermal conductivity of uranium dioxide (UO_2) to the material temperature which has been validated against experimental data, neglecting radiation contribution. This relation is as follows:

$$k_{TH,UO_2} = \left(\frac{10^2}{6.548 + 23.533t} + \frac{6400 \exp\left[-16.35/t \right]}{t^{5}/_{2}} \right) \tag{3.209}$$

where k_{TH,UO_2} = thermal conductivity of uranium dioxide (W/m-K) and

$$t = \frac{T_{fuel}}{1000 \text{ K}} \tag{3.210}$$

3.9.2 Convection

The coefficients for convection heat transfer from the coolant mixture to the outer cladding depend on the Reynolds number, Prandtl number, and void fraction of the flow mixture. Each of the different stages in the net vapor generation model shown in Figure 3.4 requires a different set of equations for the convection heat transfer coefficient. The equations are applied to the coolant surrounding each pin individually using average flow

quantities (temperature, Reynolds number, etc.) from each of the subchannels.

An important parameter for determining the convection heat transfer coefficient is the Nusselt number:

$$Nu \equiv \frac{\mathrm{h}_{conv} D_h}{k} \tag{3.211}$$

The Nusselt numbers are dependent on the geometry, properties, and dynamics of the coolant flow. These are often determined using empirical data. The Nusselt numbers for each pin are calculated assuming a smooth pipe configuration. The equations used for each of the stages of void fraction development from Figure 3.4 are discussed.

Note that the convection heat transfer coefficient for the gap is not easily calculated, depending on amount of contact between the fuel and cladding (due to swelling and manufacturing processes) and the amount of fission products emitted in the gap due to burnup, among other factors (Todreas & Kazimi, 1990). For now, the gap convection coefficient must be provided by the user. Future work includes implementing a model for calculating gap conductance.

3.9.2.1 Single Phase

For laminar flow (Re < 2300), the flow requires a distance of travel, called the entry length, before it fully develops. The entry length for laminar flow, L_e, may be approximated as:

$$L_e \approx 0.05 \cdot Re \cdot Pr \cdot D_h \tag{3.212}$$

where the parameters are averaged over the length of each pin. The Prandtl number is defined as:

$$Pr \equiv \frac{c_p \mu}{k} \tag{3.213}$$

The entry region (i.e. $L < L_e$) is the length along which the flow velocity profile has not reached full development. In this region, the Nusselt number may be calculated as:

$$Nu = 1.86 \left(\frac{D_h \cdot Re \cdot Pr}{L} \right)^{1/3}, \qquad 0.48 < Pr < 16{,}700 \tag{3.214}$$

For the fluid past the entry region, or the fully-developed region (i.e. $L \geq L_e$), the equation assuming constant heat flux is:

$$Nu = 4.36 \tag{3.215}$$

For turbulent flow where Reynolds numbers of the fluid exceed 10,000, the Dittus-Boelter equation for a heated fluid is applicable:

$$Nu = 0.023 \cdot Re^{0.8} \cdot Pr^{0.4}, \qquad 0.7 < Pr < 160 \tag{3.216}$$

For transitional regions (i.e., between laminar and turbulent flow regions), the Gnielinski correlation (Bergman et al., 2011) may be applied. This correlation applies

over a wide range of Peclet and Reynolds numbers (up to $Re = 5(10^6)$), including the transition region. The Gnielinski correlation is as follows:

$$Nu = \frac{(f/8) \cdot (Re - 1000) \cdot Pr}{1 + 12.7 \cdot (f/8)^{0.5} \cdot (Pr^{2/3} - 1)}, \qquad 0.5 < Pr < 2000 \qquad (3.217)$$

3.9.2.2 Subcooled Nucleate Boiling and Saturated Boiling

Upon revisiting Figure 3.4, subcooled nucleate boiling begins at the axial location along the height of the pin $z = Z_{NB}$. This location represents a transition point at which nucleate boiling occurs at the walls of the fuel elements, yet the bulk temperature of the coolant is still below saturation (i.e., subcooled or condensed liquid). Since the bulk liquid is subcooled, bubbles exit the wall and quickly collapse due to its energy being dispersed within the subcooled liquid. This results in a nonzero yet very small void fraction in the liquid (which Todreas & Kazimi (1990) indicate may generally be neglected). Bergles and Rohsenow created a criterion above which the heat flux must be in order for bubble nucleation to occur for water between pressures of 0.1 and 13.6 MPa:

$$q'' = 15.6 \cdot P^{1.156} \cdot (T_s - T_{sat})^{2.3/p^{0.0234}} \qquad (3.218)$$

The point at which bubbles escape from the wall without first collapsing is known as the point of bubble departure. These bubbles detach regularly and condense slowly. This occurs at the location depicted in Figure 3.4 as $z = Z_D$.

The point of bubble departure has been described using different criteria as thermally or hydrodynamically controlled. These criteria are typically based on the assumption that,

at this point, the wall heat flux is balanced by liquid subcooling. After this point, the void fraction of the bulk fluid increases substantially.

The bulk fluid reaches saturation at the axial height $z = Z_B$. As in the second stage of bubble departure, the heat transfer in the early stages of saturated boiling depends on the amount of bubble nucleation at the wall. The equations used in the bubble departure region are still applicable in the case that nucleation exists.

As void fraction increases, the bulk fluid reaches equilibrium at $z = Z_E$. When flow quality increases greatly, the liquid film at the pin walls thins, leading to evaporation and entrainment of water droplets. Nucleation becomes suppressed as the heat transfer from the liquid film to the gaseous region in the subchannel becomes more efficient. Evaporation occurs in annular flow at the interface between the gaseous core and liquid film.

Chen described a correlation that may be applicable for all stages of saturated boiling. The heat flux for this model follows the form

$$q'' = \mathrm{h}_{2\phi}(T_w - T_{sat}) \tag{3.219}$$

since it is assumed that the bulk fluid is at saturation temperature. The two-phase convection heat transfer coefficient is expressed in the form

$$\mathrm{h}_{2\phi} = \mathrm{h}_{NB} + \mathrm{h}_{conv} \tag{3.220}$$

The convective term is a modified form of the Dittus-Boelter correlation:

$$\mathrm{h}_{conv} = 0.023\left(\frac{G(1-x)D_h}{\mu_f}\right)^{0.8} \cdot \left(Pr_f\right)^{0.4} \cdot \left(\frac{k_f}{D_h}\right) \cdot F \tag{3.221}$$

where F is a factor which takes into account enhanced flow and turbulence due to vapor. It is approximated as

$$F = \begin{cases} 1 & \text{for } (X_{tt})^{-1} < 0.1 \\ 2.35(0.213 + (X_{tt})^{-1})^{0.736} & \text{for } (X_{tt})^{-1} > 0.1 \end{cases} \tag{3.222}$$

where

$$(X_{tt})^{-1} = \left(\frac{x}{1-x}\right)^{0.9}\left(\frac{\rho_f}{\rho_g}\right)^{0.5}\left(\frac{\mu_g}{\mu_f}\right)^{0.1} \tag{3.223}$$

The nucleation term in the Chen correlation is based on the Forster-Zuber equation:

$$\mathrm{h}_{NB} = \mathrm{S} \cdot 0.00122 \cdot \left[\frac{\left(k^{0.79}c_p^{0.45}\rho^{0.49}\right)_f}{\sigma^{0.5}\mu_f^{0.29}h_{fg}^{0.24}\rho_g^{0.24}}\right] \cdot (\Delta T_{sat})^{0.24} \cdot (\Delta P)^{0.75} \tag{3.224}$$

where

$$\Delta T_{sat} = T_s - T_{sat} \tag{3.225}$$

$$\Delta P = P(T_s) - P(T_{sat}) \tag{3.226}$$

The quantity S is a suppression factor which is a function of the Reynolds number. It may be approximated as

$$\mathrm{S} = \frac{1}{1 + 2.53 \cdot 10^{-6} \cdot Re^{1.17}} \tag{3.227}$$

where the Reynolds number is calculated as

$$Re = Re_l F^{1.25} \tag{3.228}$$

and

$$Re_l = \frac{G(1-x)D_h}{\mu_f} \tag{3.229}$$

Collier (Todreas & Kazimi, 1990) discussed a possible extension of the Chen correlation to the subcooled boiling region. The heat flux in this case follows the form

$$q'' = \mathrm{h_{NB}}(T_w - T_{sat}) + \mathrm{h_c}(T_w - T_m) \tag{3.230}$$

In the case of subcooled nucleate boiling, Collier suggested

$$F = 1 \tag{3.231}$$

And S may be calculated assuming the quality is zero. This affects the original equation for Re_l thus:

$$Re_l = \frac{GD_h}{\mu_f} \tag{3.232}$$

These equations are implemented to calculate the heat transfer in the subcooled nucleate boiling and saturated boiling regions.

Once the average fuel temperatures are calculated, they are used in Scale to determine cross sections which are implemented in the AGENT neutronics code which is discussed in the following section.

3.10 Coupling Scheme Between Scale, AGENT, and TH

The coupling scheme between the Scale, AGENT, and TH codes is discussed in this section. The inputs required for each code as well as the outputs produced by each code (which are, in turn, used as inputs for the following code) are introduced and discussed.

Figure 3.10 shows the overall coupling scheme between the Scale, AGENT, and TH codes. To begin, the nuclear system properties (geometry, including lattice pitch, fuel rod radius and length, fuel channel areas, coolant mass flow rates, etc.) must be known. These inputs are used in the Scale software to determine the macroscopic cross sections for the system at each axial node for each fuel pin. These macroscopic cross sections are used as inputs for the AGENT neutronics code. The AGENT neutronics code then determines the normalized power profile for each pin at each 2D radial plane; these planes are then coupled in the 1D axial direction by AGENT (as described in Chapter 2).

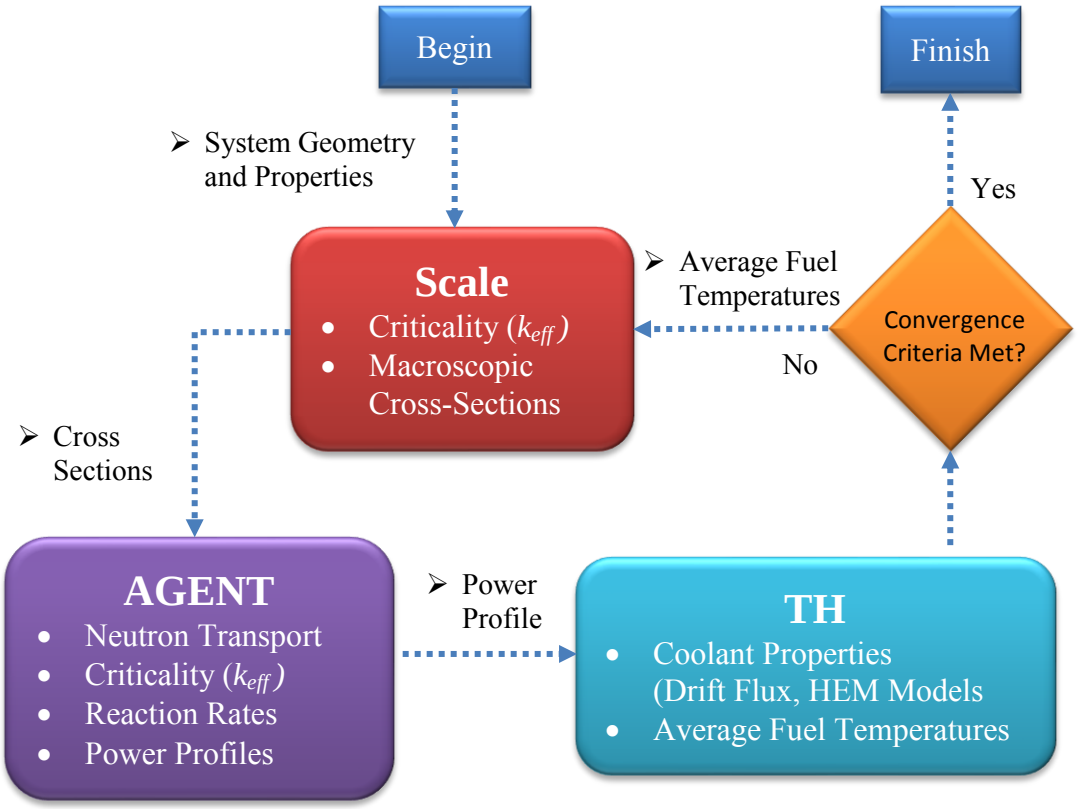

Figure 3.10. AGENT-TH coupling scheme between Scale, AGENT, and TH codes.

The normalized power values for each fuel pin at each axial node are used in the TH thermal hydraulics code to modify the heat flux to the coolant from the fuel pin at each node. The TH code must assume a total power for the pin or assembly of pins being analyzed, as the results from the AGENT neutronics code do not allow for a direct calculation of assembly power, only a normalized power profile. The TH code utilizes the two models described in this chapter, including the drift flux model, as has been implemented by Galloway (2010) in the NESTLE code, to model BWRs, and the HEM model, as described in this chapter, to model PWRs. Both models are implemented in the TH code in a 1D analysis at each axial node along the coolant subchannels. The results from the hydrodynamic models implemented in the TH code are used with a 1D radial heat transfer model for each subchannel node to determine the average fuel pin

temperatures at each axial node.

With the average temperatures for the fuel, cladding, and coolant known, these are then entered into Scale to account for temperature effects on the materials. This will modify the macroscopic cross sections (typically only slightly) for each iteration. The user must determine if the coupled Scale, AGENT, and TH codes results have sufficiently converged. If not, the process is continued until convergence is reached. In the example used with a single BWR pin, convergence was reached after the 3rd iteration, as is described in Chapter 4. The following chapter will show several example benchmarks, including those using the TH hydrodynamic model alone, along with others, including the entire coupled AGENT-TH code scheme, as depicted in Figure 3.10.

CHAPTER 4

EXAMPLES USING TH CODE AND COUPLED AGENT-TH CODE

4.1 Introduction

The first two examples in this section are included as benchmarks between the drift flux and HEM hydrodynamic models used in the TH code as compared against TRACE, a code used to model nuclear power plant systems, including pipes, heat exchangers, light water reactors, etc. in both transient and steady-state operations (TRACE V5.0 THEORY MANUAL). The TRACE code allows for analysis of the coolant properties of the LWR core under analysis, including pressure, temperature, void fraction, etc. These properties are compared against those produced from the TH thermal hydraulics code to benchmark its capabilities and contrast the results from both codes.

While both the TRACE software and coupled AGENT-TH code both are capable of modeling both the thermal-hydraulic and neutronics behavior of LWR systems, they do differ slightly in the methods of calculation. Several main differences that exist between TRACE and the coupled AGENT-TH code are as follows:

1. TRACE code is capable of performing steady-state or transient analyses; the coupled AGENT-TH code is currently designed to perform steady-state analyses only.
2. TRACE is capable of including specific LWR and related components (heat

exchangers, pumps, pipes, etc.); the coupled AGENT-TH code currently only models LWR cores (the AGENT code may be used for neutronics analysis in 2D/3D for any desired geometry, however).

3. The AGENT neutronics code provides criticality calculations using a deterministic solution to the neutron transport equation in 2D and 3D; the TRACE code uses a point kinetics method with reactor feedback for calculating reactor power (3D transient neutronics calculations are possible in TRACE only when coupled with the PARCS neutronics code (Joe et al., 1998).
4. TRACE uses a more computationally-intensive and more accurate two-fluid hydrodynamic model for the coolant; the AGENT-TH code uses the drift flux model for BWR analysis and the HEM model for PWR analysis.

The benchmarks in this chapter for the drift flux and HEM models for BWR and PWR pin analyses, respectively, show very high accuracy and agreement with the results as provided by the more computationally intensive results provided by TRACE. The accuracy of the TH code's hydrodynamic models (drift flux and HEM) is compared against TRACE first, and the last benchmark shows the coupled AGENT-TH code capability versus the TRACE software.

4.2 Drift Flux Benchmark

A single BWR pin adapted from the study by Hoogenboom et al. (2011) is used as a benchmark for the drift flux model as implemented in the TH code. The example used in the Hoogenboom et al. study was a 3x3 pin bundle; in order to adapt it for comparison

using a single pin, the coolant subchannel flow areas and assembly size were reduced to a single pin. The mass flow rate was also reduced by one-ninth the original value in order to account for the smaller coolant subchannel. The inlet temperature and outlet pressure for the fluid were kept the same, however, as these are intensive properties (i.e., they do not depend on the quantity of the fluid). The single pin's cross section has a similar appearance to Figure 3.8. The properties used in this analysis are included in Table 4.1. Note that a gap is included in the TRACE model with a thickness of 0.001 cm for this example only. The results of the analysis are shown in Figures 4.1 through 4.6. In succession, the figures contain the plots for void fraction, true quality, pressure, mean saturation temperature, mixture temperature, and specific energy along the axial direction

Table 4.1. Properties of single BWR pin adapted from the study by Hoogenboom et al. (2011) for validation of drift flux model used with the TH code and TRACE. The TRACE model included a 0.001 cm gap between the fuel and cladding (Submitted on 08/20/2015 to "Progress in Nuclear Energy").

Property	**Value**
Fuel Pin Radius	0.5375 cm
Fuel Pellet Radius	0.4555 cm
Fuel Pin Pitch	1.43 cm
Fuel Material	UO_2
Total Pin Power	61.22 kW
Axial Power Profile	Flat
Fuel Density	10.25 g/cm^3
Cladding Material	Zr (pure)
Cladding Density	5.77 g/cm^3
Coolant Material	H_2O
Inlet Coolant Density	753.61 kg/m^3
Inlet Coolant Velocity	1.4525 m/s
Inlet Coolant Liquid Temperature	545.00 K (271.85 °C)
Outlet Coolant Pressure	7.06 MPa
Fuel Pin Length	3.71 m

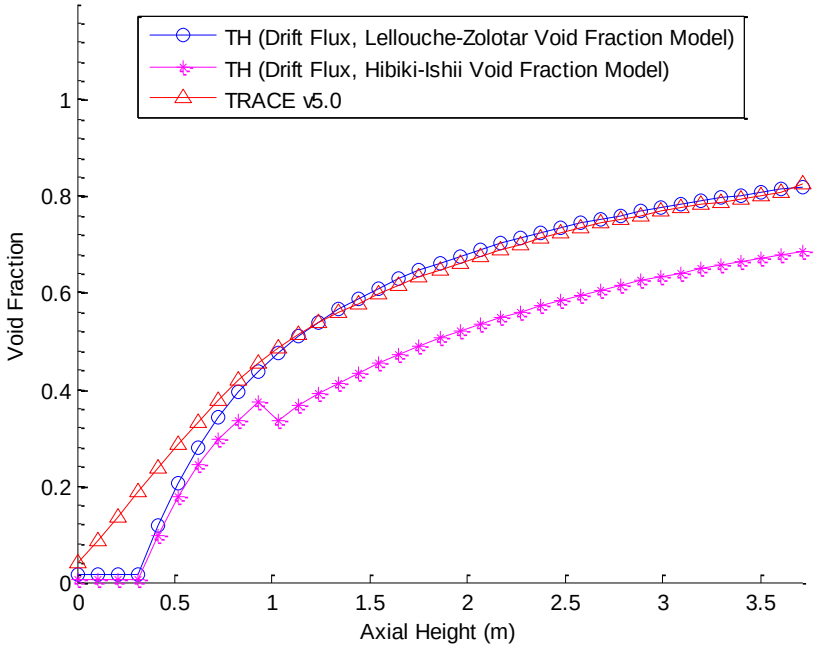

Figure 4.1. Void fraction versus axial height of single BWR pin analysis adapted from the study by Hoogenboom et al. (2011) using TH drift flux model (Submitted on 08/20/2015 to "Progress in Nuclear Energy").

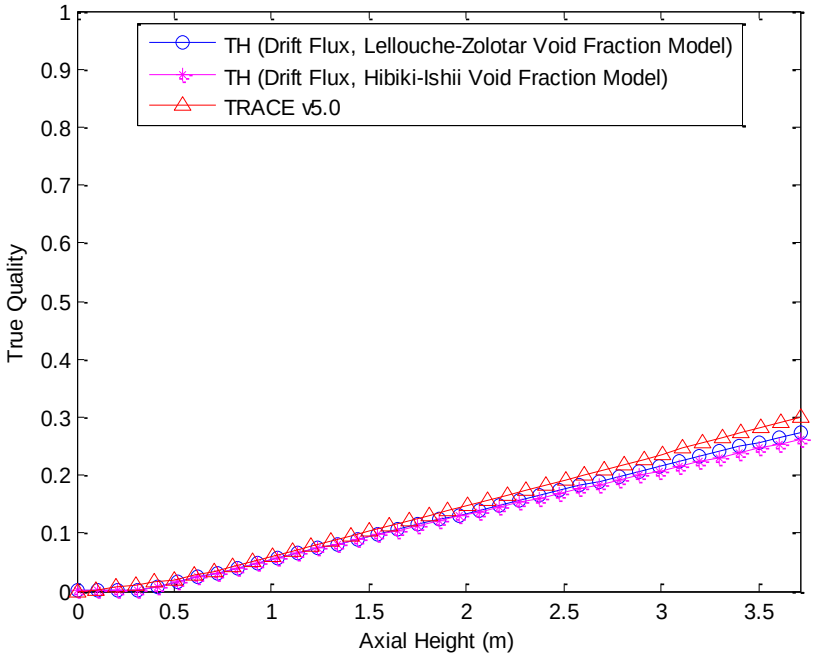

Figure 4.2. True quality, x, versus axial height of single BWR pin analysis adapted from the study by Hoogenboom et al. (2011) using TH drift flux model (Submitted on 08/20/2015 to "Progress in Nuclear Energy").

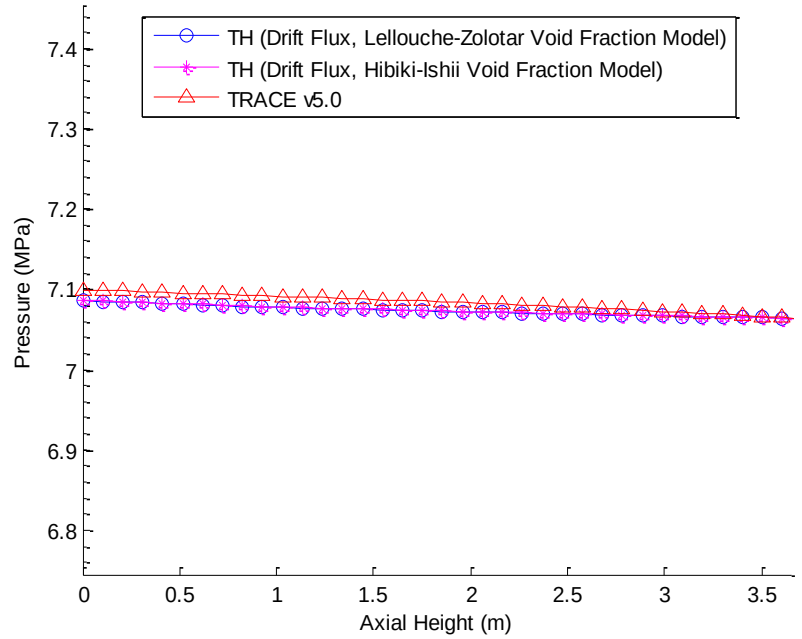

Figure 4.3. Average pressure versus axial height of single BWR pin analysis adapted from the study by Hoogenboom et al. (2011) using TH drift flux model (Submitted on 08/20/2015 to "Progress in Nuclear Energy").

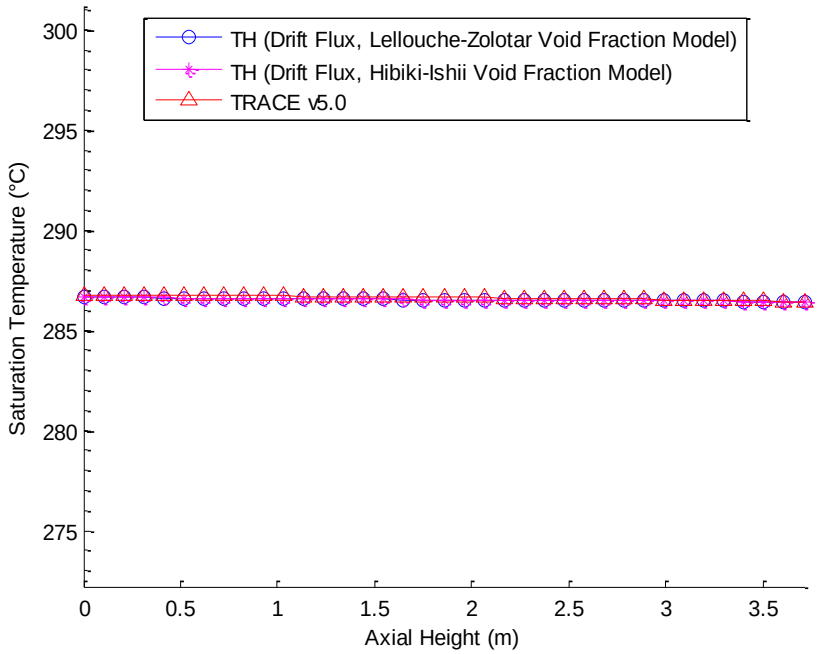

Figure 4.4. Mean saturation temperature versus axial height of single BWR pin analysis adapted from the study by Hoogenboom et al. (2011) using TH drift flux model (Submitted on 08/20/2015 to "Progress in Nuclear Energy").

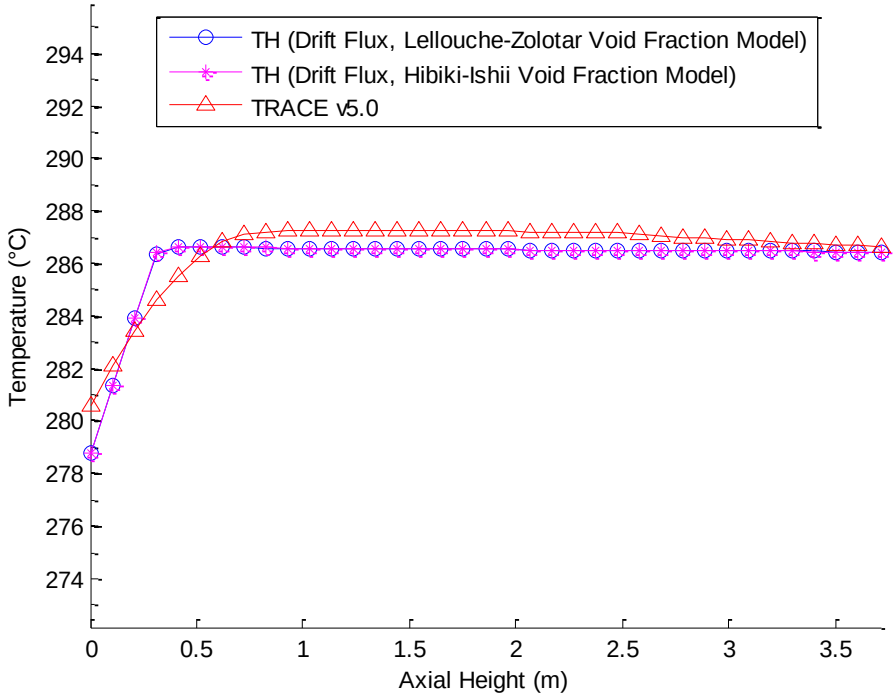

Figure 4.5. Coolant mixture temperature versus axial height of single BWR pin analysis adapted from the study by Hoogenboom et al. (2011) using TH drift flux model (Submitted on 08/20/2015 to "Progress in Nuclear Energy").

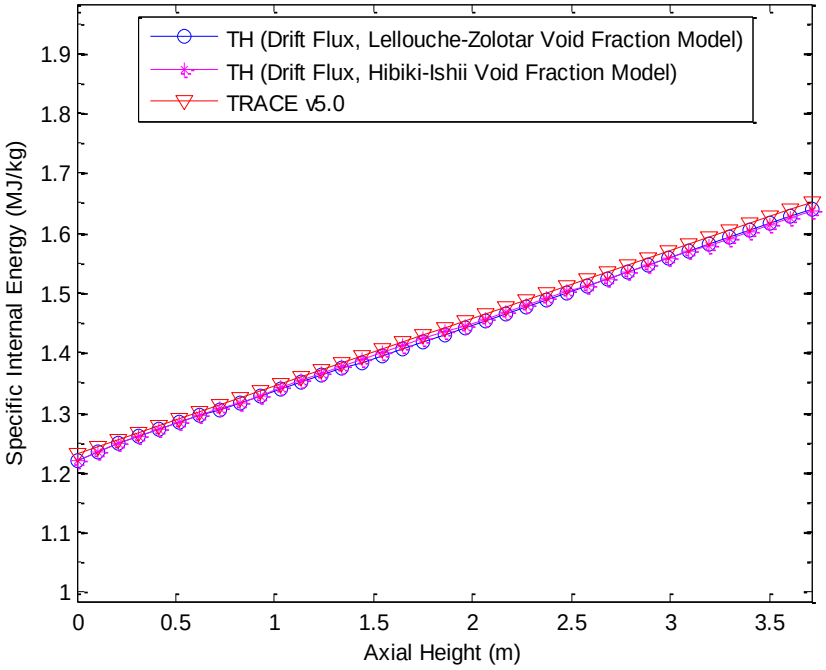

Figure 4.6. Specific internal energy versus axial height of single BWR pin analysis adapted from the study by Hoogenboom et al. (2011) using TH drift flux model (Submitted on 08/20/2015 to "Progress in Nuclear Energy").

of the BWR coolant channel. Each plot includes results using two void fraction models, each based on the work by Lellouche and Zolotar (1982) and Hibiki and Ishii (2003, 2005).

As indicated in the void fraction results in Figure 4.1, the Lellouche-Zolotar void fraction model agrees with the TRACE v5.0 results to within approximately 3% at and above an axial height location of about 0.9 m. Below this axial location, discrepancies exist between the TRACE and TH results. The Net Vapor Generation model, as described in Chapter 3 and represented in Figure 3.4, includes an increase in void fraction due to subcooled nucleate boiling (i.e., boiling that occurs beginning at the heated walls prior to the coolant reaching bulk saturation temperature at the prescribed coolant pressure). However, it appears that the NVG model greatly underestimates the void fraction at the lower axial heights (below approximately $z = 0.9$ m) as compared to the results from TRACE v5.0. Although the curve in Figure 4.1 appears otherwise, the void fraction is calculated to be a finite positive value using the TH code and the drift flux model with the EPRI NVG equations [Eqs. (3.140) through (3.151)]. It is a possibility that the EPRI NVG model as implemented for calculating subcooled nucleate boiling in the TH thermal hydraulics code requires re-evaluation to increase accuracy as compared with the TRACE results.

Continuing to examine Figure 4.1, the void fraction as calculated using the implemented Hibiki-Ishii void fraction model [Eqs. (3.150) through (3.169) in conjunction with Eq. (3.50)] shows a greater discrepancy with the TRACEv5.0 results at all axial heights than does the Lellouche-Zolotar void fraction model implemented in the TH code. The TH Hibiki-Ishii void fraction curve gradually increases beginning at approximately

$z = 0.4$ until it reaches between 0.8 and 0.9 m, at which point the void fraction makes a significant drop. Above approximately 1.1 m, the void fraction continues to increase but shows a noticeable underestimation of the void fraction as compared with the TH Lellouche-Zolotar model and TRACE curves. The noticeable dip is due to the different equations being used in that region due to the coolant reaching a different boiling regime above the height at about 0.8 m. The cause for this dip may be due to discontinuities in the coolant parameters as it transitions between boiling regimes. A more precise boiling regime map than that used in Figure 3.4 may also aid in resolving both the dip in void fraction at about 0.8 m and in the underestimation of the void fraction values.

The flow quality values for the TH Lellouche-Zolotar and Hibiki-Ishii curves indicated in Figure 4.2 both agree very well (within 5% difference) with the TRACE curve. From the coolant inlet to the axial height of about 2 m in the coolant subchannels, all three curves agree to within 5% difference. Above this height until the maximum height of the subchannels (i.e., the coolant outlet), the percent difference reaches a maximum between the TRACE and TH Hibiki-Ishii curve at about 7.2% and between the TRACE and TH Lellouche-Zolotar curve at about 3.6%. In other words, the maximum percent difference above 2 m is approximately halved using the TH Lellouche-Zolotar void fraction model as compared with the TH Hibiki-Ishii void fraction model when compared with calculations from TRACE.

The axial coolant pressures in the coolant subchannels in Figure 4.3 show very excellent agreement between all three models (TH Lellouche-Zolotar model, TH Hibiki-Ishii model, and TRACE). The maximum percent difference occurs at the coolant inlet between the three models in Figure 4.3 at approximately 0.3%, with differences

decreasing as axial height increases.

The saturation temperatures displayed in Figure 4.4 agree excellently between the three models, as do the pressures in Figure 4.3. Once the coolant reaches bulk saturation conditions, it would be expected that pressures and temperatures follow very closely due to the direct correlation between saturation temperature and pressure (Cengel & Boles, 2010). At any specific axial height along the subchannels, the saturation temperatures calculated by the three models do not exceed approximately 0.5% between each other.

In order to calculate the coolant mixture temperature from the TRACE model as displayed in Figure 4.5, the following equation was used:

$$T(z) = x \cdot T_v(z) + (1 - x) \cdot T_l(z) \tag{4.1}$$

where $T(z)$ represents the mixture temperature at axial height z, $T_v(z)$ represents the vapor temperature at axial height z, and $T_l(z)$ is the liquid temperature at axial height z, with x being the flow quality (as used in equations throughout Chapter 3). The reason Eq. (4.1) is necessary is that TRACE uses a two-fluid model (TRACEV5.0 THEORY MANUAL, 2012) which allows for thermal nonequilibrium between the phases at any spatial and temporal location. The TRACE model does typically allow for higher accuracy in calculating fluid temperatures and parameters but requires more computational resources (as the number of conservation equations is doubled to account for the separate phases). The condition of phase temperature nonequilibrium inherent in the two-fluid model is not allowed in either the drift flux or the HEM models as implemented in the TH code. The different temperatures taken from TRACE at any axial

height must then be used to approximate the total mixture temperature (as it is not provided directly). If Eq. (4.1) does not allow for an accurate approximation of the two-phase mixture temperatures from TRACE, this will lead to inevitable discrepancies when compared with the TH code. An additional source of discrepancy may occur due to the slight difference in inlet coolant temperature in the TRACE model. This occurred as the different boundary conditions set for the TRACE model were slightly modified as the simulation ran in order to reach a converged solution. The discrepancy between inlet coolant temperatures is very minor, however; the TRACE model shows an elevated temperature difference at the inlet of about 1.5 degrees Celsius as compared to the TH model (less than 0.5% of any model's inlet temperature). Eq. (4.1) allows for the coolant mixture temperature to be a much smoother transition than as used in the TH code; despite this and the slightly different trend shapes between the TRACE and TH models, the maximum percent difference between the two codes is less than 1% at any axial location.

The specific internal energy of the coolants is displayed in Figure 4.6 and indicates a steady quasilinear increase between the three models from the coolant inlet to the outlet. Once again, the TH and TRACE models all agree excellently, to within approximately 1% difference at any axial location.

In summary, with the exception of void fraction calculations, the two-phase coolant parameter calculations between the TH and TRACE codes all exist within 2% at any axial height. The discrepancies in void fractions may be worthy of future investigation and refinement. If the cause of the discrepancies in void fraction calculations cannot be determined, it may be recommended to implement other void fraction models as bases of comparison and benchmarking with TRACE.

4.3 HEM Model Benchmark

The benchmark used for the HEM model has been adapted from the Hoogenboom et al. (2011) study. The information used for the benchmark is included in Table 4.2. The geometry of this example is a single PWR pin with a similar axial cross section to that given in Figure 3.8, as with the drift flux benchmark. A flat power profile is used to display the effectiveness of the hydrodynamic model (i.e., without the coupling between the TH and AGENT codes). Figures 4.7 through 4.13 display the results of this benchmark. In succession, the figures display the void fraction, true quality, pressure, saturation temperature, liquid temperature, specific internal energy, and slip ratio of the coolant mixture along the axial height of the PWR pin.

Table 4.2. Properties of single PWR pin adapted from the study by Hoogenboom et al. (2011) for validation of HEM model used with AGENT-TH and compared to results from TRACE. The trace model included a 0.001 cm gap between the fuel and cladding (Submitted on 08/20/2015 to "Progress in Nuclear Energy").

Property	**Value**
Fuel Pin Radius	0.475 cm
Fuel Pellet Radius	0.410 cm
Fuel Pin Pitch	1.26 cm
Fuel Material	UO_2
Total Pin Power	66.5 kW
Axial Power Profile	Flat
Fuel Density	10.25 g/cm^3
Cladding Material	Zr (pure)
Cladding Density	5.77 g/cm^3
Coolant Material	H_2O
Inlet Coolant Density	744.9 kg/m^3
Inlet Coolant Velocity	4.98 m/s
Inlet Coolant Liquid Temperature	545.00 K (291.085 °C)
Outlet Coolant Pressure	15.8 MPa
Fuel Pin Length	3.66 m

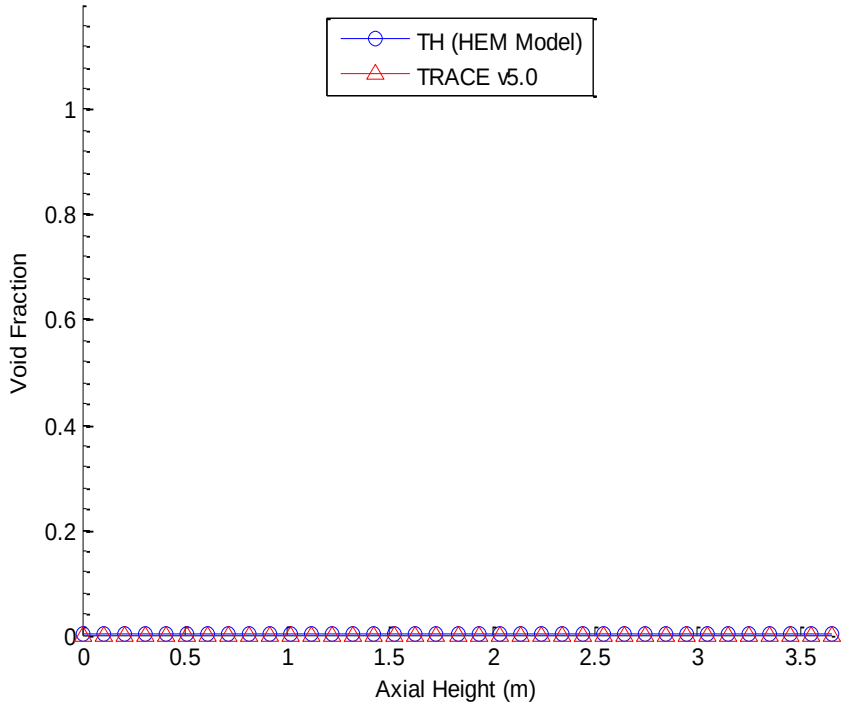

Figure 4.7. Void fraction versus axial height of analysis of PWR pin adapted from the study by Hoogenboom et al. (2011) using the HEM model in AGENT-TH as compared against TRACE model (Submitted on 08/20/2015 to "Progress in Nuclear Energy").

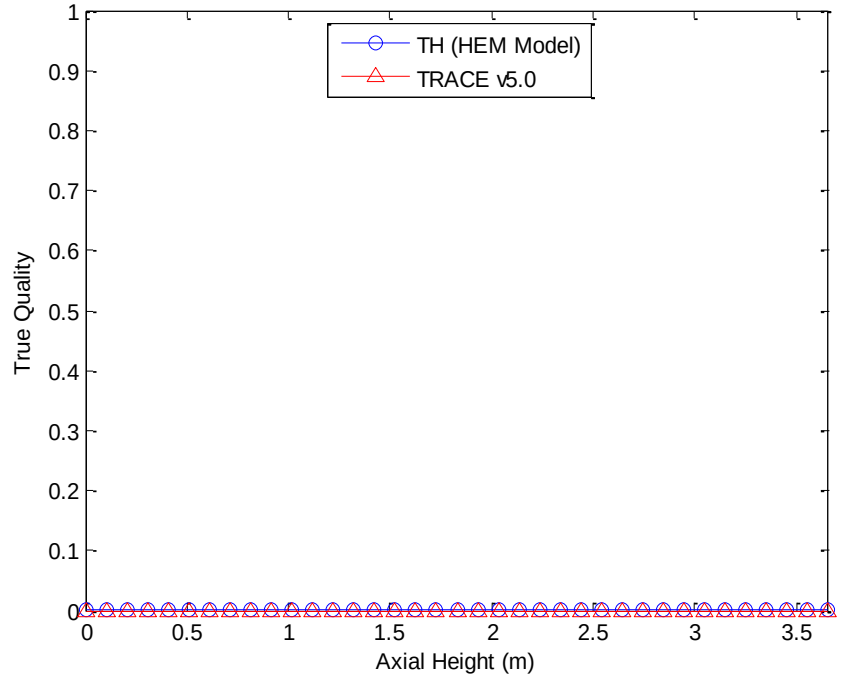

Figure 4.8. True quality, x, versus axial height of analysis of PWR pin adapted from the study by Hoogenboom et al. (2011) using the HEM model in AGENT-TH as compared against TRACE model (Submitted on 08/20/2015 to "Progress in Nuclear Energy").

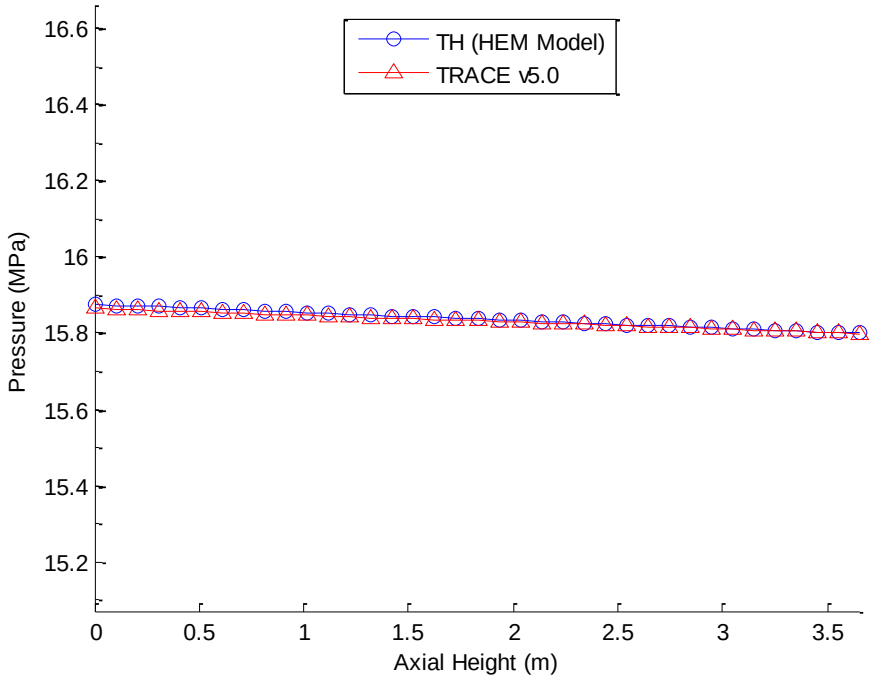

Figure 4.9. Pressure versus axial height of analysis of PWR pin adapted from the study by Hoogenboom et al. (2011) using the HEM model in AGENT-TH as compared against TRACE model (Submitted on 08/20/2015 to "Progress in Nuclear Energy").

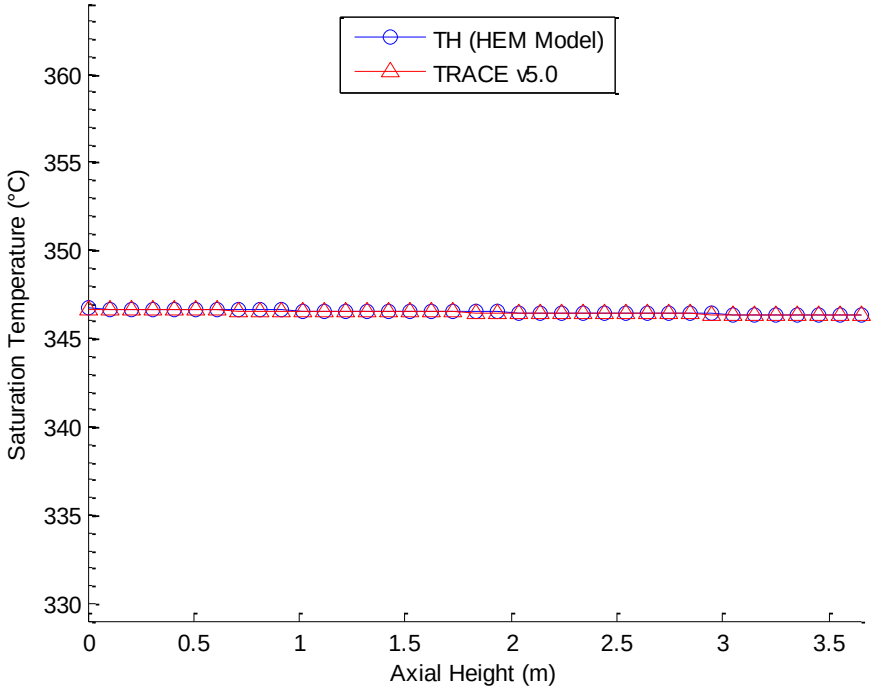

Figure 4.10. Saturation temperature versus axial height of analysis of PWR pin adapted from the study by Hoogenboom et al. (2011) using the HEM model in AGENT-TH as compared against TRACE model (Submitted on 08/20/2015 to "Progress in Nuclear Energy").

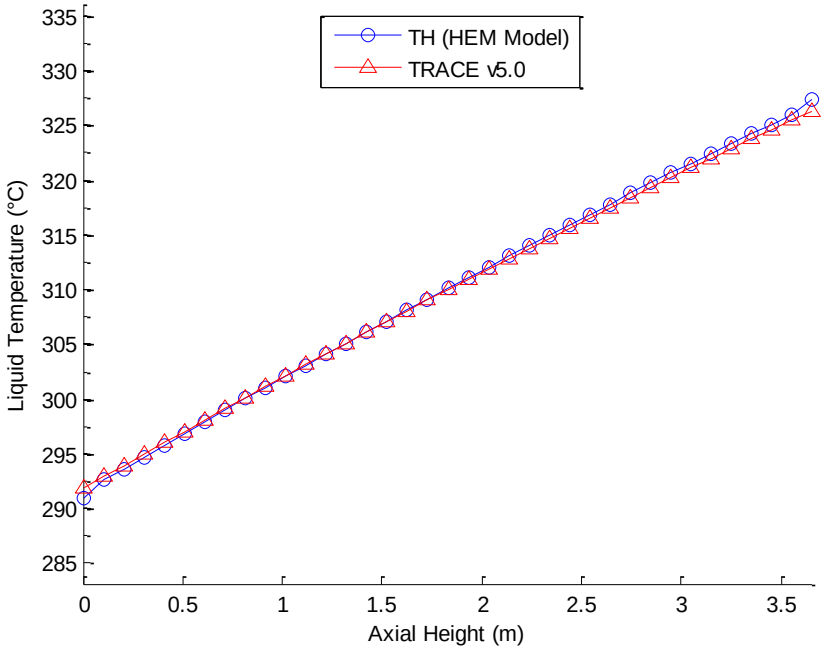

Figure 4.11. Liquid temperature versus axial height of analysis of PWR pin adapted from the study by Hoogenboom et al. (2011) using the HEM model in AGENT-TH as compared against TRACE model (Submitted on 08/20/2015 to "Progress in Nuclear Energy").

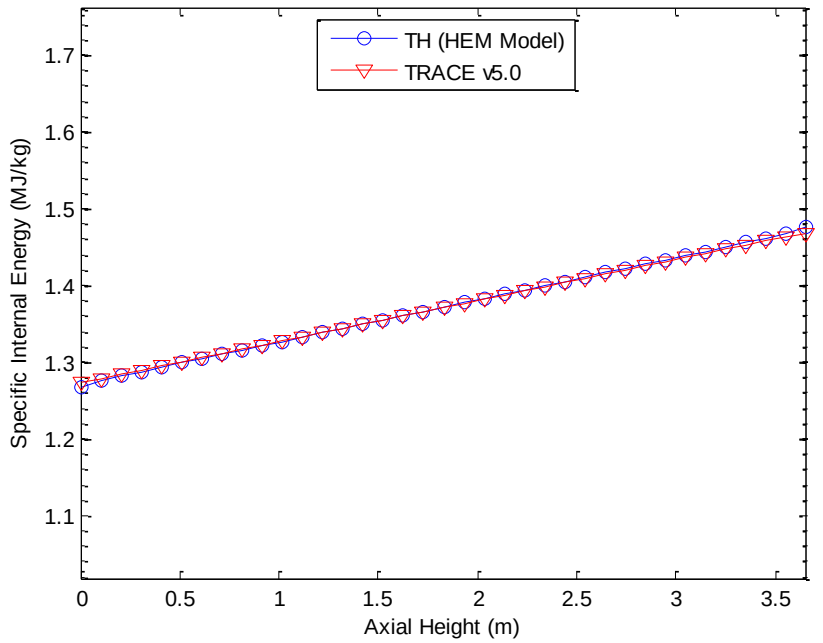

Figure 4.12. Specific internal energy versus axial height of analysis of PWR pin adapted from the study by Hoogenboom et al. (2011) using the HEM model in AGENT-TH as compared against TRACE model (Submitted on 08/20/2015 to "Progress in Nuclear Energy").

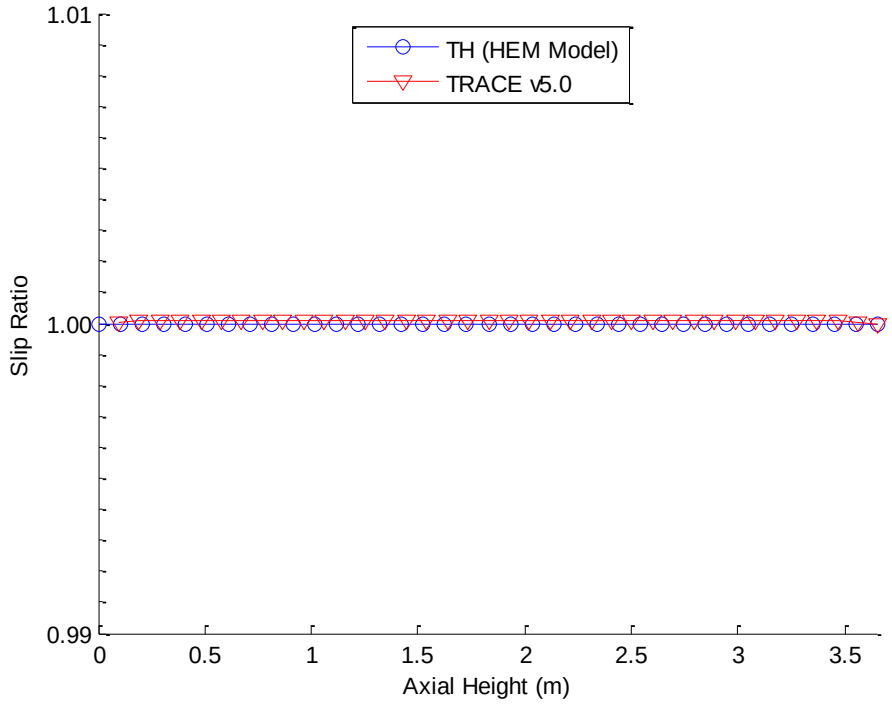

Figure 4.13. Slip ratio, *S*, versus axial height of analysis of PWR pin adapted from the study by Hoogenboom et al. (2011) using the HEM model in AGENT-TH as compared against TRACE model (Submitted on 08/20/2015 to "Progress in Nuclear Energy").

The slip ratio of the fluid along the height of the PWR coolant channel is included in Figure 4.13 because the HEM model is assumed to have a slip ratio equal to one (as described in Chapter 3). To verify that the HEM model as implemented in AGENT-TH may accurately be used for this analysis, the slip ratio as calculated from TRACE is included as a comparison. If the slip ratio deviates greatly from unity, the HEM model would not be appropriate (and the drift flux or another model would be required).

Average axial void fractions as calculated by the TH code for this PWR benchmark are included in Figure 4.7. Due to the much higher pressures inherent in the operating environment of PWRs over BWRs, it is expected that the void fractions will be very low, as indicated in the figure. This is also a strong indication that the HEM model is suitable for analyzing this particular system.

As the void fractions are inherently tied with the coolant flow quality, it is also expected that the flow quality will be very low for this PWR benchmark. This is demonstrated in the average axial coolant flow quality in Figure 4.8. As is the case with BWRs, subcooled nucleate boiling does occur but at a much reduced rate in the case of PWRs. Again, the much-lower coolant qualities (which are positive and finite) as displayed in Figure 4.8 are due to the higher operating pressures of PWRs within the coolant channels. The TRACE and TH models agree very closely in Figures 4.7 and 4.8 for the void fractions and flow qualities, respectively.

The averaged axial subchannel pressure, as calculated for the PWR benchmark by the TH and TRACE codes, is displayed in Figure 4.9. The pressures calculated by the TH HEM model and the TRACE two-fluid model show excellent agreement (to within 2% difference along the entire height of the channel). It is expected that the pressure would drop slightly due to the height differential resulting in a loss of momentum for the fluid, though it is a very small change.

Figure 4.10 indicates the saturation temperature of the coolant along the height of the PWR subchannels. As described in the results for the BWR benchmark previously in this chapter, the saturation temperatures are directly linked to saturation pressures (Cengel & Boles, 2010). As the pressure along the height of the coolant channel drops, it is expected that the saturation temperature would also slightly drop. This is the case as calculated by all three codes which show agreement at any axial height to within 2%.

Liquid temperatures for the coolant, as calculated by the TH HEM code and TRACE, are displayed in Figure 4.11. The liquid temperature taken from TRACE may be directly compared against those taken from the TH HEM code (as the fluid has no void fraction,

the vapor temperature calculated by TRACE is essentially negligible) negating the need to employ Eq. (4.1) to derive a mixture temperature. Along the entire height of the coolant subchannels, the liquid temperatures between the TH HEM and TRACE codes remain within 2% difference.

Specific internal energies for the coolant are included in Figure 4.12. The gradual increases in internal energy, as calculated by both the TH HEM and TRACE codes, agree to within 1% along the entire PWR subchannels. This provides strong evidence to the validity of the assumption that the internal energy change in the fluid due to shear stress and friction as well as due to the spatial pressure gradient is negligible. This assumption was used in the derivation of the HEM conservation equations in Chapter 3 and led to the development of the HEM enthalpy Eqs. (3.105) and (3.106). The calculated specific internal energies agree excellently between TH and TRACE.

Finally, Figure 4.13 includes the slip ratios, S, for the PWR subchannel coolant. The value for the slip ratios was provided directly from TRACE and the values from the TH HEM code are assumed to equal exactly one. As shown, the slip ratios for TRACE and the TH codes deviate less than 0.1% from one. This figure was included to indicate that, along with the low void fractions calculated in Figure 4.7, the HEM model is indeed suitable for analyzing this PWR pin. If the slip ratios deviated significantly from unity, a different method (such as the drift flux or a two-fluid model, etc.) would be necessary for analyzing the system, as the HEM model would not be applicable in that case.

In summary, the TH HEM model shows very excellent agreement with TRACE in this PWR benchmark of the coolant flow. The pressures, saturation and liquid temperatures, void fractions, flow qualities, and slip ratios all were calculated to within

2% difference between the two codes. This allows for definite confidence in using the TH HEM code for analyzing coolant flow for PWR systems (and other systems which operate at high pressures, low flow rates, and low void fractions where the slip ratio between the vapor and liquid phases equal to or approach very closely to one).

4.4 NUPEC BFBT Void Distribution Benchmark

The NUPEC Full-size Fine-mesh Bundle Test (BFBT) Benchmark (Neykov et al., 2006) is a set of experimental tests which were designed, built, and performed in the late 1980s specifically for the use of validation of CFD codes for modeling BWRs. As instruments such as thermocouples show drift under very high temperatures and radiation fluences, this test is advantageous to provide more accurate temperature, pressure, and void fraction measurements under conditions that mimic BWRs without requiring the use of nuclear fuel.

A few of the notable dimensions and construction of the experimental setup are included; the remaining details (along with detailed drawings and locations of each component) are included in the NUPEC BFBT Benchmark: Volume I document (Neykov et al., 2006). The NUPEC BFBT benchmark utilizes a grid of 8 x 8 pins filled with electrical heating elements that produce a desired heat flux to simulate a BWR rod surrounded by light water. There are two types of bundles for this test: the most-current 8 x 8 setup and an 8 x 8 bundle designed to simulate high burnup. The heated rods for both types have the cladding, insulator, and heater consisting of Inconel alloy, boron nitride (BN), and nichrome, respectively. The pressure vessel is composed of titanium (Ti).

An X-ray CT scanner device, consisting of 512 detectors and an X-ray tube, coupled with detectors, was used during the NUPEC BFBT benchmark for measuring void distributions at a single axial location. For steady-state tests, a fine-mesh void distribution was measured with a spatial resolution of 0.3 mm x 0.3 mm. For the transient tests, the X-ray CT scanner was used to determine chordal-averaged void fraction measurements. Along with the X-ray CT scanner, an X-ray densitometer was used with multiple X-ray tubes and coupled with detectors which were installed at several axial locations in the experiment. At the locations where X-ray measurements were taken, the cladding of the heated rods (at the same diameter as the Inconel alloy cladding in the heated section) and channel box were composed of beryllium (Be) intended to minimize X-ray attenuation in the experiment.

The first and second volumes documenting the specifications (Neykov et al., 2006) and uncertainties (Aydogan et al., 2010) of the NUPEC BFBT Benchmark do not include all the experimental results or the associated uncertainties inherent in the experimental setup; thus, it is not possible to accurately compare the uncertainties from the experiment to the percent difference in calculated and directly measured values to gain a better perspective into the effectiveness of the AGENT-TH code at this time. The second volume (Aydogan et al., 2010) does estimate, however, that the uncertainties in the X-ray CT scanner and densitometer measurements for the void distribution benchmark range from approximately 2% to 8%. In the future, if the entire NUPEC BFBT Benchmark database is acquired, these data may be used to statistically analyze the differences from the experimental results and the AGENT-TH code.

While multiple test setups were used, including different thermal power profiles, test

assembly 0 (including assembly configurations 0-1, 0-2, and 0-3) was used in the NUPEC BFBT Benchmark to validate the AGENT-TH model. Table 4.3 includes the dimensions and properties of each of these experimental setups. The reason the type 0 assembly was used for the validation is to reduce the complexity of the system in an attempt to minimize systematic errors that may have occurred in the experimental data. This will also simplify the user input required in the AGENT-TH code, for instance, if other AGENT users desire to perform the same benchmarks in the future. The other tests may be performed using the AGENT-TH code, but the differing axial and radial power profiles in the 8 x 8 assembly require significantly more time to set up correctly.

The three different configurations used (0-1, 0-2, and 0-3) each had a different configuration of heated, unheated, and water rods, as described in Table 4.3. For this validation, the fluid within the water rods was not included in the AGENT-TH thermal hydraulics model, with the assumption that the water is well separated from the flowing coolant and thus may be considered inert. The heat transferred from the warmer flowing coolant to the unheated water rods is not calculated in this model, as the thermal energy lost from the flowing coolant is considered to be small as compared to the heat transferred to the flowing coolant. The friction losses caused by the water rods' cladding are still considered, however. Including heat loss from the flowing coolant to the water rods may be implemented in future revisions of the AGENT-TH code.

Each assembly type and configuration was submitted to a series of tests with different coolant mass flow rate and outlet temperature and pressure. Using the X-ray CT scanner and densitometer, the radial void distribution was calculated for steady-state and transient

Table 4.3. Geometries from the NUPEC full-size fine-mesh Bundle Test (BFBT) Benchmark (Neykov et al., 2006) used to validate the AGENT-TH thermal hydraulics model. The most pertinent information from test assembly 0 used to perform the validation, including a cross-sectional layout of the experiment, are included.

Test Assembly Number	0		
Assembly Configuration	0-1	0-2	0-3
Assembly Configuration Layout: = Heated Rod = Water Rod = Unheated Rod	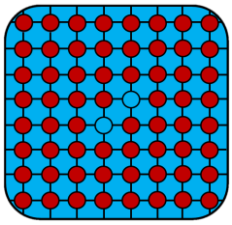	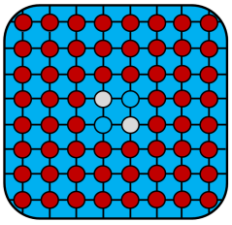	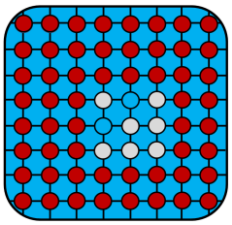
Fuel Type	Current Use 8 x 8		
Planar Power Profile	Uniform		
Axial Power Profile	Uniform		
Heated Length (m)	3.708		
Number of Heated Rods	62	60	55
Number of Unheated Rods	0	2	7
Heated Rods Outer Diameter (mm)	12.3		
Heated Rods Pitch (mm)	16.2		
Number of Water Rods	2		
Water Rods Outer Diameter (mm)	15.0		
Channel Box Inner Width (mm)	132.5		
Channel Box Corner Radius (mm)	8.0		
Spacer Type	Grid		
Spacer Axial Height (mm)	41		
Number of Spacers	7		
Spacer Pressure Loss Coefficients	1.2, 0.94*		
Locations at Bottom of Spacers from Bottom of Heated Length (m)	0.455, 0.967, 1.479, 1.991, 2.503, 3.015, 3.527		

***** Recommended pressure loss coefficient used by Galloway (2010) and Gluck (2008).

cases. In this validation, only steady-state tests are used. Of note, in the NUPEC BFBT Benchmark: Volume I (Neykov et al., 2006), there are listed two different sets of experiments including the "experimental" and "process" data. The authors of the document distinguish the "process" data as the actual values measured in time; these values are used for the validation when conflicts arise between the "experimental" and "process" data. The data used for the validation, including the NUPEC BFBT Benchmark test designations, are included in Table 4.4. For clarification, as noted underneath the table, the original information for the flow rate of the light water coolant was given in metric tons per hour (t/hr). This was converted to SI units of kilograms per second (kg/s) using the conversion in Eq. (4.2):

$$1\frac{\text{metric ton}}{\text{hour}} \cong 0.2778\frac{\text{kg}}{\text{s}} \tag{4.2}$$

The inlet subcooling column in Table 4.4 refers to the amount of internal energy above that which exists in the inlet coolant that is required to achieve saturated liquid at the prescribed pressure. The NIST water-steam thermophysical tables were used to calculate these subcooled temperatures automatically.

While the complete NUPEC BFBT Benchmark database includes radial temperature data, the available data in the Volume I specifications (Neykov et al., 2006) only include outlet coolant quality, x, for each of the tests. This was compared against the coolant outlet flow quality as calculated using the AGENT-TH thermal hydraulics model. The comparison between each test and the AGENT-TH calculation are included in Figures 4.14, 4.15, and 4.16 for assembly configurations 0-1, 0-2, and 0-3, respectively. Each

Table 4.4. Test conditions for the steady-state void distribution measurement tests from the NUPEC full-size fine-mesh Bundle Test (BFBT) Benchmark (Neykov et al., 2006) used to validate the AGENT-TH thermal hydraulics model. The test numbers used in the NUPEC BFBT Benchmark are listed for reference.

Test Assembly Number 0					
Assembly Configuration	**Test Number**	**Outlet Pressure (MPa)**	**Flow Rate (kg/s)***	**Inlet Sub-Cooling (kJ/kg)**	**Power (MW)**
0-1	0011-55	7.180	14.61	52.6	1.90
	0011-58	7.172	15.25	51.0	3.51
	0011-61	7.210	15.22	50.9	6.44
0-2	0021-16	7.190	15.24	54.0	1.91
	0021-18	7.171	15.25	59.8	3.51
	0021-21	7.179	15.25	51.4	6.45
0-3	0031-16	7.180	15.27	52.4	1.92
	0031-18	7.179	15.22	50.0	3.52
	0031-21	7.171	15.25	49.4	6.45

***** Source data was given in tons/hour and converted to SI units (1 ton/hour ≅ 0.2778 kg/s).

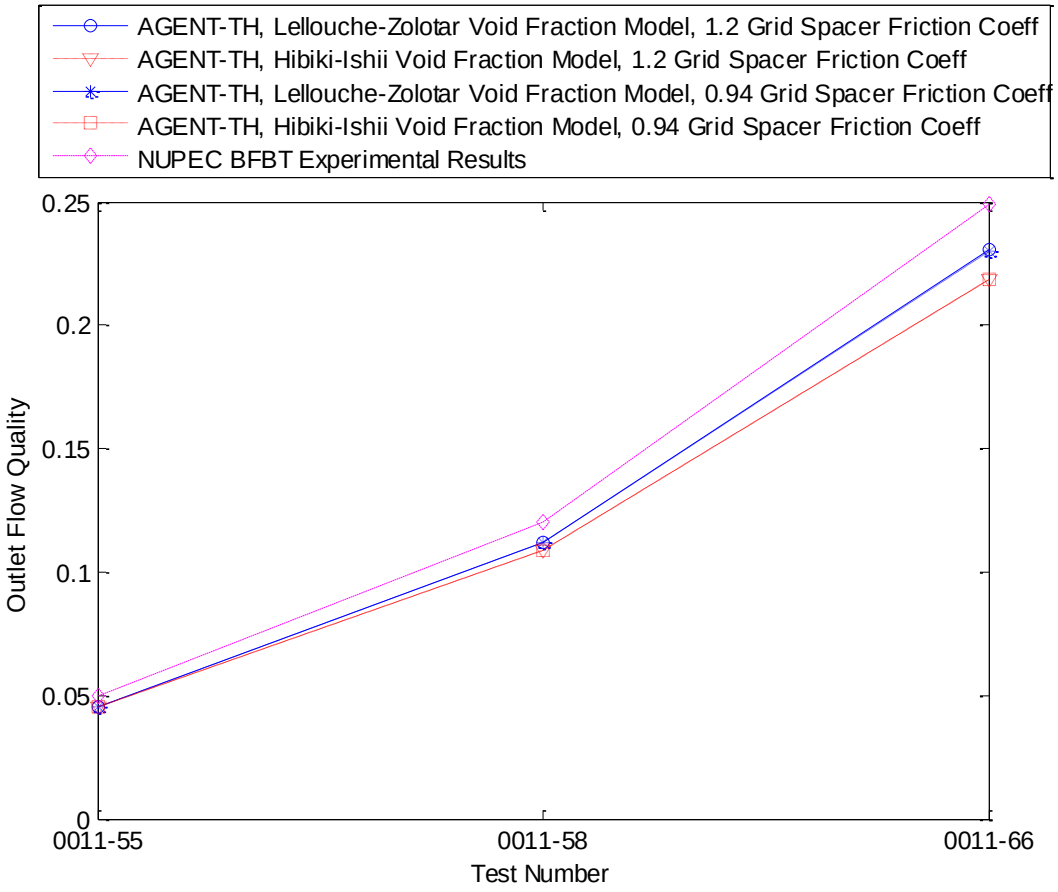

Figure 4.14. Outlet coolant quality, x, for each of the three NUPEC BFBT Benchmark tests (Neykov et al., 2006) for assembly configuration 0-1 as described in Table 4.3, as calculated using the AGENT-TH thermal hydraulics model with both the Lellouche-Zolotar and Hibiki-Ishii void fraction models. The friction coefficients for the grid spacer were also evaluated at 0.94 and 1.20 as recommended by Galloway (2010) and Gluck (2008).

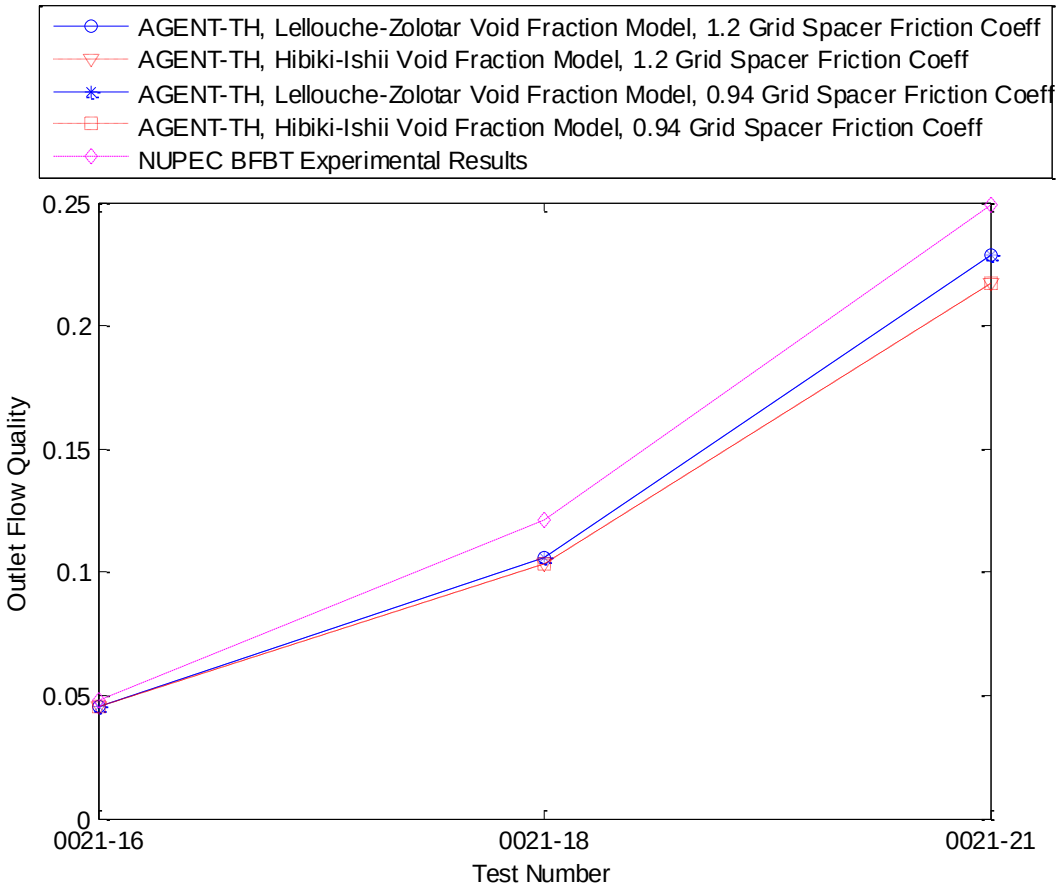

Figure 4.15. Outlet coolant quality, x, for each of the three NUPEC BFBT Benchmark tests (Neykov et al., 2006) for assembly configuration 0-2 as described in Table 4.3, as calculated using the AGENT-TH thermal hydraulics model with both the Lellouche-Zolotar and Hibiki-Ishii void fraction models. The friction coefficients for the grid spacer were also evaluated at 0.94 and 1.20 as recommended by Galloway (2010) and Gluck (2008).

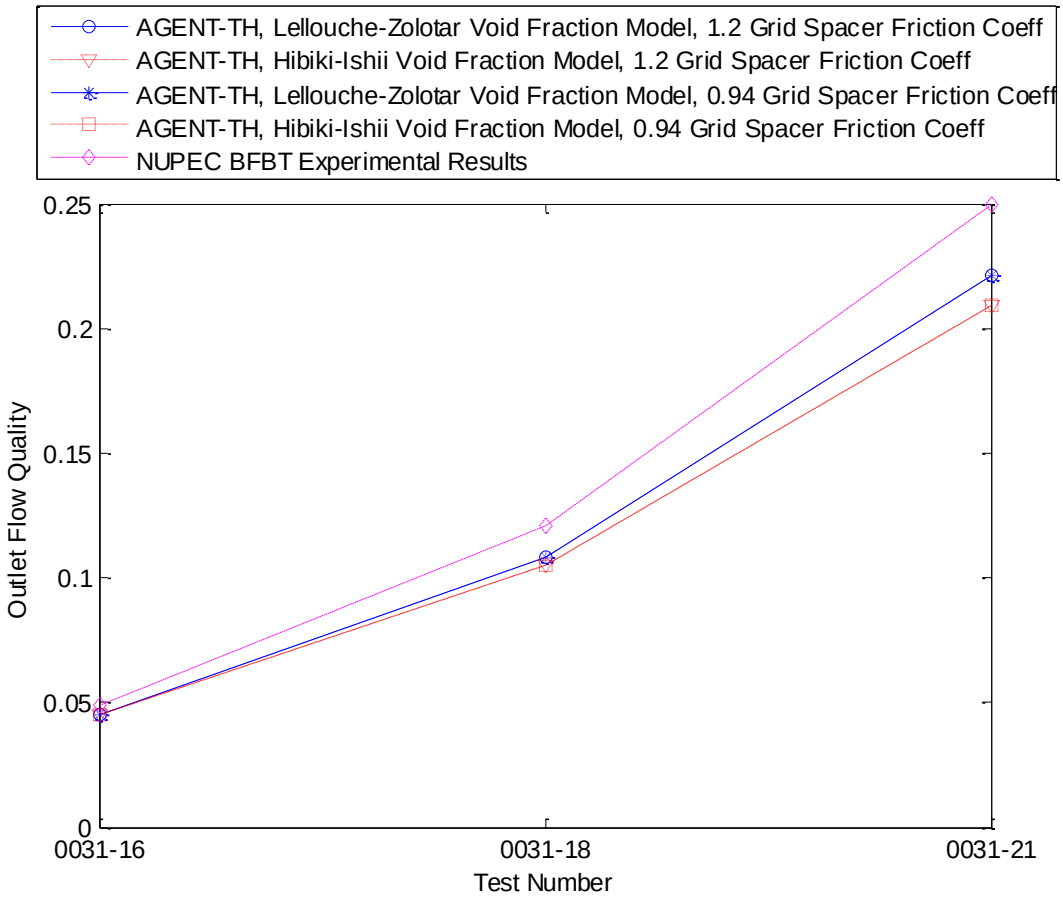

Figure 4.16. Outlet coolant quality, x, for each of the three NUPEC BFBT Benchmark tests (Neykov et al., 2006) for assembly configuration 0-1 as described in Table 4.3, as calculated using the AGENT-TH thermal hydraulics model with both the Lellouche-Zolotar and Hibiki-Ishii void fraction models. The friction coefficients for the grid spacer were also evaluated at 0.94 and 1.20 as recommended by Galloway (2010) and Gluck (2008).

plot includes results using both 1.2 and 0.94 for the grid spacer friction coefficients, as recommended by Galloway (2010) and Gluck (2008) and both the Lellouche-Zolotar and Hibiki-Ishii void fraction models.

The results show agreement between the NUPEC BFBT Benchmark measurements and the AGENT-TH calculations extremely well for the first and second tests (test results in the figures going from left to right) of each assembly configuration; each calculation and the experimental results lie within an approximate range from 4.8% to 9.2% difference for the first tests for each configuration, and from 6.6% to 14.8% for the second tests. A slightly elevated difference exists for the final tests, however, at the highest power level (the rightmost results on each of the three figures). The difference between the AGENT-TH and NUPEC results range from approximately 7.5% to 16.3%. For each test, the percent differences were calculated by dividing the absolute value of the difference between values by the experimental value and multiplying by 100. The lower differences occur while using the Lellouche-Zolotar void fraction model for each assembly configuration and test with the change in grid spacer friction coefficient from 1.2 to 0.94 creating negligible changes in the outcomes.

Aside from the void distribution benchmark described above, there were several other tests performed in the NUPEC BFBT Benchmark, including steady-state single-phase and two-phase pressure drop tests and steady-state and transient critical power benchmarks. However, the results included in the specifications (Neykov et al., 2006) are not complete. In order to perform these tests on the AGENT-TH code, it is recommended that full access to the NUPEC BFBT Benchmark database be acquired and the necessary inputs be used appropriately.

4.5 Coupled AGENT/AGENT-TH BWR Benchmark

The coupling of the AGENT neutronics code and the AGENT-TH thermal hydraulics (including the radial heat transfer model) code is of particular interest. As done with the BWR benchmark previously in this chapter, a single BWR pin was adapted from the 3 x 3 BWR study by Hoogenboom et al. (2011). Table 4.5 includes the properties of the BWR pin used in this benchmark. Table 4.6 includes the survey settings used in the AGENT neutronics code for determining the normalized axial power distribution as described in the AGENT/AGENT-TH coupling scheme in Chapter 3. The results of the criticality calculations in AGENT compared with T-NEWT in 2D and KENO VI in 3D are summarized in Table 4.7.

Table 4.5. Properties of coupled AGENT-TH analysis of single BWR pin adapted from 3x3 BWR assembly in the study by Hoogenboom et al. (2011) (Submitted on 08/20/2015 to "Progress in Nuclear Energy").

Property	**Value**
Fuel Pin Radius	0.5375 cm
Fuel Pellet Radius	0.4555 cm
Fuel Pin Pitch	1.43 cm
Fuel Material	UO_2
Fuel Density	10.25 g/cm^3
Cladding Material	Zr (pure)
Cladding Density	5.77 g/cm^3
Coolant/Moderator	H_2O
Gap Heat Transfer Coefficient ($h_{conv,gap}$)	6300 W/m^2-K
Inlet Coolant Mass Flow Rate	1.1205 kg/s
Inlet Coolant Liquid Temperature	278.78 °C
Outlet Coolant Pressure	7.06 MPa
Fuel Pin Length	3.71 m
Axial Node Number	37
Total Pin Power	61.2 kW
Initial Power Profile Along Pin Axial Height	Flat (Constant)

Table 4.6. Survey settings used in AGENT neutronics code for evaluating single BWR pin in coupled AGENT/AGENT-TH benchmark as adapted from 3 x 3 BWR array study by Hoogenboom et al. (2011) (Submitted on 08/20/2015 to "Progress in Nuclear Energy").

Property	**Settings**
Fuel Pin Unit Cell Sub-Meshing	Triangular Octant 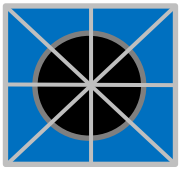
Number of Border Edges Per Side	20
Polar Angle Scheme	Leonard and McDaniel
Number of Polar Angles	2
Number of Azimuthal Angles	48 (24 - fast energy group, 24 - thermal energy group)
Ray Separation Distance (Each in Fast and Thermal Energy Groups)	0.004 cm
Assembly Boundary Condition	Reflective

Table 4.7. Eigenvalues from 2D and 3D AGENT in comparison to 2D Scale's T-NEWT and 3D KENO-VI for a single BWR pin as adapted from Hoogenboom et al. (2011) (Submitted on 08/20/2015 to "Progress in Nuclear Energy").

	Code	k_∞ **(Reflective)**
2D	AGENT Resolution parameters per Table 4.6	1.500899
	T-NEWT (Scale)	1.500817
3D	AGENT Resolution parameters per Table 4.6	1.501998
	KENO-VI (Scale) 500 generations, 50 generations skipped, 100,000 particles per generation	1.494405 ± 8.5E-5

The figures to follow describe the results of the AGENT/AGENT-TH coupled analysis which reached conversion after the third iteration. Figures 4.17, 4.18, 4.19, 4.20, and 4.21 depict the following averaged axial properties, respectively: normalized power distribution, coolant void fraction, coolant pressure, fuel temperature, and difference in fuel temperature between AGENT/AGENT-TH analysis iterations. The TRACE results included in Figure 4.18 are the same as given in the BWR benchmark previously in this chapter.

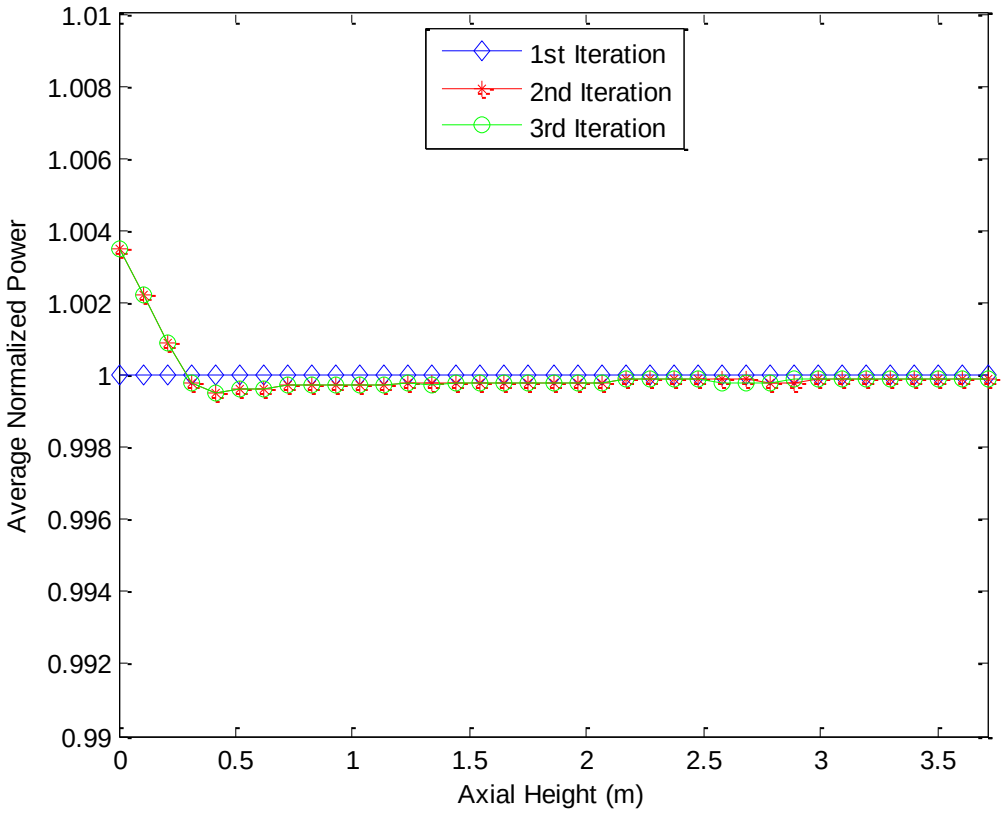

Figure 4.17. Average normalized axial power distribution of coupled AGENT-TH analysis of single BWR pin adapted from Hoogenboom et al. (2011) for iterations 1 through 3, at which point, the coupled codes converge (Submitted on 08/20/2015 to "Progress in Nuclear Energy").

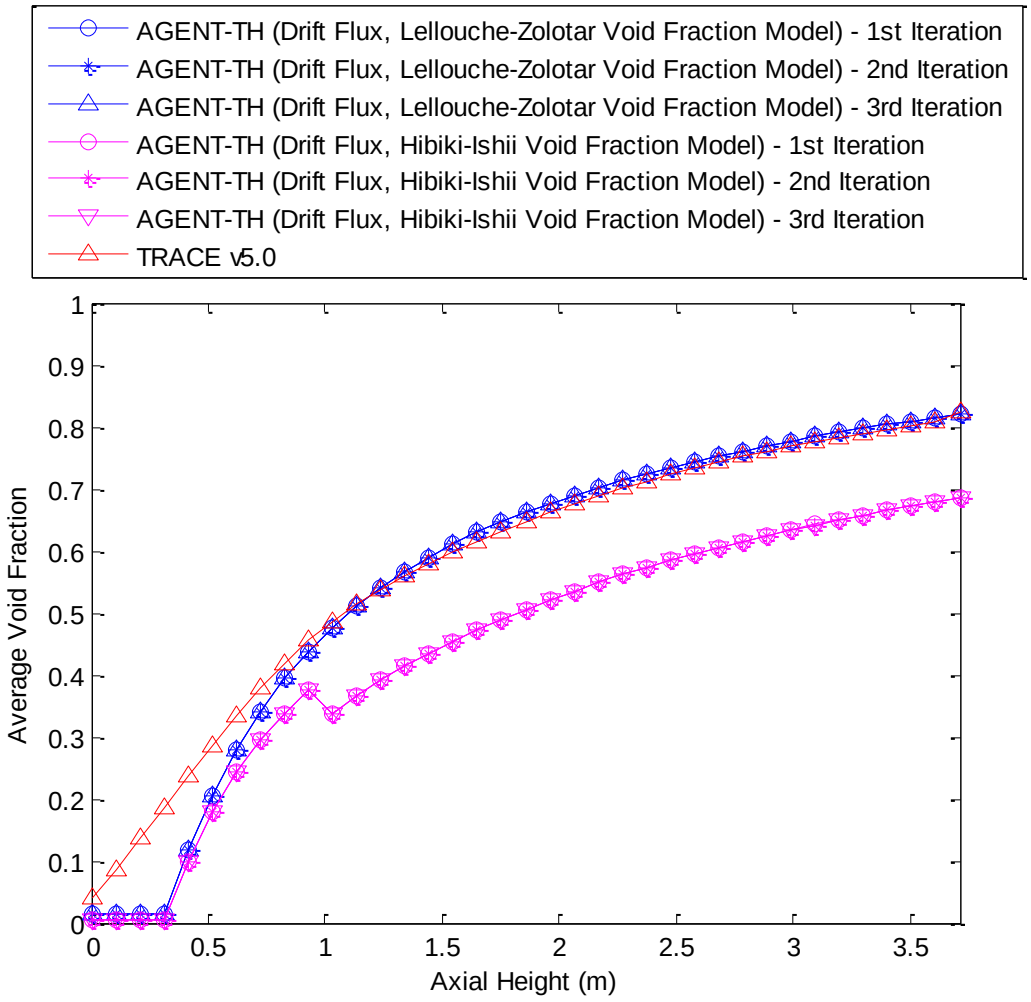

Figure 4.18. Average axial coolant void distribution of coupled AGENT-TH analysis of single BWR pin adapted from Hoogenboom et al. (2011) for iterations 1 through 3, at which point, the coupled codes converge (Submitted on 08/20/2015 to "Progress in Nuclear Energy").

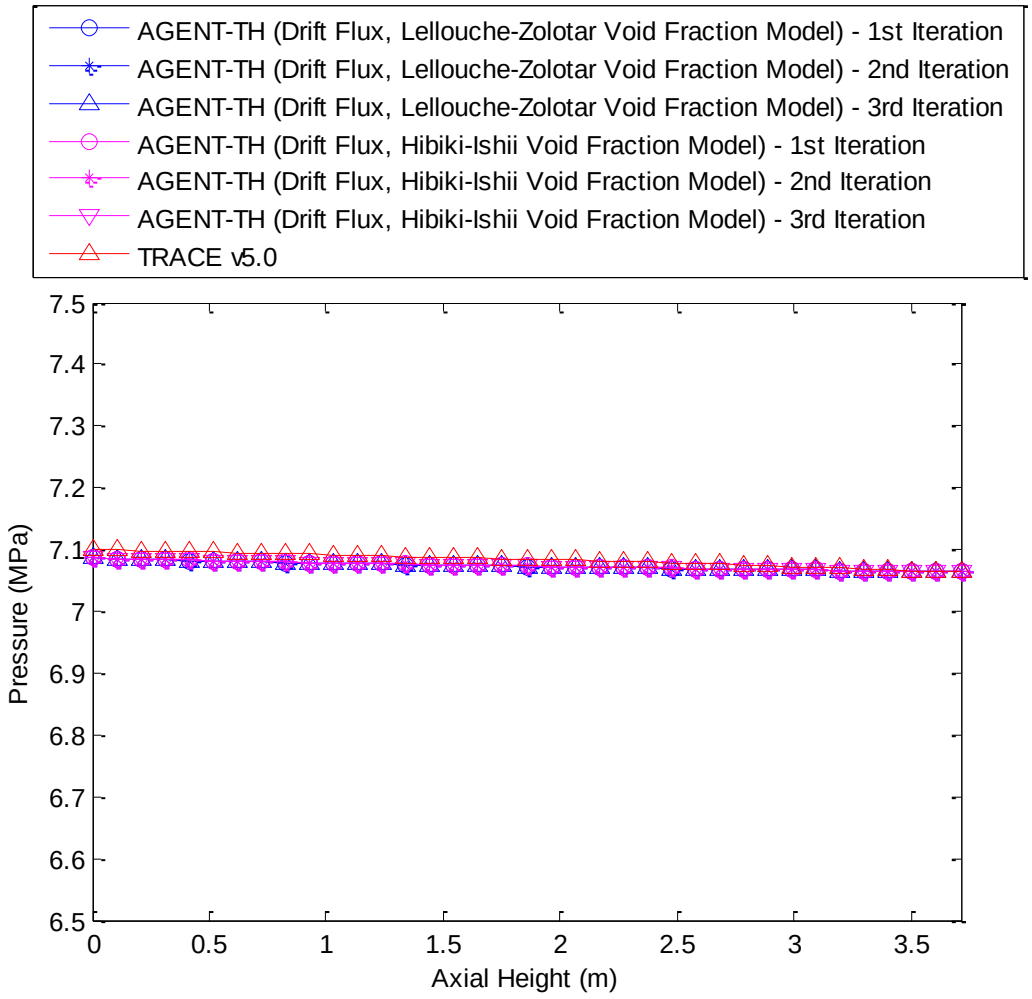

Figure 4.19. Average axial coolant pressure of coupled AGENT-TH analysis of single BWR pin adapted from Hoogenboom et al. (2011) for iterations 1 through 3, at which point, the coupled codes converge (Submitted on 08/20/2015 to "Progress in Nuclear Energy").

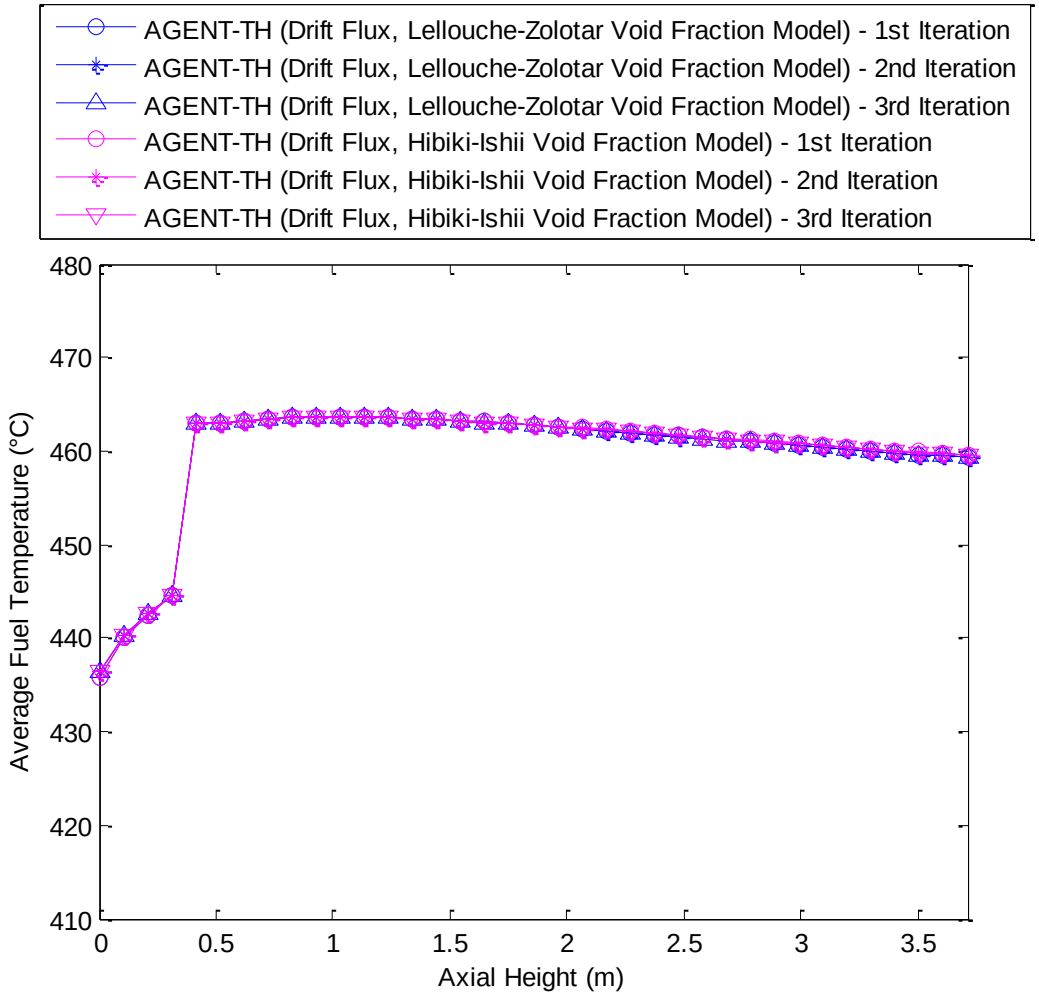

Figure 4.20. Average axial fuel temperature distribution of coupled AGENT-TH analysis of single BWR pin adapted from Hoogenboom et al. (2011) for iterations 1 through 3, at which point, the coupled codes convergence. The average fuel temperatures were averaged radially by taking a logarithmic mean of the temperatures at the fuel centerline and outer edge at each axial node (Submitted on 08/20/2015 to "Progress in Nuclear Energy").

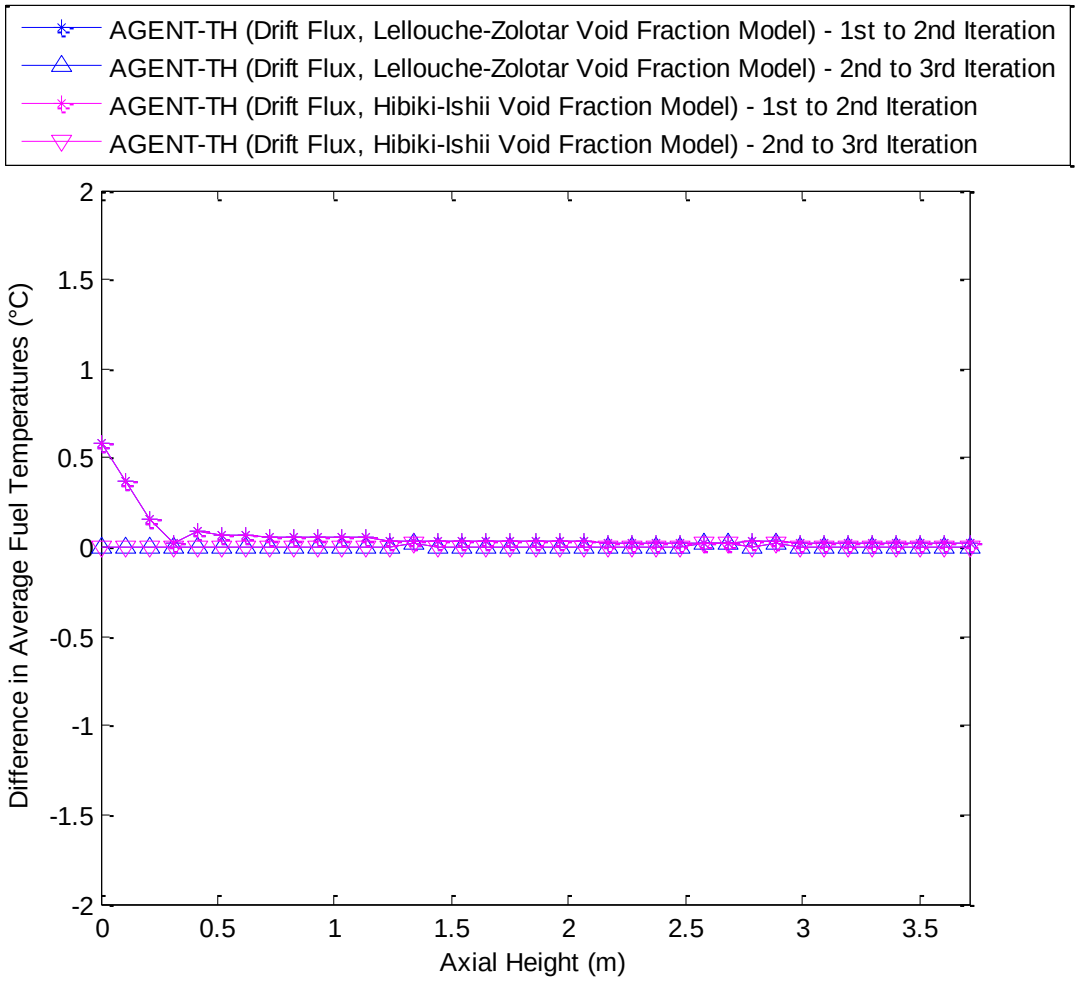

Figure 4.21. Difference in average axial fuel temperature distributions between iterations of coupled AGENT-TH analysis of single BWR pin adapted from Hoogenboom et al. (2011) for iterations 1 through 3, at which point, the coupled codes converge (Submitted on 08/20/2015 to "Progress in Nuclear Energy").

The normalized axial power distribution for the BWR coupled AGENT-TH code benchmark is indicated in Figure 4.17 for the first, second, and third iterations (at which point, the simulation reached convergence). To begin the simulation, it was assumed that the pin had a perfectly flat power profile (as the fissile uranium-235 enrichment of the pin was assumed uniform along the pin's height). The TH thermal hydraulics code (with the 1D axial coolant drift flux model and 1D radial heat transfer model as described in Chapter 3) determined the average nodal fuel temperatures along the height of the BWR pin. These temperatures were then used to recalculate neutron cross sections for the fuel using the Scale package. These updated cross sections were used in the AGENT neutronics code to recalculate the pin's normalized axial power profile for the succeeding iteration. This was done until convergence was reached at the third iteration, after which point the fuel temperatures in Figure 4.20 changed less than 3%. This was the convergence criterion decided before initiating the simulation by the user.

As is indicated in Figure 4.17, with increasing iteration, the normalized axial power profile increased near the entrance to the BWR pin. This is due to the increased neutron cross section of the fuel as temperature decreases (in cases where the fuel is designed with a negative temperature coefficient of reactivity, α_{TH}, meaning that increasing the fuel temperature will lower its reactivity, which acts as a safety precaution). As the fuel temperature increases (as is displayed in Figure 4.20), the localized reactivity and subsequent normalized axial power profile decreases. When the fuel temperature reaches a maximum at an axial height of approximately 1 m, the fuel temperature then decreases, resulting in a slight increase in the normalized power profile in Figure 4.17. Thus, as expected, the results in Figures 4.17 and 4.20 indicate that fuel temperature has a direct

effect on the power profile of the fuel pin.

The averaged axial void fractions of the BWR pin, as calculated using the coupled AGENT-TH code, are included on Figure 4.18 for the three calculation iterations for both void fraction models (Hibiki-Ishii and Lellouche-Zolotar), as introduced in Chapter 3. The TRACE values used in this figure are identical to those from the previous BWR benchmark in Figure 4.1. This is because the point kinetics neutronics model of TRACE was not used in this case; the same pin as adapted from Hoogenboom et al. (2011) was used in both cases. A flat power profile for the TRACE model was assumed in both benchmarks for comparison. The difference in void fractions between iterations differs only slightly for the two void fraction models (less than one percent); these are still included in the figure for comparison. The trends in Figure 4.18 for the void fractions, as calculated using the coupled AGENT-TH code, follow closely with those calculated in 4.1 using the TH code alone. The results indicate that the coupled AGENT-TH code had a much greater effect on the fuel temperatures in Figure 4.20 and on the normalized axial power profile in Figure 4.17 than on the coolant void fractions. As shown in Figure 4.1, when using the TH code, the AGENT-TH Lellouche-Zolotar void fraction model allows for a more accurate calculation of the BWR void fraction distribution as compared to the TRACE results than does the Hibiki-Ishii void fraction model as implemented in AGENT-TH. The Hibiki-Ishii void fraction model implementation in the TH code deserves further investigation to determine and eliminate any errors in the coding for future benchmarks.

The average axial coolant pressures for the BWR benchmark are included in Figure 4.19 and indicate excellent agreement between the coupled AGENT-TH code results with the TRACE results. The changes in pressure between the iterations of the AGENT-TH

code are miniscule and they agree with the TRACE calculated pressures to within 0.5% at any axial location.

The 1D radial heat transfer model described in Chapter 3 of the TH thermal hydraulics code was used to calculate the average nodal fuel temperatures using a logarithmic mean in Eq. (3.207) and the calculated thermal resistances of the coolant, clad, gap, and fuel. These results are included in Figure 4.20 and have been discussed as having a direct impact on the normalized axial power profile of the BWR pin in Figure 4.17. In the figure, for all three iterations of the AGENT-TH code, there is a sudden rapid rise in fuel temperature near the bottom of the BWR pin. This is because the subcooled liquid at the inlet of the BWR pin is rapidly heated by the pin during the simulation. The lower temperatures at the BWR inlet raised the local reactivity, increasing the normalized axial power at those same axial locations (as indicated in Figure 4.17). With the increase in fuel temperature in Figure 4.20, local reactivity decreases, leading to a subsequent decrease in normalized axial power in Figure 4.17. At approximately z = 1 m, the fuel temperature's previously increasing curve reaches a maximum and begins to decrease. It is expected that the maximum fuel temperature should occur closer to the center of the pin's axial height, as opposed to its edges (Duderstadt & Hamilton, 1976). This is indicated in Figure 4.20, as is expected.

To aid in determining when the simulation reached convergence (in this case, convergence was determined to be when average nodal fuel temperatures change equal to or less than 3% of the nodal fuel temperatures between iterations), the AGENT-TH code calculated and plotted the difference in axial fuel temperatures along its height, and is displayed in Figure 4.21. Between the first and second iterations, Figure 4.21 shows that a

slight change in averaged nodal fuel temperatures occurred (mostly near the bottom and top of the BWR pin). Between the second and third iterations, the difference in fuel temperatures dropped well below the convergence criterion of 3%, indicating that no further iterations are necessary. It is at this point that the simulation was deemed completed.

In summary, this benchmark was designed and performed in order to determine if the AGENT neutronics code and TH thermal hydraulics code could be successfully coupled, and if the calculated fuel temperatures in the TH code would have an effect on the normalized axial power profile calculated by AGENT. In other words, this benchmark was created to determine if the AGENT-TH coupling scheme as shown in Figure 3.10 could be achieved. As the results show in Figures 4.17 through Figure 4.21, this has been achieved. Figure 4.21 shows that the changes in temperature between iterations 2 and 3 of the AGENT-TH calculations were well below 1 Δ°C, which lies well within the convergence criterion of 3% for any of the averaged nodal fuel temperatures (which range between 582 °C and 615 °C). The Lellouche-Zolotar void fraction model again showed more accurate calculations of the axial void fraction profile as compared with the TRACE results than the Hibiki-Ishii void fraction model did. The implementation of the Hibiki-Ishii void fraction model deserves further investigation in future revisions of the TH thermal hydraulics code.

CHAPTER 5

CONCLUSION

The AGENT neutronics code, including its theoretical and mathematical bases and methodology, has been explained in detail. The capabilities of the AGENT code for analyzing nuclear reactors have been summarized along with its limitations in modeling nuclear reactor coolant flow.

To supplement the neutronics capabilities of AGENT, the drift flux and homogeneous equilibrium mixture (HEM) fluid dynamics models have been implemented in a 1D subchannel finite difference scheme in the TH thermal hydraulics code, which has been shown to be capable of coupling with the AGENT code. The TH code includes the EPRI Net Vapor Generation (NVG) model to take into account subcooled vapor generated within the coolant. Implemented with the TH drift flux model is included both the Lellouche-Zolotar and Hibiki-Ishii void fraction models for calculating void fraction within the coolant subchannels. Benchmarks using the TH code of single PWR and BWR fuel pins surrounded with light water coolant demonstrate the code's effectiveness as compared with analysis results from TRACE, a software package designed for the analysis of light water reactors.

The AGENT neutronics code has been coupled with the TH thermal hydraulics code using a nodal 1D radial heat transfer model for each fuel pin to determine average nodal

fuel temperatures. These temperatures allow for the temperature-dependent neutron cross sections for the fuel at each axial node to be calculated using the Scale package. The drift flux and HEM benchmarks against results from TRACE show excellent agreement, especially when employing the Lellouche-Zolotar void fraction model as implemented in the TH code. The benchmarks using the drift flux code compared to experimental results from the NUPEC BFBT test are all within 5% to 17% difference of the provided measurements.

The benchmark of the BWR pin using the coupled AGENT-TH code demonstrated that the analysis converted within three iterations while including the effects of temperature-dependent neutron cross sections taken from Scale. The axial power profile of the BWR pin was shown to increase due to lowered fuel temperature at the bottom of the BWR, as was predicted.

The recommended future improvements to the TH thermal hydraulics code and the coupled AGENT-TH code are described further in Chapter 6 to follow.

CHAPTER 6

FUTURE WORK

While the TH thermal hydraulics code shows excellent agreement with simulations from TRACE, a range of higher percent differences exists in the results of the NUPEC BFBT benchmarks from Chapter 4 (from approximately 5% up to 17% difference). To determine the cause of these differences it is recommended that the full NUPEC BFBT database be obtained to allow for more benchmarks to be performed and to analyze sources of inaccuracies from the NUPEC BFBT that may propagate in the thermal hydraulics analysis.

Further refinement and testing of the TH code, particularly concerning the 1D radial heat transfer model, will allow more accurate results as compared to other benchmarks when using the AGENT-TH coupling scheme. Although it has proven to be difficult in the past (Todreas & Kazimi, 1990), it may be possible to implement a radial 2D fluid dynamics scheme at each axial node to work in conjunction with the 1D subchannel code as currently implemented in the TH code, which may increase accuracy. An implementation of a 2D axial conduction heat transfer model for the fuel may also provide for a more accurate axial temperature distribution of the fuel.

It is also recommended that further investigation be done into the implementation of the Hibiki-Ishii void fraction model into the TH code. The results are not as accurate as

those derived while using the Lellouche-Zolotar void fraction model on every benchmark performed. This may require updating the flow regime plot as used in Figure 3.5 in Chapter 3 to determine if the flow is slug, bubbly, churn, or annular flow, as each regime has a separate set of equations in the Hibiki-Ishii void fraction model.

Finally, it would be highly advantageous to consolidate the AGENT/AGENT-TH coupling scheme into a set of codes which perform calculations automatically given the user inputs. This would reduce time required for computation and for the user to run each separate code in the coupling scheme. At present, the Scale, AGENT, and AGENT-TH codes must be set up and run separately with the pertinent results from each manually input into the next code in the coupling scheme. This would require the development of a code to calculate the temperature-dependent neutron cross sections without requiring running the simulation in Scale.

REFERENCES

1. Abbot, M.B., 1966. An introduction to the method of characteristics. Elsevier, New York, USA.

2. Asmar, N.H., 2005. Partial Differential Equations with Fourier Series and Boundary Value Problems, Second Edition. Pearson Education, Inc.

3. Aydogan, F., Hochreiter, L., Ivanov, K., Martin, M., Utsuno, H., Sartori, E., 2010. NUPEC BWR Full-Size Fine-Mesh Bundle Test (BFBT) Benchmark, Volume II: Uncertainty and Sensitivity Analyses of Void Distribution and Critical Power – Specification. OECD, NEA No. 6343, NEA/NSC/DOC(2007)21, ISBN 978-92-64-99124-8.

4. Bergman, T.L., Lavine, A.S., Incropera, F.P., DeWitt, D.P., 2011. Fundamentals of Heat and Mass Transfer, Seventh Edition. John Wiley & Sons, Inc.

5. Boroushaki, M., 2009. Numerical solution of the neutron transport equation using cellular neural networks. Annals of Nuclear Energy, 36(1), 15-27.

6. Chexal, B., Lellouche, G., 1986. A Full Range Drift-Flux Correlation for Vertical Flows. EPRI NP-3989-Sr.

7. Duderstadt, J.J., Hamilton, L.J., 1976. Nuclear Reactor Analysis. John Wiley & Sons, Inc. New York, USA.

8. Eklund, M., Alamaniotis, M., Hernandez, H., Jevremovic, T., 2015. Method of characteristics – A review with applications to science and nuclear engineering computation. Progress in Nuclear Energy, 85, 548-567, ISSN 0149-1970, http://dx.doi.org/10.1016/j.pnucene.2015.05.002.

9. Galloway, J.D., 2010. Boiling Water Reactor Core Simulation with Generalized Isotopic Inventory Tracking for Actinide Management. PhD Dissertation. University of Tennessee, Knoxville.

10. Gluck, M., 2008. Validation of the subchannel code F-COBRA-TF Part I. Recalculation of single-phase and two-phase pressure loss measurements. Nuclear Engineering and Design. 238, 2308.

11. Haberman, R., 1983. Elementary applied partial differential equations. Englewood Cliffs, NJ, USA, Prentice Hall.

12. Hewitt, G.F., Roberts, D.N., 1969. Studies of Two-Phase Flow Patterns by Simultaneous X-Ray and Flash Photography. AERE-M2159.

13. Hibiki, T., Ishii, M., 2003. One-dimensional drift-flux model and constitutive equations for relative motion between phases in various two-phase flow regimes. International Journal of Heat and Mass Transfer 46, 4935-4948.

14. Hibiki, T., Ishii, M., 2005. Erratum to: "One-dimensional drift-flux model and constitutive equations for relative motion between phases in various two-phase flow regimes". International Journal of Heat and Mass Transfer 48, 1222-1223.

15. Hong, S.G., Cho, N.Z., 1998. CRX: a code for rectangular and hexagonal lattices based on the method of characteristics. Annals of Nuclear Energy 25(8), 547-565.

16. Hoogenboom, J.E., Ivanov, A., Sanchez, V., Diop, C., 2011. A Flexible Coupling Scheme for Monte Carlo and Thermal-Hydraulics Codes. International Conference on Mathematics and Computational Methods Applied to Nuclear Science and Engineering (M&C 2011), Rio de Janeiro, RJ, Brazil.

17. Hursin, M., Jevremovic, T., 2005. Agent code: Neutron transport benchmark example and extension to 3D lattice geometry. Nuclear Technology and Radiation Protection 20(2), 10-16.

18. Hursin, M., Xiao, S., Jevremovic, T., 2006. Synergism of the method of characteristics, *R*-functions and diffusion solution for accurate representation of 3D neutron interactions in research reactors using the AGENT code system. Ann. Nucl. Energy 33, 1116-1133.

19. Ishii, M., Hibiki, T., 2006. Thermo-Fluid Dynamics of Two-Phase Flow. Springer Science+Business Media, Inc.

20. Jevremovic, T., Vujic, J., Tsuda, K., 2001. ANEMONA – a neutron transport code for general geometry reactor assemblies based on the method of characteristics and R-function solid modeler. Annals of Nuclear Energy 28(2), 125-152.

21. Jevremovic, T., Ito, T., Inaba, Y., 2002. ANEMONA: multiassembly neutron transport modeling. Annals of Nuclear Energy 29(17), 2105-2125.

22. Jevremovic, T., Xiao, S., Satvat, N., Gert, G., 2006. Performance, accuracy and efficiency evaluation of a three-dimensional whole core neutron transport code AGENT. Proc. Int. Conf. ICONE14, Miami, FL, USA. 435-445.

23. Jevremovic, T., Xiao, S., Satvat, N., Gert, G., Hopkins, J., 2008. Neutron transport benchmark examples with web-based AGENT. Nuclear Engineering and Design 238(8), 1975-1986.

24. Jevremovic, T., 2009. Nuclear Principles in Engineering, Second Edtion. Springer Science+Business Media, LLC.

25. Joe, H.C., Barber, D., Jiang, G., Downar, T.J., 1998. PARCS, A Multi-Dimensional Two-Group Reactor Kinetics Code Based on the Nonlinear Analytic Nodal Method. PU/NE-98-26.

26. Lahey, R., Moody, F., 1977. The Thermal Hydraulics of a Boiling Water Nuclear Reactor. American Nuclear Society. La Grange Park, Il.

27. Lathrop, K.D., 1969. Spatial differencing of the transport equation: positivity vs. accuracy. Journal of Computational Physics 4(4), 475-498.

28. Lellouche, G., Zolotar, B., 1982. Mechanistic Model for Predicting Two-Phase Void Fraction in Vertical Tubes, Channels, and Rod Bundles. EPRI NP-2246-SR.

29. National Institute of Standards and Technology, 2011. Thermophysical Properties of Fluid Systems: <http://webbook.nist.gov/chemistry/fluid/>.

30. Neykov, B., Aydogan, F., Hochreiter, L., Ivanov, K., Utsuno, H., Fumio, K., Sartori, E., 2006. NUPEC BWR Full-Size Fine-Mesh Bundle Test (BFBT) Benchmark, Volume I: Specifications. OECD, NEA No. 6212, NEA/NSC/DOC(2005)5, ISBN 92-64-01088-2.

31. Reddy, D., Sreepada, S., Nahavandi, A., 1982. Two-Phase Friction Multiplier Correction for High-Pressure Steam-Water Flow. EPRI NP-2522. Electric Power Research Institute.

32. Ronchi, C., Sheindlin, M., Musella, M., Hyland, G.J., 1999. Thermal conductivity of uranium dioxide up to 2900 K from simultaneous measurement of the heat capacity and thermal diffusivity. Journal of Applied Physics 85, 776, doi: 10.1063/1.369159.

33. Saha, P., Zuber, N., 1975. Point of Net Vapor Generation and Vapor Void Fraction in Subcooled Boiling. Proc. 5th International Heat Transfer Conference B4.7.

34. Tai, C.H., Zhao, Y., Liew, K.M., 2005. Parallel-multigrid computation of unsteady incompressible viscous flows using a matrix-free implicit method and high-resolution characteristics-based scheme. Computer methods in applied mechanics and engineering, 194(36), 3949-3983.

35. Todreas, N.E., Kazimi, M.S., 1990. Nuclear Systems I Thermal Hydraulic Fundamentals. Taylor & Francis.

36. USNRC, Division of Safety Analysis, Office of Nuclear Regulatory Research, 2012. TRACE V5.0 THEORY MANUAL: Field Equations, Solution Methods, and Physical Models.

37. Xiao, S., 2009. Hardware Accelerated High Performance Neutron Transport Computation Based On AGENT Methodology. PhD Dissertation, Purdue University, West Lafayette, IN, USA.

38. Zuber, N., Findlay, J., 1965. Average Volumetric Concentration in Two-Phase Flow Systems. J. Heat Transfer 87, 453.